Computational and Experimental Studies of Graphene and Carbon Nanotubes

By

Moshibudi Shai

A dissertation submitted in partial fulfillment of
the requirements for the degree of

Master of Science

In

Physics

In the

Faculty of Science and Agriculture

(School of Physical and Mineral Sciences)

At the

University of Limpopo

Supervisor: Dr T.E Mosuang

Co-Supervisor: Prof. K.E Rammutla

2016

DECLARATION

I declare that the dissertation hereby submitted to the University of Limpopo for the degree of Master of Science has not been previously submitted by me for a degree at this or any other university; that it is my work in design and execution, and that all material contained therein has been duly acknowledged.

Moshibudi Shai

Signature_____ **Date** _____

ACKNOWLEDGMENTS

I wish to express my sincere gratitude to my supervisors, Dr T.E. Mosuang and Prof K. E. Rammutla, for their excellent guidance and support during this research. I would like to thank my numerous friends at the University of Limpopo especially my fellow students and Prof Mônica A. Cotta from IFGW-UNICAMP University in Brazil for hosting me in her laboratory. I would also like to acknowledge the en.wikipedia.org and www.qrc.nasa.gov pictures/photographs as referenced in chapter 6. Acknowledgements are also in order for finance assistance received from National Research Foundation (NRF) and India Brazil South Africa trilateral cooperation (IBSA). I thank my family for always being there for me. I dedicate this dissertation to my grandmother and my husband.

Abstract

Bilayer graphene and single-walled carbon nanotubes were studied through classical molecular dynamics using Tersoff potential. The Tersoff potential has been the most successful model to replicate much of the semiconducting properties in carbon structures. The simulations were performed within a canonical (NVT) ensemble for structural properties and isothermal–isobaric ensemble (NPT) for thermodynamic properties of both materials. The bilayer graphene consists of two models of 64 and 256 atoms. Single-walled carbon nanotubes consist of three chiral structures of 264 atoms which is cnt(12,10), 260 atoms which is cnt(10,12) and armchair structure of 312 atoms which is cnt(12,12). The structural and thermodynamics properties were investigated in a range of temperature from 300 - 5000 K. It has been found that some of the properties of the graphene and carbon nanotube are similar. Graphene256 was found to be more stable than graphene64 and the armchair cnt(12,12) appears to be more mechanically stable than chiral cnt(12,10). Graphene and single-walled carbon nanotubes were also studied using X-ray diffraction and atomic force microscopy (AFM). The lattice constant for both materials were calculated and they agree well with the computational results. For carbon nanotubes, different solvents were used for characterization using the AFM. Chloroform was the best solvent since we managed to find some bundles of carbon nanotube. For ethanol and toluene solvents we did not managed to get any bundles. The diameter of single-walled carbon nanotube was determined only on a solution that chloroform solvent was used.

List of Figures

List of Tables

Table of Contents

Chapter 1

Introduction

1. 1 Background on Carbon Material

Elemental carbon atom is readily found in various formations. The food for human consumption, clothes being worn, cosmetics, and fuels being used as source of energy, have carbon as the main constituent atom [1]. From fundamental chemistry it is known that carbon is the sixth element in the periodic table. Generally, all the life in the solar system (plants and animals) is based on the elemental carbon atom [1]. For human usage, carbon mineral is extracted through mining coal. The atomic structure of carbon provides it with a high strength to weight ratio. This property is experienced in various carbon containing compounds when exposed to different adverse conditions. The word carbon is derived from the Latin word carbo, meaning charcoal [2].

Stone Age history tells of carbon in the form of charcoal was already made by burning organic material like plants (trees) in an enclosed cask. This material element is readily obtained in the solar system. Carbon can be found in the sun, in the moon, in the neighbouring planets and the stars of the galaxy [1, 2]. Meteorites which fall from outer space were found to have some traces of carbon. Evolution with carbon research has unearthed many outstanding properties. Some forms of carbon structures can have different properties of mechanical, electrical, optical, and sensing. The above mentioned properties can be informed by either sp^3-hybridized carbon atoms, sp^2-hybridized carbon atoms, or both [3]. At high temperatures and pressures, one form of carbon can be transformed into the other form. But the actual structural evolution and energy differences among the different forms is not well understood. Carbon can bond with other carbon atoms and it can even bond with other different atoms making rings and chains. In case of the bulk material, carbon can either be in the form of diamond or graphite, but at the nano-scale material, it can be in the form of graphene, nanotube, bucky balls or fullerenes [2].

1.2. Diamond and Graphite

Diamond is a form of carbon, where carbon atoms are packed in a tetrahedral plane of carbon triangles making a face-centred cubic (fcc) crystal structure which has sp^3 orbitals. Many studies show that, diamond is less stable than graphite at normal temperatures and pressures [3], but the changing or transforming from diamond to graphite is negligible at standard conditions. Diamond is known to have the highest hardness and thermal conductivity of any bulk material ever tested [3, 4]. Each carbon atom in a diamond structure is bonded to four other atoms throughout the crystal lattice. This is through the four valence electrons in carbon which in turn bond covalently among themselves. There are no free electrons in diamond because all atoms are involved in bonding. This property makes diamond a poor conductor of electricity [4]. Another polymorph of carbon is graphite which is composed of sp^2-hybridised orbitals [5]. Each carbon atom in graphite is bonded to three other carbon atoms in plane, which make a hexagonal honey comb of carbon atom sheet. Several studies have found graphite to be stable at standard temperature and pressure. This resulted to it being used in thermochemistry as the standard state for defining the heats of formation [5]. Graphite is also used as a substrate in various bombardment and irradiation experiments. The bond length of graphite is 1.42 Å, and the distance between planes is 3.35 Å [5, 6].

1.3. Graphene

Currently, a vast of physics research is focused on nano-scale materials. At the nano-scale carbon structures, there is a great interest in graphene and carbon nanotubes. Freshly there is also a talk about nano- diamond. Graphene was discovered in 2004 and has since stimulated much interest in the field of condensed matter physics. It is a thin sheet of carbon atoms arranged in a two dimensional honeycomb crystal [7]. The presence of graphene has been discussed by the objective that, graphene has an intrinsic roughness. That is what makes graphene to be the good perfect two dimensional crystal in three dimensional spaces which is not forbidden [8]. Graphene is not only an essential new testing ground for fundamental physics such as relativistic quantum mechanics and low dimensional thermodynamics, but also has an important applications to nano-scale technology [9]. The covalent bonds between nearest-neighbour carbon atoms in graphene are formed by sp^2-hybridised orbitals making

strong bonds. The single non-bonded electrons in each carbon reinforce themselves in pi (π) bond formation. Because of its robust bonds among carbon atoms, graphene has remarkable mechanical strength. The result is that graphene has unique free-standing sheets, being only one atomic layer thick [10]. The remaining p-orbital electron per atom is delocalized over the whole graphene lattice, and is responsible for the electrical conductivity. The carbon-carbon bond length of graphene is 1.42 Å similar to that of graphite. Graphene has exclusive structural, mechanical and electronic properties. For this reason, it has inspired many scientists involved in the field to look forward to making a breakthrough in some new research areas. At present, research has discovered many potential applications of graphene in solar cell technology [11], sensors, liquid device and the fabrications of nano-sized prototype transistors [12].

Applications of graphene are parallel to those of carbon nanotubes. Like carbon nanotubes, graphene is also suitable for usage as a gas sensor material to detect different molecules, ranging from gas phase to some small bioactive molecules [13]. These remarkable properties obligate graphene to offer incredible short-circuit current-gain cutoff frequency for high frequency applications. It has recently been established by Wang *et al*. [13] that high speed graphene devices were carried out with a cutoff frequency reaching up to 100 GHz, demonstrating the significant importance of graphene devices for radio frequency (RF) applications. Due to highly conductive π electrons, graphene has a zero energy band gap, so is not appropriate for the fabrication of digital field-effect transistor (FET) devices. If one need to create such a device from graphene, a band gap need to be introduced in the graphene sheet structure. Another possible solution to this is to restrict the free π electrons motion within a sheet to specific energies until discrete levels are apparent in graphene ribbons. The other solution is the introduction of a double layer graphene structure with a tuneable interplanar spacing. Graphene also has a huge potential to be a key ingredient of new devices, such as single molecule gas sensors, ballistic transistors and spintronic devices. Bilayer graphene consists of two packed monolayer sheets and where the quasi-particles are massive chiral fermions, have a quadratic low-energy band which involve various scattering properties from those of the monolayer graphene. It also presents the particular properties that can be used to open a tuneable band gap. These particular properties have made bilayer graphene a subject

of a great interest [14]. Graphene nano-devices functionality depends strongly on the structure of the edges. Because graphene nano-devices have an important chemical character, in future large scale processing of graphene device technology can be possibly imply the use of ion beam and plasma based etching techniques [15]. Graphene has been correlated with some various superlatives strongest and thinnest material; it is the first example of an atomically thick membrane. Such unique properties make it to be a great applicant for industrial applications. The on-going studies try to address certain problems like cost effective production before this can be invested in practice. Apart from its important usefulness, graphene is proven to be scientifically compelling in its own right. Graphene is not like any materials, electrons in graphene have a linear dispersion relation close to the Fermi energy and its behaviour is almost relativistic [16]. Graphene have electronic properties that are particularly different to other carbon polymorphs. For an example; graphene's low-energy quasi-particles behave as massless chiral Dirac fermions which have led to the experimental observation of many great effects similar to those predicted in the relativistic regime [16].

1.4. Carbon Nanotubes

Carbon nanotubes are new class of materials with assumed one dimensional (1D) structure. The structure occupied the minds and illusions of vast scientific communities for their distinctive electrical, mechanical, and thermal properties [17]. Apart from pronounced intuitive thinking provoked by this kind of materials, the physics get simplified from three dimensional to the fundamental one-dimensional, scrutinizing nano-size and molecular electronics, as well as expanding the connection between structure and properties. Single-walled carbon nanotubes (SWCNT) have many interesting applications which currently make it to be the subject of great experimental and theoretical studies [17]. Investigations with nanotubes are quite diverse; chemists and materials scientists explore different synthesis techniques whilst physicists explore novel characteristics. SWCNT is a tube made of a single graphite or graphene layer rolled up into a sanctify cylinder and multi-walled carbon nanotube (MWCNT) is a tube containing several, intensively arranged cylinders [18]. Both SWCNT and MWCNT have a wall-to-wall distance of the same range as the interlayer spacing in graphite (≈3.41 Å). The bond length of the two tubes is similar, but MWCNT have much larger diameters than SWCNT [18]. SWCNT and MWCNT have the inner and outer

diameters around 50 and 1000 Å, respectively, related to about 30 coaxial tubes. Constraining consequences in MWCNT are expected to be less dominant than in single-walled tubes, because MWCNT have a larger circumference. In numerous ways, multi-walled carbon nanotubes behave the same as graphite flakes [20]. The microscopic structure of carbon nanotubes are derived from that of graphene, which is the main reason carbon nanotubes are being labelled using the same procedure used for graphene lattice vectors [21]. Carbon nanotubes precarious smooth graphitic cylinders show an unexpected merger of a nanometre-size diameter and millimetre-size length. The ability of nanotubes to twist, bend, and stretch in a defect free mode on a macroscopic scale, gives rise to unusual electronic properties of individual single-walled nanotubes. Depending on the nanotubes diameter and the angle of folding the tubes can either be conducting or insulating. Surrounding environment and point defects may alter the conducting properties of these nanotubes [22].

A typical carbon nanotube is created from a rectangular segment cut from a graphene sheet then rolled into a seamless tube. Carbon nanotube chirality represents the angle at which the graphene is folded back on itself. The symmetrical form of the force fields of the carbon nanotube is determined by the chirality, which again determines the cooperation of the CNTs within the bundle. Chiral symmetry has three distinct forms, which are armchair, zigzag, and chiral. From these distinct forms of chirality, a variety of diameter sizes could be formed. According to Majure *et al*. [23] as shown in figure 1.1, the vector L is equal to the length of the carbon nanotube and parallel to the axis of the carbon nanotube. Chiral vector *C (n,m)* can determine the width of the segment, which can be used to determine also the chirality of the carbon nanotube where n and m are integers[23]. Any other chirality with a chiral angle between those of armchairs *(n; n)* and zigzags *(n; 0)* is called a chiral nanotube. These nanotubes have a staircase like track of carbon hexagons along the length of the tube. The angle of the chiral vector can be used to determine the angle of the staircase in a carbon nanotube. A carbon nanotube is completely described by its length and chirality. Mathematically, a chiral vector is a linear combination of the unit vectors that define the hexagonal lattice, a_1 and a_2, as

$$Ch = ma_1 + na_2, \qquad (1.1)$$

where n and m are the integers, $n \geq m$.

The circumference of the carbon nanotube is called the normal of the chiral vector. The diameter of a carbon nanotube can thus be written in terms of the carbon-carbon bond length l and the chiral vector indices n and m as follows:

$$D_{CNT}=\frac{a}{\pi} l\sqrt{n^2+mn+m^2}\ . \qquad (1.2)$$

The symmetry of carbon nanotube was described by so called line groups, which were introduced by Damnjanović *et al*. [24-27].

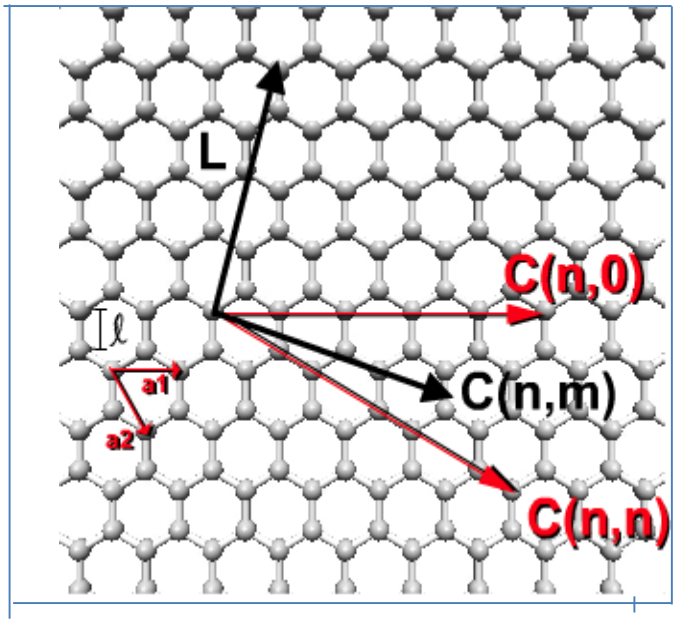

Figure 1. 1: An explanation of the chiral vectors in a graphene sheet [23].

D. L. Majure, R. W. Haskins, N. J. Lee, C. R.Welch and C. F. Cornwell, Journal of chemical physics 127, (074708) 2007*

1.5 Dissertation Layout

Chapter 1 entails the overall introduction about carbon based compounds. Bulk graphite and diamond phase are explored and then toned down to nanoscale two dimensional graphene and one dimensional carbon nanotubes.

Chapter 2; a more detailed discussion of graphene and carbon nanotubes applications is brought forward. Here structural, semiconductor, gas sensing and energy properties of graphene and carbon nanotubes are being presented.

Chapter 3 reports the theory of the computational method used in this dissertation. Classical molecular dynamics together with empirical potentials suitable for this study are introduced.

Chapter 4 and **5** presents structural, equilibrium, and thermodynamic properties results in graphene and carbon nanotubes. Similarities and deviation are being noted.

Chapter 6 discusses the XRD and AFM results of graphene and carbon nanotubes. Further comparison with computational results and literature is made.

Chapter 2

Literature Review

2.1 Structural Properties of Graphene and Carbon Nanotubes

Graphene, which can be described as a single layer of carbon atoms arranged in a hexagonal benzene ring like crystal structure was studied by transmission electron microscopy on sheets of graphene suspended between bars of a metallic grid [5, 7, 9]. Hexagonal lattice arrangement of graphene was shown by the electron diffraction patterns. Suspended graphene also showed "rippling" of the flat sheet, with amplitude of about 10.0 angstroms (Å) [7]. When rolling a graphene honeycomb sheet into a cylindrical shape, that can be called a carbon nanotube. The structural edge shape of graphene sheet brought about classifying different types of nanotubes using a chiral vector (*n*, *m*), where *n* and *m* are integers [28]. The values of *n* and *m* explain the chirality of potential nanotubes. This affects the nanotube lattice structure, density, thermal and conduction properties. Noel *et al*. [17] and Nomura and MacDonald [29] studies are based on first-principle spin-polarized calculations to study the structural and electronic properties of a hybrid of an armchair graphene nanotube and a zigzag graphene nano-ribbon [17, 29]. These properties mostly depend either on the nanotube position or on the spin orientation. In most cases the electronic structure of the carbon nanotube is affected by the interlayer spacing in multi-walled nanotubes, the width and length of nano-ribbons and the stacking configuration in the case of double layered ribbons [19, 21]. Both zigzag and armchair carbon nanotube and graphene have the lattice parameter of 2.46 Å [18]. In figures 2.1 and 2.2, an illustration of a single layer of graphene honeycomb and single-walled carbon nanotubes are shown.

Bahk *et al*. [30] investigated the cylindrical length of carbon nanotubes (CNTs) by electrical mobility classification and developed a filtration based method. Measurements were carried out in an atmospheric environment then related with liquid produced CNTs. For arbitrary alignment where carbon nanotubes are considered to be obtained readily, the tubular geometrical length of a CNT can be written as [31],

$$L_{CNT} = \frac{A\lambda d_m}{d_{CNT} C_c}, \qquad (2.1)$$

where λ is the mean free path of gas, d_m is the electrical mobility size, d_{CNT} is the CNT diameter, A is the uncertainty, C_c is the Cunningham slip correction, and the uncertainty:

$$A = 2\left(\frac{1}{f} + \frac{2}{\left(\left(\frac{\pi-2}{4}\right)+2\right)}\right) \quad (2.2)$$

where f is the momentum accommodation coefficient $(= 0.9)$. For the total alignment, then the length of carbon nanotube is given by

$$L_{CNT} = \frac{6\lambda d_m}{f d_{CNT} C_c} \quad (2.3)$$

The length of SWCNTs was determined using the reproducible method by Nicholas *et al* [32]. The method is established on determining the viscosity of a macroscopic sample of dilute suspended SWCNTs. The average length was determined from the difference between the zero-shear viscosity of the suspension and that of the solvent. Thereafter the relationship between viscosity and length was used to find the average length of SWCNTs ranging from 4000 to 7000 Å.

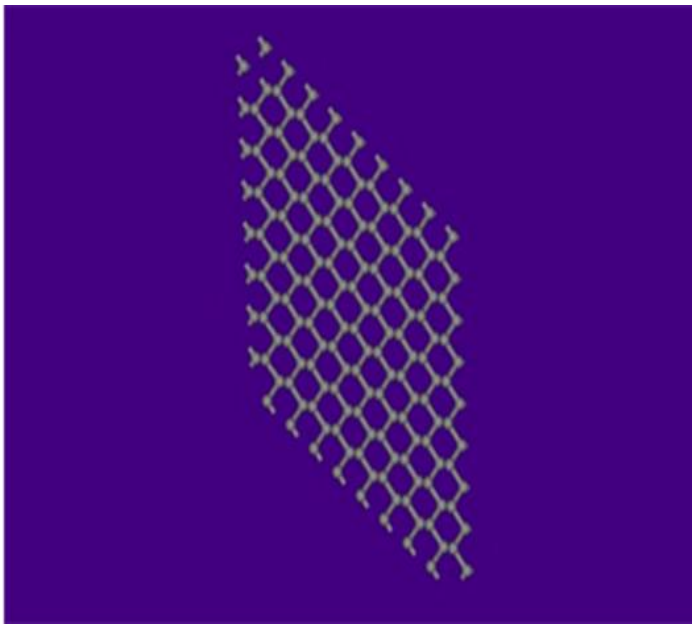

Figure 2. 1: A single layer graphene sheet

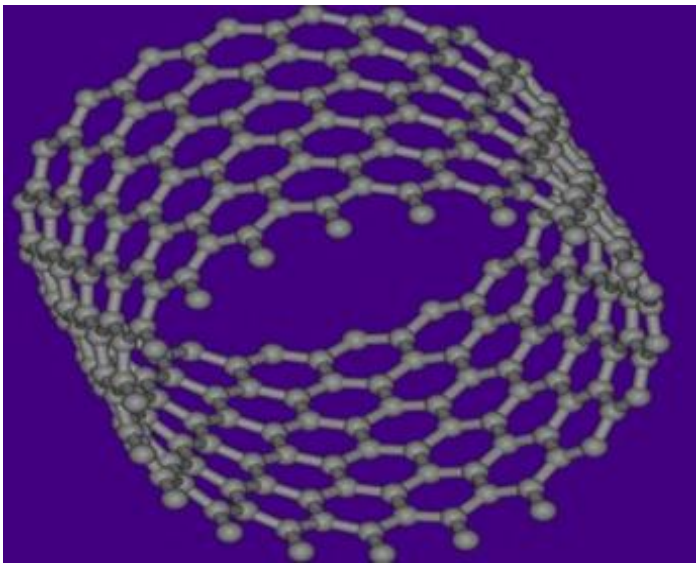

Figure 2. 2: A single-walled carbon nanotube

2.2 Electronic Properties of Graphene and Carbon Nanotube

The electronic properties help in classifying materials as metals, semi-conductors or insulators [88]. It is the size of the energy gap in these materials which plays a crucial role (the gap between the valence band orbitals and the conduction band orbitals). In the case of a metal there is no gap as there is overlap of the orbitals, for semiconductors the gap is sufficiently small for electron/hole tunnelling to occur, and in insulators the potential barrier is sufficiently large for tunnelling of particles to occur [33].

2.2.1 Graphene for Gas Sensing

Graphene is always thermodynamically stable, seldom shows any electric signals with its surroundings and has atomic dimension layered structure. These distinctive properties make it relevant for gas sensing, meaning that every atom is at the surface [33]. It is also unstable to chemical gating; changes in electrical properties that occur as chemicals on the surface donate or withdraw electrons, even a single molecule of nitrogen dioxide (NO_2) can cause a significant change in its electrical properties [34]. Once more, graphene materials have high conductivity and a large surface area that makes it to be extensively explored for the fabrication of gas sensors [35]. Studies by Kong *et al*. [36] suggest that such a device could even detect individual molecules. These types of sensors show a fast response and a substantially higher sensitivity than the solid-state type of sensors at normal temperatures [36]. The better way to understand the possibilities of graphene as a gas sensors, one has to investigate the interaction mechanism between the graphene sheet and the adsorbed atoms or molecules thoroughly [36].

The response of the graphene based device can be further boosted by functionalising its surface with catalytic metals such as Pt, Pd and Au. The important use of graphene for gas sensing is well indicated by the study of Schedin *et al.* [18], which demonstrates that once graphene is added in a multi-terminal Hall bars device, the electrical detection of the single molecule adsorbed on it can be obtained. A variety of articles about the role of graphene in detecting of different gasses have been published [41-45]. Johnson *et al*. [40] reported the ammonia (NH_3) sensing behaviour of graphitic nano-ribbons decorated with platinum (Pt) nanoparticles. Chu *et al*. [41] used Pt coated graphene surface to identify H_2 gas in various concentrations. Randeniya *et al*.

[45] reported the NH_3 gas sensing behaviour of carbon nanotubes (CNTs) functionalized with Au nanoparticles (AuNPs) and Au/Pt nano clusters, respectively. This is the evidence to show that the graphene surface integrated with AuNPs can be an attractive approach for NH_3 detection. The gas sensing behaviour of graphene depends on the concentrations of target gas and operating temperatures [46]. Varezhnikov *et al*. [47] described that, the optimizations of the graphene layer dimensions are required to increase the sensitivity and miniaturize of the array. Using mechanical exfoliated graphene, Dan *et al*. [39] detected H_2O, NH_3, octanic acid and tri-methylamine gases. Schedin *et al*. [18] detected H_2O, NO_2, I_2, NH_3, CO and C_2H_5OH with graphene down to molecular level.

Graphene shows huge sensitivity to a wide range of studies at a standard temperature, even though it is affected by the chronic handicap of the standard temperature solid state chemical gas sensors such as slow analysts desorption, low selectivity, poor electrical stability in environmental conditions [48-50].

2.2.2 Carbon nanotubes for Gas Sensing

There are different methods to integrate CNTs to several gas sensor structures. Li *et al*. [51] refined a resistive gas sensor by simply casting SWCNTs on inter-digitated electrodes (IDEs). The photolithography and evaporation of Ti and Au (600 Å in thickness together) on silicon oxide were used to fabricate the electrodes. Another easy method is screen-printing of CNTs onto patterned electrodes which was used by Lee *et al*. [52]. They screen-printed CNTs paste mixed with MWNTs, terpineol, ethyl-cellulose, and glass frits onto electrode-coated glass as the gas sensing element for NO_2 detection. The product was annealed in N_2 gas at ambient temperatures to remove the organic binder.

CNTs sensors can also be produced using the di-electrophoresis (DEP) approach. DEP is the electro kinetic motion of dielectrically polarized materials in non-uniform electric fields and has been used to manage CNTs for separation, orientation, and positioning of CNTs [53-59]. Suehiro *et al.* [60] demonstrated that the DEP fabrication could create an excellent electrical connection between CNTs and the electrodes. Jang *et al*. [61] fabricated a NH_3 gas sensor using this approach with sideways altering MWNTs. The Si base was used as N-type substrate with SiO_2 layer on top. In most cases, carbon nanotube conductivity was detected that never fall below a minimum

value corresponding to the quantum unit of conductance, even when concentrations of charge carriers tend to zero [62]. The adsorption of different gas molecules on SWNTs is mostly investigated by first-principles calculations based on density functional theory (DFT). The binding energy, tube-molecule distance, and charge transfers are investigated predominantly. Further studies on the adsorption of NO_2 on to SWCNTs was investigated by Peng and Cho [63] using the density functional theory method. According to Peng and Cho [63] studies, the binding of the NO_2 molecule with electron transfer is the microscopic mechanism for the increase conductance observed in experiments [63]. The resistance feedback of chemically functionalized nanotubes to alcohol vapours was investigated by Wang and Yeow [37] together with Sin *et al*. [38]. During this study, a purified carbon nanotube was oxidized and COOH functional group was embedded along the sidewalls of the tube that gave carbon nanotube a good acknowledgement to alcohol vapours [37-38]. Zhao *et al*. [15] investigated the adsorption of different gas molecules (NO_2, O_2, NH_3, N_2, CO_2, CH_4, H_2O, H_2, Ar) on both SWCNT and MWCNT bundles using first principles method. In their studies they explained that all molecules are ailing adsorbed on SWCNT with small charge transfer, but they can be either charge donor or acceptor of the nanotube. Again in this study they [15] also explained that the adsorption of some gas molecules on SWCNTs can cause a serious change in electronic and transport properties of the nanotube due to the charge transfer and charge fluctuation.

Kong *et al*. [36] work explained that the electrical resistance of respective semiconducting SWCNTs is seriously affected when disclosed to gaseous molecules such as NO_2, NH_3, and O_2 under gate voltage circuits. These field-effect transistor (FET) type SWCNT gas sensors present a great sensitivity and a quick response time at standard temperature. The electrical properties of respective metallic SWCNTs in different chemical environments were also studied under gate modulation. The electrical conductance fluctuations turned out to be small compared to their semiconducting counterparts [36]. Different authors have been investigating the direct growth of SWCNTs network from discriminatory aligned catalyst by chemical vapour deposition (CVD) [64]. Vermesh *et al*. [65] assembled SWCNT FET sensors by using direct CVD growth technique at 900 ºC and explained that all devices showed huge sensitive chemical gating's, which demonstrate that the charge transfer is especially through semiconducting SWCNTs.

2.2.3 Graphene for Semiconducting

The electronic properties of graphene can be altered by introducing impurities. Because of their valence electrons, boron (B) and nitrogen (N) doped diamond can have p-type and n-type conductivity respectively [68]. The doping could be extremely sensitive to the location, density, nature and dimensions of the sheet and the tube in 2-D graphene and 1-D carbon nanotube respectively. Graphene-based photovoltaic devices have brought huge interest since the current implementation of graphene/semiconductor hetero-junction solar cells. It is encouraging to see a possible value of graphene as transparent electrodes, hole collectors and junction layers because of its captivating electronic and optical characteristics [68]. Just like in diamond, Zheng *et al*. [66] discovered that depending on the distance of substitutional B or N to the perimeter, the zigzag edge graphene can either be semiconducting, half-metallic, or metallic. If extrinsic defects are introduced in the matrix, conductance of graphene can essentially increase or decrease. Kong *et al.* [36] investigated that, graphene sandwiched between two metal contacts display a field effect transistor, with thermal emission p-type characteristics. With the introduction of NO_2 in its environment, the devices conductance increase tremendously.

Tongay *et al*. [67] discovered that when CVD prepared graphene sheets are placed over n-type Si, GaAs, 4H-SiC and GaN semiconductor substrates, equilibration of the Fermi level throughout the system gives rise to a charge transfer between the graphene and the elemental IV or III-V semiconductor. This results in a huge current rectification (Schottky effect) at the interface. Beside that they discovered that graphene's Fermi level is subject to variation during charge transfer across the graphene - semiconductor interface as determined by in-situ Raman spectroscopy measurements [67]. This is very different to the conventional metal semiconductor diodes where the Fermi level of the metal does not change due to a huge density of states at the Fermi surface.

Castro *et al*. [69] discovered that, the band structure of bilayer graphene can be contained by an external applied electric field using both theoretical and experimental method so that the electric gap between the valence and conduction bands can be shifted between zero and mid infrared energies. Their studies, achieved that a

bilayered graphene was the only known semiconductor with a tuneable energy gap and it may open the way for establishing photo detectors and laser lights tuneable by electric field effect [69].

2.2.4 Carbon nanotubes for Semiconducting

Tans *et al*. in 1998 [70] described the behaviour of semiconducting in carbon nanotubes. A typical measurement of the conductance of a semiconducting SWCNT is displayed in figure 2.3 [71] as the gate voltage (V_g) applied to the conducting substrate is checked. The nanotube conducts at negative V_g, and then turns off with a positive V_g. The noticeable amount of change in resistivity occurs during the on and off state of the device. The device behaviour is comparable to a p-type metal-oxide semiconductor field-effect transistor (MOSFET), with the nanotube substituting Si as the semiconductor [72]. N-type conductance is occasionally noticed at high positive gate, particularly in bigger-diameter tubes [72-73].

Because of the work function of the Au electrodes, the conductance in the n-type region is generally less than in the p-type region [73]. The Au Fermi level gets even with the valence band of the SWCNT. This results in the p-type surface being in contact with a barrier for the injection of electrons. Semiconducting nanotubes are generally p-type at $V_g = 0$. But due to contacts and extrinsic chemical species, especially oxygen, adsorbed on the tube they may act as weak p-type dopants.

Semiconducting carbon nanotubes have been suggested for such nano-electronics applications as high-speed field-effect transistors (FETs) [70], few- or single-electron memories [72-75] and chemical or biochemical sensors [36, 76-78]. The conductivity assigned to nanotubes by the concentration density of charge carriers is important to each of the semiconducting applications. Gradient concentration mobility regulates the carrier velocity and even switching speed, in FETs [79]. Nanotube FETs can be utilised to identify charge, or a chemical signal transformed to charge in floating gate memories and chemical or biochemical sensors [76]. The change in conductivity per charge can be determined by the mobility and even the responsive of such devices. But the mobility of charge carriers in semiconducting carbon nanotubes remains poorly understood [79].

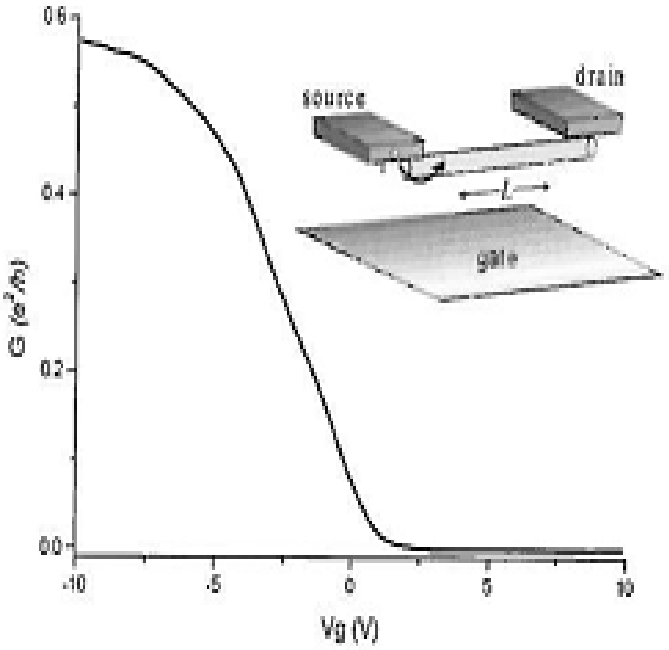

Figure 2. 3: Conductance G vs gate voltage Vg of a p-type semiconducting SWNT field effect transistor [71].

2.3 Carbon nanotubes as energy and hydrogen storage

Hydrogen is one of the greatest purified and idealized energy sources. A range of modern technologies including compression, liquefaction, metal hydride and adsorbent material have been developed for the purpose of hydrogen storage [79]. Mechanical conduct and kinetics of SWCNTs, MWCNTs, and bundles of SWCNTs have been studied thoroughly for the storage of hydrogen energy. The model tries to explain the deformation of CNTs through compression and stretching and the van der Waals interactions among hydrogen molecules and between hydrogen and carbon atoms [80]. Stretched SWCNTs create pores in the molecular dimension and are competent in adsorbing hydrogen even at high temperatures and low pressures [81]. This action is important to these materials and demonstrates that SWCNTs are the perfect building blocks for constructing safe, active and high energy density adsorbents for hydrogen storage applications [81]. Darkrim *et al.* [83] investigated some mechanical properties of CNTs which involve bending and stretch applications. Hydrogen storage is one of those promising application because carbon is great for adsorbing of gases and in addition they are micro-porous carbon macromolecules with high particular surface and have the potential to adsorb hydrogen in their nanostructures [83].

Hydrogen adsorption in CNTs was also investigated by Dillon *et al*. [82]. In that study, amounts of hydrogen adsorbed by gas desorption were accumulated. Liu *et al*. [85] studied the hydrogen adsorption in CNTs at standard temperature using semi-continuous hydrogen arc discharge method and reached the same outcomes as Dillon *et al*. [82]. Darkrim and Levesque [86] used Monte Carlo simulations to compute hydrogen adsorption in opened SWCNTs for a wide range of pressure and temperature and increased the tube diameters and the inter-tube spacing to attain a high adsorptive property. The adsorption is expressed as a unit of quantity of gas with respect to a unit of quantity of adsorbent. Dillon *et a*l [84] developed laser synthesis conditions that produce SWNTs with size and type circulations that were already found to have excellent hydrogen storage capacities of ~7 wt.%.

Liu *et al.* [85] experiments managed a hydrogen storage quantity of 4.2 w% or a hydrogen to carbon atom ratio of 0.52 which could be reproduced at standard temperature and high pressure. Chen and Huang [80] used potassium hydroxide (KOH) in order to change the properties of MWCNTs for beneficial hydrogen storage. The results showed the structure of CNTs being destructive after being altered by KOH at 550 ^{0}C in H_2 atmosphere. The analysis also showed that the quantity of hydrogen storage on the plain and KOH altered CNTs were 0.71 and 4.47 wt%, respectively, under atmosphere pressure and at balanced temperature.

For years carbon has been unconsciously a source of energy. The request for energy storage devices with high energy density and high power has endured to increase while their physical size inside electronic products has endured to decrease [87]. Since it is fascinating for energy storage devices to have flexible shapes to fit into different forms of factors, energy storage devices formed from adjustable electrodes could be interesting. There has been powerful attraction in the advanced progress of energy storage devices such as batteries [88] and super capacitors [89] over the past years.

Carbon materials have been playing an important role in the improvement of different clean and continual energy technologies [90]. The achievement of energy storage devices depends actually on the properties of the materials that are made of and the change of materials depend on the nature of the advances in energy storage [91]. Fthenakis *et al*. [92] investigated the elastic range and energy storage quantity of contorted carbon nanotubes and nanotubes ropes using ab initio and parameterised density functional calculations. In that study it was discovered that the contorted nanotube ropes may reversibly store energy by contorting, expanding, bending and compressing basic nanotubes. In addition to that, the elastic establishment and the interior of a contorted rope nanotubes encounters hydrostatic pressures of up to tens of GigaPascals (GPa).

Chapter 3

Theoretical Background

3.1 Introduction

Molecular dynamics is a simulation method that is good in explaining and predicting numerous properties of materials in solid and liquid phase. Computer simulations facilitate a connection between microscopic length and time scales and the macroscopic world of the laboratory [93]. The buried detail behind bulk measurements can be exposed at the same time. The relationship between the diffusion coefficient and velocity autocorrelation function is one of an example. Lately researchers use simulations as an association between theory and experiment:

Theory ⇋ Computer simulations ⇌ Experiments.

By running a simulation, a theory may be proven using the same model and correlate the test model with experimental results [93], in another case the results might be in concurrence but sometimes they are contrasting. A good advantage of simulations is that they may also be carried out on variables that are impossible or absurd to archive in the laboratory (for an example; working at high temperature or pressure). Consider a scenario of modelling a large-scale semiconductor system (about 10^6 atoms). Here a computationally reasonable and accurate interatomic potential will be essential. For example, a plain structural relaxation of crystals with small strain, the well-established Lennard-Jones potential is acceptable [96]. This potential is quite capable of calculating quantities like bond lengths and elastic constants. When calculating parameters like Grüneisen parameters or specific heat capacity more specialised potentials maybe desired [97].

3.2 Molecular Dynamics

Molecular dynamics (MD) is a design of computer simulation in which atoms and molecules are granted to collaborate for a period of time by estimations of known physics, giving an aspect of the motion of the particles. Most of the time is commonly used in the study of materials physics, chemistry and biology [93]. MD is inviting,

though not completely correct to explain the technique as a "virtual microscope" with high material and spatial resolution. It allows scientists peer into the motion of individual atoms in a form which is impossible in laboratory experiments. Simulations can consistently be protracted to cover longer time periods and the modelled systems can consistently be made larger than the largest systems investigated so far. In addition, the models can again be more precise and brought closer to the importance of physics [100]. This technique can be considered as a specialized field of molecular modelling and computer simulation based on statistical mechanics. The predominant reason of the MD method is that, statistical ensemble averages are alike to time averages of the system which is called the ergodic hypothesis. Furthermore, molecular dynamics simulations produce information at the microscopic level, containing atomic positions, velocities and forces. Quantities like energy, pressure, heat capacity; need statistical mechanics in order to be transformed from microscopic to macroscopic level. Statistical mechanics is basically used to the study of material science by molecular dynamics simulation. The molecular dynamic has a great advantage over Monte Carlo methods, which contributes a route to dynamic properties of the system, which are transport coefficients, time-dependent reaction to perturbations, rheological properties and spectra [98].

3.3 Verlet Algorithm

In molecular dynamics, the most frequently used time integration procedures is the Verlet algorithm [104]. This can be obtained by writing two 3rd -order Taylor expansions for the positions $r(t)$, one forward and one backward in time, where $v(t)$ is the velocity and $a(t)$ the acceleration of the particle [100]. Generally there are velocity Verlet and the leap-frog Verlet algorithms. The Verlet algorithm is derived from Taylor expansions for the position [97]:

$$r(t+\Delta t) = r(t) + v(t)\Delta t + \frac{1}{2}a(t)\Delta t^2 + \frac{1}{6}\dot{a}(t)\Delta t^3 + \mathcal{O}(\Delta t^4) \quad (3.1)$$

$$r(t-\Delta t) = r(t) - v(t)\Delta t + \frac{1}{2}a(t)\Delta t^2 - \frac{1}{6}\dot{a}(t)\Delta t^3 + \mathcal{O}(\Delta t^4) \quad (3.2)$$

Adding the two equation gives

$$r(t+\Delta t) = 2r(t) - r(t-\Delta t) + a(t)\Delta t^2 + \mathcal{O}(\Delta t^4) \quad (3.3)$$

Equation 3.3 is the basis of the Verlet algorithm. Because the Newton's equations are the one which are integrated, $a(t)$ is just the force divided by mass, and the force is in turn a function of the positions $r(t)$.

In this procedure, the discrepancy is evident when developing the system by Δt which is of the 4th order (Δt^4), even though a third derivative does not come into sight certainly. In explaining the larger recognition among molecular dynamics simulators, the Verlet algorithm is simple to implement, precise and balanced. A disadvantage with this form of the Verlet algorithm is that velocities are not precisely created. Even though they are not wanted with time evolution their knowledge is frequently essential. However, they are enforced to calculate the kinetic energy *K*, whose calculation is precisely to evaluate the conservation of the total energy

$$E = K + V. \qquad (3.4).$$

V is the potential energy. This is one of the most valuable tests to confirm that an MD simulation is proceeding accurately. One could calculate the velocities from the positions by using

$$v(t) = \frac{r(t+\Delta t) - r(t-\Delta t)}{2\Delta t}. \qquad (3.5)$$

Nevertheless, the error connected to this expression is of order Δt^2 rather than Δt^4. To solve this complication, a few variations of the Verlet algorithm as mentioned in this chapter have been advanced. They give improvement to absolutely the same trajectory and differ in variables that are stored [100].

3.3.1 Leapfrog Verlet method

The leapfrog method is generally used to clarify numerically, basic boundary value complication for partial differential equations (PDEs). It is interesting because it is clear 2nd -order and has a short memory, but mainly because it has an outstanding stability when calculating oscillatory motion solutions. Some algorithmic methods for PDEs are frequently studied by considering them as arising from the method of lines (semi-discretization) [104]. Leapfrog integration is a simple method for integrating equations, particularly in the case of a dynamical system. The method is known by various names in various disciplines [100]. By Newton's 2nd law and basic mechanics,

$$F = ma. \quad (3.6)$$

F stands for the force on the particle, m is the mass of the particle, and a is the acceleration of the particle [102].

$$a(t) = \frac{dv(t)}{dt}, \quad (3.7)$$

$$v(t) = \frac{dr(t)}{dt}. \quad (3.8)$$

In this case position (r) and force (F) at time t are wanted while the velocities (v) are half a time step behind. Firstly the velocities are advanced by $t + \frac{\Delta t}{2}$

$$v(t + \tfrac{\Delta t}{2}) = v(t - \tfrac{\Delta t}{2}) + a(t)\Delta t \ , \quad (3.9)$$

then positions,

$$r(t + \Delta t) = r(t) + \ v(t + \tfrac{\Delta t}{2})\Delta t. \quad (3.10)$$

The velocity equation is considered first to produce a new mid-step velocity. This velocity is then used to compute the new positions. The velocity is computed from

$$v(t) = \left(\tfrac{1}{2}\right) v\left(t + \tfrac{1}{2}\Delta t\right) + (\tfrac{1}{2}) v(t - \tfrac{1}{2}\Delta \mathrm{t}). \quad (3.11)$$

Another advantage of leapfrog method is that, the temperature scaling using velocity scaling is achievable [103].

3.3.2 Velocity Verlet method

In the velocity Verlet algorithm the velocity is applied directly and this method is beneficial when calculating time-correlation functions e.g. $[v(t)v(0)]$ and transport coefficients (e.g., the diffusion coefficient D) [106].

The calculations of the time-correlation functions require sampling of the initial conditions according to the ensemble distribution explained by D and for each initial condition calculate the value of the particle velocity $v(t)$ at time t. The equation that is used to calculate the ensemble average is expressed below as:

$$v(t)v(0) = \frac{1}{T}\int_0^T Dt' v(t' + t)\, v(t'), \quad (3.12)$$

where T is the period of the measurement of the diffusion constant D, a time that is much larger than the relaxation time of the velocity autocorrelation function [105].

Molecular dynamics simulations can supply the arrangement of microscopic configurations through which the model system passes in time. Such accurate microscopic information allows one to calculate the result of a measurement of an observable according to the time average. This can be explained by easily averaging the value of the observable through the whole multiple of microscopic configurations produced during the time of the measurement.

The velocity Verlet algorithm for application in molecular dynamics is given by

$$r(t + \Delta t) = r(t) + \Delta t v(t) + \frac{1}{2}\Delta t^2 a(t), \quad (3.13)$$

$$v(t + \Delta t) = v(t) + \frac{1}{2}\Delta t[a(t) + a(t + \Delta t)]. \quad (3.14)$$

The above velocity Verlet concept can be exposed to be similar to basic Verlet algorithm by removing the velocities. There are two stages that can be used to implement the above equations. The first stage is to compute the new positions at time $t + \Delta t$. In the second stage the velocities at mid-step are computed using

$$v\left(t + \frac{1}{2}\Delta t\right) = v(t) + \frac{1}{2}\Delta t a(t) \ . \quad (3.15)$$

The forces and accelerations at time $t + \Delta t$ are then computed so that the new velocity is computed [105] to be

$$v(t + \Delta t) = v\left(t + \frac{1}{2}\Delta t\right) + \frac{1}{2}a(t)\Delta t. \quad (3.16)$$

3.4 Bond Order Potential

The forces between atoms which are derived from quantum and statistical mechanics are called bond order potentials. Different from classical empirical potentials, bond order potentials capture bond formation and breaking, saturated and unsaturated bonds, dangling bonds and radical bonds, as well as single, double or triple bonds. The bond order potentials supply an equivalent accuracy as tight-binding calculations at less computational effort, and again they pave the way to larger scale atomistic simulations of systems which cannot be explained by classical empirical potentials [108]. Examples of bond order potentials that will be reviewed in this section are Tersoff potentials, Brenner potentials, Finnis-Sinclair potentials and Stillinger-Weber potentials. They have advantage over other interatomic potentials because whilst using same parameters they can explain numerous bonding states of an atom and in some cases might be able to explain chemical reactions perfectly. All these potentials were developed partly independent of each other, but contribute the same conclusion that the stability of a chemical bond depends on the bonding environment, that include the number of bonds and perhaps also angles, bond length and order. These potentials are based on the Linus Pauling bond order concept, which can be expressed in the form of

$$V_{ij}(r_{ij}) = V_{repulsive}(r_{ij}) + b_{ijk}V_{attractive}(r_{ij}). \quad (3.17)$$

In the above equation the potential field is written as uncomplicated pair potential relying on the distance between two atoms r_{ij} , but the stability of this bond is altered by the environment of the atom i via the b_{ijk} term. Preferably, the potential can be expressed in the form of

$$V_{ij}(r_{ij}) = V_{pair}(\vec{r}_{ij}) - D\sqrt{\rho_i}\ , \quad (3.18)$$

where ρ_i is defined as the electron density at the location of atom i. Algebraically it can be shown that equation 3.17 and 3.18 are equivalent [108-114].

3.4.1 Tersoff Potentials

Originally, the Tersoff potential was created to recreate the effects of covalent bonding in systems composed of group 4 elements on the periodic table (carbon, silicon, germanium etc) and their alloys. Just like the metal potentials, the Tersoff potential is

also non-bonded potentials defined by atom types instead of specific atomic indices. The potential energy definition yields balanced planar graphite layers as well as a balanced diamond phase for carbon, both with appropriate densities and binding energies [109]. As mentioned earlier on the Tersoff potential is based on the approach of bond order. This is because the strength of a bond between two atoms may not be stable, but rely on the local environment. This concept is equivalent to that of the ``glue model'' for metals, to use the coordination of an atom as the variable controlling the energy. However in semiconductors, the target is on bonds instead of atoms, that is where the electronic charge is sitting in covalent bonding [112]. Due to the content of the implementation and the physical catalyst of the Tersoff potential, it has been generally used for molecular dynamics research [109-112].

A Tersoff potential has the presentation of a pair potential:

$$E = \sum_i E_i = \frac{1}{2}\sum_{i \neq j} V_{ij} \tag{3.19}$$

$$= \frac{1}{2}\sum_{ij} \emptyset_R\left(r_{ij}\right) + \cdots + \frac{1}{2}\sum_{ij} B_{ij}\emptyset_A\left(r_{ij}\right) + \cdots, \tag{3.20}$$

where the potential energy is broken down into a site energy E_i and a bonding energy V_{ij}, r_{ij} is the distance between i and j, $\emptyset_R$ and $\emptyset_A$ means ``repulsive'' and ``attractive'' pair potentials respectively [111].

$$\emptyset_R\left(\vec{r}_{ij}\right) = Ae^{(-\lambda_1 r_{ij})}, \tag{3.21}$$

$$\emptyset_A\left(\vec{r}_{ij}\right) = -Be^{(-\lambda_2 r_{ij})}, \tag{3.22}$$

where A, B, λ_1 and λ_2 are parameters of the potential; B_{ij} is not consistent which is the bond order for *i* and *j,* it is a decreasing function of coordination G_{ij} assigned to the bond:

$$B_{ij} = B\left(G_{ij}\right) \tag{3.23}$$

G_{ij} is given by

$$G(\theta_{ij}) = \sum_k F_c\left(\vec{r}_{ij}\right) g(\theta_{jik}) F(\vec{r}_{ij} - \vec{r}_{ik}), \tag{3.24}$$

where$F_c(r_{ij})$, $F(\vec{r}_{ij}-\vec{r}_{ik})$ and $g(\theta_{ijk})$ are applicable functions.

$$g(\theta_{ijk}) = 1 + \frac{c_i^2}{d_i^2} - \frac{c_i^2}{d_i^2+\left(h_i - cos(\theta_{ijk})\right)^2}\,, \tag{3.25}$$

where θ_{ijk} is the bond angle between bonds ij and ik. The parameters c, d, and h rely only on atom i.

$$F_c(\vec{r}_{ij}) = \begin{cases} 1 & r_{ij}<R_{ij} \\ \frac{1}{2} + \frac{1}{2}.cos\left(\pi.\frac{r_{ij}-R_{ij}}{S_{ij}-R_{ij}}\right) & R_{ij}<r_{ij}<S_{ij} \\ 0 & S_{ij}<r_{ij} \end{cases}. \tag{3.26}$$

The Tersoff functional is not like Stillinger-Weber potential, its arrangement consists of an accurate cut-off term [109,117]. The step function in equation 3.26 is created to design a smooth transition between the separation ranges of R and S.

The important idea is that the bond ij is depleted by the existence of other bonds ik including atom i. The quantity of weakening is determined by where these other bonds are located. Angular terms come out basically to build up a realistic model [112]. This theory works in an expansive spectrum of positions than the Stillinger-Weber potential which is very equivalent with the Tersoff potential; nevertheless it is not relived from the problems. One of the biggest problems with this theory is that it may be not easy to fit parameters: with 6 functions to fit and angular terms, finding an excellent parameterization is a difficult effort [113].

3.4.2 Brenner Potentials

The bond-order Brenner potential was advanced especially for learning the covalent bonds found in carbon based materials. In Brenner potential each atom in the system has mutual dependence on its nearest neighbours [113-116]. The total potential energy of the system combined via the Brenner potential can be expressed in the form of

$$U_{tot} = \frac{1}{2}\sum_{i=1}^{N}\sum_{\substack{j=1 \\ j\neq i}}^{N} U_{ij} = \frac{1}{2}\sum_i \sum_{i\neq j} F_{cut}(r_{ij})\,[U^{(R)}(r_{ij}) - B_{ij}U^{(A)}(r_{ij})], \tag{3.27}$$

where $F_{cut}(r_{ij})$ is the cut-off function, which limits the interaction of an atom to its nearest neighbours and is defined as:

$$F_{cut}(r)_{ij} = \begin{cases} 1, & r_{ij} \leq R_1 \\ \frac{1}{2}\left[1+\cos\left(\frac{r_{ij}+R_1}{R_2-R_1}\pi\right)\right], & R_1 < r_{ij} \leq R_2 \\ 0, & r_{ij} > R_2 \end{cases}. \quad (3.28)$$

Here R_1 and R_2 are the parameters which determine the range of the potential. The functions $U^R(r_{ij})$ and $U^A(r_{ij})$ are the repulsive and the attractive energy terms of the potential respectively. The Brenner potential involves the following parameterization for $U^R(r_{ij})$ and $U^A(r_{ij})$:

$$U^R(r_{ij}) = \frac{D_e}{S-1}\exp[-\sqrt{2S\beta}(r_{ij}-R_0)], \quad (3.29)$$

$$U^A(r_{ij}) = \frac{D_e}{S-1}\exp[-\sqrt{\frac{2}{S}}\beta(r_{ij}-R_0)], \quad (3.30)$$

where D_e, S, β and R_0 are parameters. The factor B_{ij} in equation 3.27 is the called bond order term, which is written as

$$B_{ij} = \left[1+\sum_{k\neq ij} F_{ij}(r_{ik})G(\theta_{ijk})\right]^{-\delta} = [1+\zeta\_ij\,]^{-\delta}. \quad (3.31)$$

The function $G(\theta)_{ijk}$ is written as

$$G(\theta_{ijk}) = a_0\left[1+\frac{c_0^2}{d_0^2}-\frac{c_0^2}{d_0^2+(1+\cos\theta_{ijk})^2}\right], \quad (3.32)$$

where c, d and a have the same meaning as in equation 3.22 and θ_{ijk} is the angle between bonds produced by pairs of atoms (i,j) and (i,k), written as,

$$\cos(\theta_{ijk}) = \frac{r_{ij}.r_{ik}}{r_{ij}r_{ik}}. \quad (3.33)$$

3.4.3 Finnis-Sinclair Potentials

Finnis-Sinclair (FS) potential is an important type of embedded atom model (EAM) for base centred cubic type materials. The bonding terms of this model potential are the square-root of a site density ρ_i, summed over atoms i, and a repulsive pairwise term

[118]. The sum over neighbouring sites j of a cohesive potential $\varphi(R_{ij})$ is explained as the site density ρ_i . Both the potential and density fields are assumed to be short-ranged and are parameterized to fit the lattice constant, cohesive energy and elastic modulus of many body-centred-cubic (BCC) transition metals [118]. The FS potential can be expressed as

$$U_{FS} = U_n + U_p \ , \tag{3.34}$$

where U_n is the repulsive pairwise term, which can be written as

$$U_n = \frac{1}{2}\sum_{ij} V(r_{ij}), \tag{3.35}$$

and U_p is the bonding term, which can be written as

$$U_p = A\sum_i \sqrt{\rho_i} \ , \tag{3.36}$$

so that a complete FS potential is

$$U_{FS} = \frac{1}{2}\sum_{ij} V\left(r_{ij}\right) - A\sum_i \sqrt{\rho_i} \ , \tag{3.37}$$

where r_{ij} is inter atomic distance between atoms *i* and *j*. The density for each atom is written as

$$\rho(r_i) = \sum_{i\neq j} \emptyset(r_{ij}) \ , \tag{3.38}$$

$$\emptyset\left(r_{ij}\right) = \begin{cases} (r_{ij} - d)^2 & r_{ij} \geq d \\ 0 & r_{ij} > d \end{cases} \ , \tag{3.39}$$

where d is a fitting parameter. The repulsive part is a fourth-order polynomial, which can be expressed as

$$V\left(r_{ij}\right) = \begin{cases} ((r_{ij} - c)^2(c_0 + c_1 r_{ij} + c_2 r_{ij}^2)^2 & r_{ij} \leq c \\ 0 & r_{ij} > c \end{cases} , \tag{3.40}$$

where c_0, c_1, c_2 and c are the fitting parameters.

3.4.4 Stillinger-Weber potential

The Stillinger-Weber (SW) potential [119] is the first interatomic potential applied to model semiconductors using classical theory. This potential model is still one of the best used in empirical potential formats for the simulation of open structure materials. This is because of its combination with ease of implementation and acceptable predictive effectiveness. It is based on a two-body term and a three-body term:

$$V = \frac{1}{2}\sum_{ij} \emptyset(r_{ij}) + \sum_{ijk} g(r_{ij})\, g(r_{ik}) \left(cos\theta_{ijk} + \frac{1}{3}\right)^2, \quad (3.41)$$

where θ_{ijk} is the angle produced by the ij and ik bonds, and $g(r)$ is a decaying function with a cut-off between the first and the second neighbour shell. The intent is clear and support those configurations where,

$$cos(\theta_{ijk}) = -\frac{1}{3}.$$

This only occurs where angles are very close to those angles that are found in diamond like tetrahedral structure, and cause this structure more stable than compact structure, as it should.

In that case equation 3.41 becomes,

$$V = \frac{1}{2}\sum_{ij} \emptyset(r_{ij}). \quad (3.42)$$

3.5 Statistical Ensemble

Statistical ensemble is an idealization consisting of a big number of mental copies (occasionally infinitely many) of a system, studied all at once, each of which represents an achievable state that the actual system might be in. The American scientist whose name was Willard Gibbs [120] was the first scientist to introduce ensemble theory. An ensemble is itself an organised learning procedure, because it can be practised thereafter applied to trigger expectations. The ensemble theory is generally used to achieve the particle circulation at kinetic and thermal equilibrium. The ensemble theory is based on the ergodic hypothesis. In this section three types of ensembles which are

micro-canonical ensemble, canonical ensemble and isothermal-isobaric ensemble are discussed.

3.5.1 Ergodic Hypothesis

The ergodic hypothesis is important to statistical mechanics, which was first put forth by Boltzmann more than a hundred years ago, before the time of quantum mechanics [121]. It is an approach utter in classical concept, and it is designed for classical many-body systems [121]. In physics and thermodynamics in partcular, the ergodic hypothesis state that, over long periods of time, the time spent by a particle in some region of the phase space of microstates with an equal energy is directly proportional to the volume of this region, this means that all available microstates are equally possible over a long period of time.

3.5.2 Micro-canonical Ensemble

A micro-canonical ensemble (NVE) is an ensemble produced by an enclosed system. Such an ensemble is easy to reproduce because of the total energy of an enclosed system, which means the internal energy remains constant in an MD simulation. In micro-canonical ensemble, the parameters that normally explain the macroscopic condition of the system are the energy E, the volume V, and the particle number N. Since this ensemble coincides with an isolated system, the energy remains constant [122].

3.5.3 Canonical Ensemble

Canonical ensemble (NVT) is the type of ensemble that has a number of thermodynamic control parameters in order to give back more acceptable experimental results. In this case, energy fluctuations are acknowledged because the system has been located in exactly at a thermal contact with an external heat bath, or temperature reservoir, the temperature of which is recognised at T [123]. In canonical ensemble, the macroscopic state of the system is described by the variables N, V, and T, which describe a system in thermal contact with an absolute heat source. Accordingly, temperature normally appears in different canonical ensemble averages, by which one can achieve advantageous relationship between the temperature of the external bath and averages of different mechanical quantities.

3.5.4 Isothermal-Isobaric Ensemble

Isothermal-isobaric ensemble (NPT) is a set of Newton's equations of motion depicting the time change of a system of N particles exposed to a coherent external pressure. Here a projectile particle which singularly regulates the system volume V is introduced. The projectile particle is described as at least one particle existing in the shell element dV surrounding spherical volume V, and is required to produce phase-space trajectories that adapt to a new reformulations of the isothermal-isobaric NPT ensemble [124].

3.6 Introduction of DL_POLY code

DL_POLY is a molecular dynamics simulation programme written at Daresbury Laboratory by W. Smith and T.R. Forester [125]. The proprietor of this software is Central Laboratory of the Research Councils in UK. DL_POLY Classic is created to conform on a duplicated data parallelism. The software is able to simulate as much as 30 000 particles in up to 100 processors. It has been designed such that it can work on personal computers as well as supercomputers with very little modification.

The most notable feature of this package is scaling up simulation from a workstation to a powerful parallel machine. In addition, DL_POLY package has an accompanying Graphical User Interface (GUI) written specifically for the software using Java programming language. The Java programming environment is an open source quite appropriate for building graphical user interfaces [124]. One of an interesting condition of java is the flexibility of the compiled GUI, which may be run without recompiling on any Java backed machine. Results in chapter 4 and 5 of this dissertation are based on DL_POLY classic package.

Chapter 4

Molecular dynamics simulation of structural and thermodynamic properties of bilayer graphene

4.1 Introduction

The structure of graphene, a single layer of carbon atoms densely arranged in honeycomb crystal lattice is baffling. It shows to be closely two dimensional (2D) and present such a high crystal quality that electrons can travel submicron distance without scattering [126]. However, in both theory and experiments, this excellent 2D crystal cannot exist in a free state [7]. This is usually because, all graphene structures investigated so far were essential part of large 3D structures, backed by a bulk substrate or embedded in 3D matrix [127]. A pure graphene monolayer can be cut into stretched layers to form 1D structure, this 1D structure is called graphene nano-ribbons (GNRs) which can be abolished by either armchair or zigzag edges. Depending on the type and width of edges of GNRs, it can either be metallic or semiconducting. Kunstmann *et al*. [128] investigated the stability of edge states and edge magnetism in zigzag edge graphene nano-ribbons, and they pointed out that the magnetic edge states might not exist in actual systems or at standard temperature.

Two monolayers of GNR can be called a bilayer GNR, and it is commonly arranged in the Bernal (AB or AA) stacking arrangements. These bilayer systems with smooth edges have been profitably manufactured by a freely multi-walled carbon nanotubes (MWCNT), the plasma engraving and chemical course [129]. If a single-layer graphene (SLG) and bilayer graphene (BLG) are undoped, they are seamless semimetals, but shippers in SLG have linear dispersion whereas in BLG the dispersion is quadratic. The quantization laws for the integer quantum Hall effect are not the same for SLG and BLG. A manageable gap can be opened with an external electric field in BLG, because it causes it to be especially fascinating for application. BLG also has a different weak localization behaviour from SLG and other two-dimensional systems. The properties of BLG have been interpreted under the expectation that the stacking of the two layers takes the form of an AB or Bernal stacking, which is common in graphite [130]. The covalent bonds between nearest-neighbour carbon atoms in graphene are formed by sp^2-hybridised orbitals [10]. The carbon-carbon bond length

of graphene is 1.42 Å with the interplanar spacing of 3.35 Å [7], the lattice constant of graphene is found to be 2.460 Å [7]. In this chapter the results of the structural and thermodynamics properties of bilayer graphene are presented

4.2 Results and Discussion [131]

In this chapter computational studies of the structural, equilibrium and thermodynamics properties of bilayer graphene (BLG) are presented [131]. Each double layer is a hexagonal arrangement of carbon atoms at the corners to make up a two dimensional honeycomb sheet. One model consists of 64 carbon atoms of which 32 atoms make one layer (graphene64); the other model has 256 carbon atoms with 128 atoms per layer (graphene256). Graphene64 and graphene256 are modelled with interplanar spacing of 7 Å and 15 Å. The hexagonal sheets have a two carbon atom unit cell with a lattice constant a_0 = 2.461 Å [133]. Each carbon atom per sheet has three nearest neighbours, six next-nearest neighbours, and three second-nearest neighbours. The scope of the simulations is to investigate the structural configuration, the equilibrium properties and the energetics with varying temperature that govern the nano-size in a given structure. In order to fully understand these effects, it is essential to perform molecular dynamics (MD) simulations at an atomistic level and a sequential resolution in the scale of the Debye frequency for thermodynamic properties. The Tersoff potential has been the most successful model to replicate much of the semiconducting properties in carbon structures [112]. Atomistic interactions are tackled by the potential energy function in the form of an interactive empirical bond-order potential.

4.2.1 Structural properties of bilayer graphene (BLG)

In the present work, focus will be on the bilayer graphene (BLG) structures. The MD simulation is performed within a canonical NVT ensemble, using DL_POLY software introduced in section 3.6 [7]. The Newtonian equations of motion are integrated with a routine based on the leapfrog Verlet algorithm with the time step of 1.0 x 10^{-3} s at a 0.0 atm pressure. Radial distribution functions were observed at every temperature from 300 K to 5000 K. For equilibrium properties we varied only the lattice constant at 300 K. All the equilibrium calculations were performed at temperature of 300 K. Iterations were performed over 2000 time steps with equilibration after every 200 steps. This step is very important and aims to calculate for each atom and generate at

each time step, a new positions and velocities. After that a frequency distribution of atomic separations is produced to compute the pair distribution function, and other various properties which are computed along the trajectory of the system in the phase space. Real space cut off and primary neighbour cut off was 2.68 Å. Some typical bilayer graphene structures at various temperature simulations are shown from figure 4.1 through to figure 4.4. Figure 4.1 and 4.2 are the structures of bilayer graphene at temperatures of 300 K and 5000 K, respectively. At 5000 K which is above the melting point, simulations predict that the structure changes the shape and atom C12 and C61 are not attached to any atom in the structure. Figure 4.3 and 4.4 are the structures of bilayer graphene256 at 300 K and 5000 K, respectively. At 5000 K above the melting point of graphene, the structure suggests C1 atom is not attached to any atom.

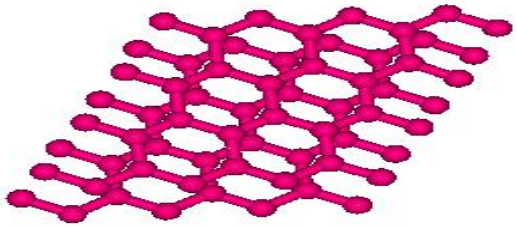

Figure 4. 1: A bilayer graphene64 configuration at 300 K.

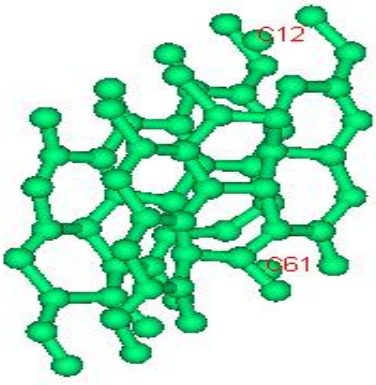

Figure 4. 2: A bilayer graphene64 configuration at 5000 K.

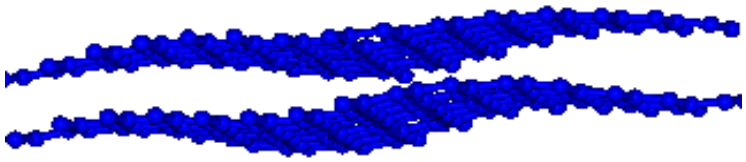

Figure 4. 3: A bilayer graphene256 configuration at 300 K.

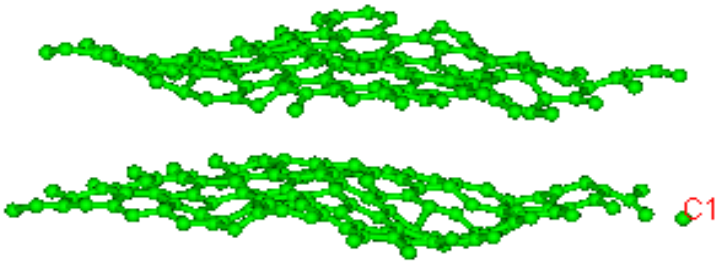

Figure 4. 4: A bilayer graphene256 configuration at 5000 K.

4.2.1.1 The radial distribution function (rdf's) of bilayer graphene (BLG)

The radial distribution function (rdf) is an effective way of describing the average structure of disordered molecular systems such as liquids, but it is also helpful when looking at disordered and ordered solids [132]. The rdf from molecular dynamics trajectory data is a common and computationally expensive analysis task. The rate limiting step in the calculation of the rdf is building a histogram of the distance between atom pairs in each trajectory frame. To test the reliability of the Tersoff potential in describing graphene, rdf's $(F(r))$ of these BLG configurations was calculated.

From peak positions of $F(r)$, the most probable distance between the atoms can be noted. In figure 4.5 and 4.6, the first peak which is associated with the first nearest neighbour parameter (r_1) appears at 1.43 Å for 300 K and 3000 K. At 5000 K which is above melting point of graphene, the first nearest neighbour parameter increases to 1.46 Å for graphene64 and 1.48 Å for graphene256. The second peak which is associated with the second nearest neighbour parameter (r_2) appears at 2.48 Å for 300 K and 3000 K. At 5000 K the second nearest neighbour parameter increases to 2.50 Å for graphene64 and 2.56 Å for graphene256. The first peak is associated with the bond length of graphene which is 1.42 Å, and the second peak is associated with the lattice parameter of graphene which is 2.46 Å [7,133]. The results for both models at 5000 K, shows that, the bond length of the material is stretching, because some of the atoms have started to melt. The number of atoms around the first nearest neighbour parameter is represented by n_1 and the number of atoms around the second nearest neighbour parameter is represented by n_2. When the temperature is increased for both models, the number of atoms around the first and second nearest neighbour parameters is decreasing. This is because at a high temperature some of the atoms are disappearing suggesting some sort of evaporation. When the number of atoms is increased in graphene, the number of atoms around those nearest parameters is increasing. These rdf's results of graphene are in agreement with both the theoretical calculations and the experiments [134-135]. A summary of this discussion is tabulated in tables 4.1 and 4.2.

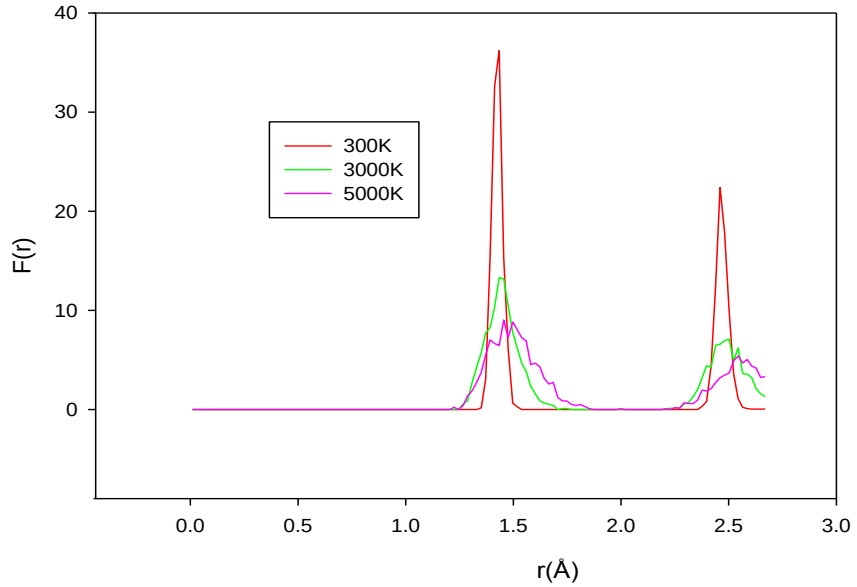

Figure 4. 5: The radial distribution functions of graphene64.

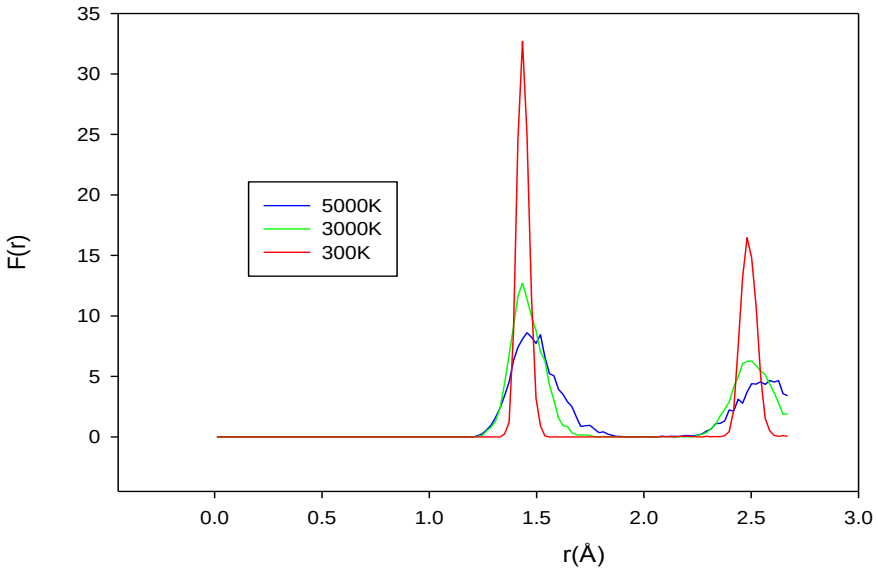

Figure 4. 6: The radial distribution functions of graphene256.

Table 4. 1: Bilayer graphene64 rdf results

	300 K	3000 K	5000 K
r_1(Å)	1.43	1.43	1.46
r_2(Å)	2.48	2.48	2.50
n_1	3.78	3.18	2.72
n_2	2.15	0.48	0.11

Table 4. 2: Bilayer graphene256 rdf results

	300 K	3000 K	5000 K
r_1(Å)	1.43	1.43	1.48
r_2(Å)	2.48	2.48	2.56
n_1	3.80	3.30	2.86
n_2	2.30	0.56	0.14

4.2.1.2 Equilibrium properties of bilayer graphene (BLG)

Figures 4.7 and 4.8, show cohesive energy as function of lattice constant for graphene64 and graphene256, respectively. The subsequent two graphs were used to calculate the equilibrium properties. In order to find the most favourable equilibrium structural configuration for the double layer graphene64 and graphene256, both structures were optimized.

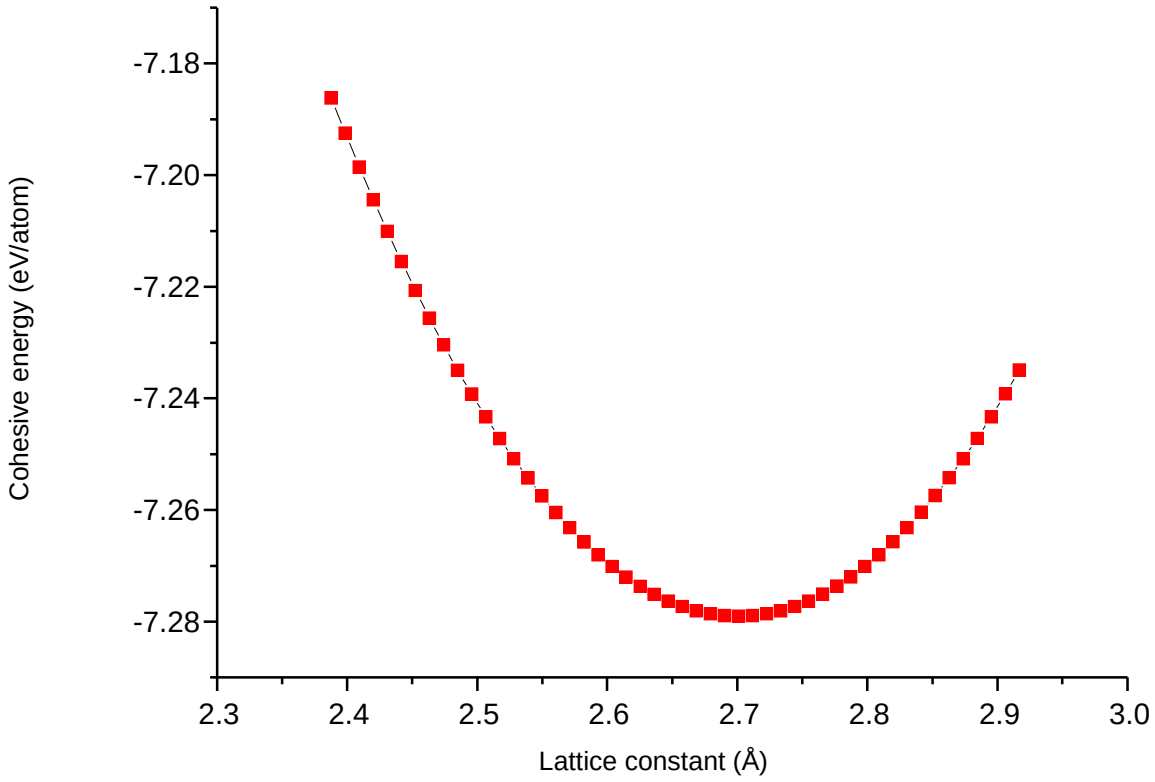

Figure 4. 7 : Cohesive energy as a function of lattice constant in graphene64.

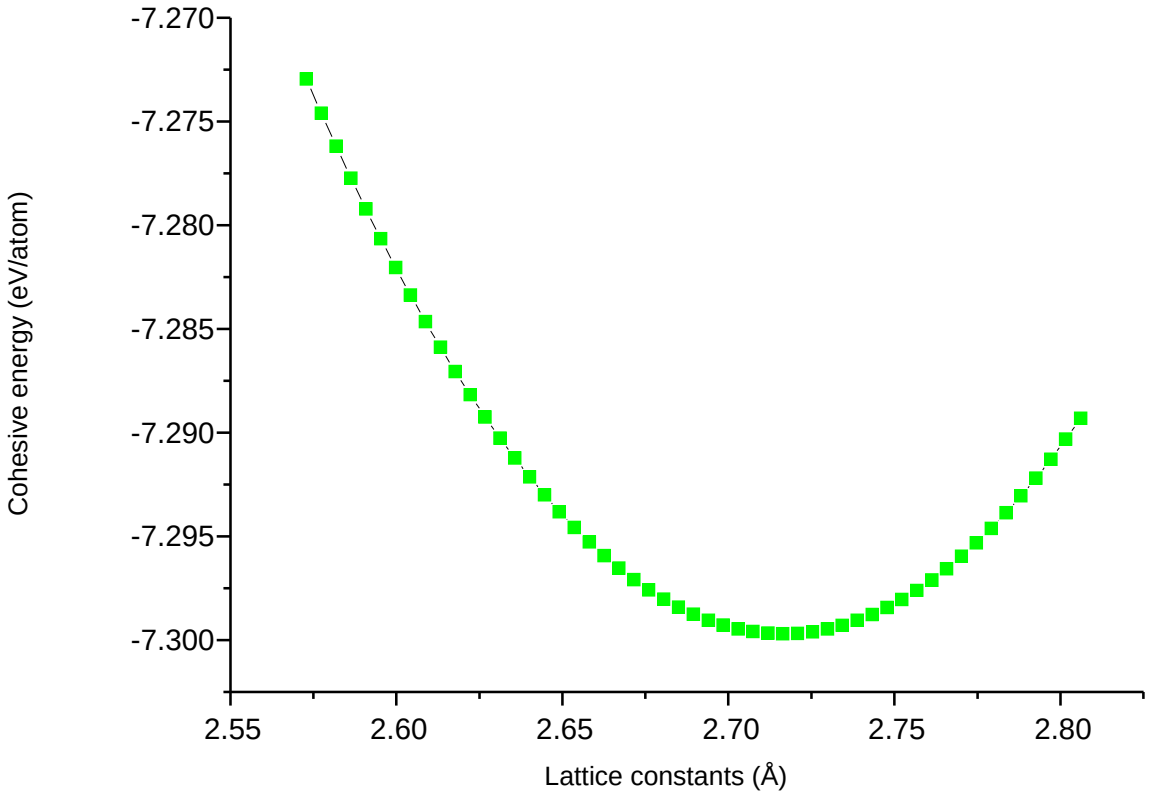

Figure 4. 8: Cohesive energy as a function of lattice constant in graphene256.

The lattice constant, the cohesive energy, volume, bulk modulus and its derivative were calculated, least squares fitted to the Murnaghan's equation of state [136]. Equilibrium energy $E(a)$ is found to be [136]:

$$E(a) = a_0 + \frac{9V_0B_0V_0}{16}\left[\left(\frac{a_0}{a}\right)^2 - 1\right]^2 + A\left[\left(\frac{a_0}{a}\right)^3 - 1\right]^3 + B\left[\left(\frac{a_0}{a}\right)^2 - 1\right]^4 + 0\left[\left(\frac{a_0}{a}\right)^2 - 1\right]^5, \quad (4.1)$$

where B_0 is the bulk modulus, V_0 the primitive volume and A and B are fit parameters. The Murnaghan equation of state or even polynomial function would fit equally well the calculation of the minimum curve.

In table 4.3, results achieved are listed together with some measured and calculated results [7, 20,95]. The lattice constants are in good agreement with the measured [131] and calculated values [7, 20]. Lattice constant of graphene64 differs from the calculated one by 9% and from the experimental one by 9%. Lattice constant of graphene256 differ from the calculated one by 10% and from the experimental one by 10%. The cohesive energy differs from the calculated one by 1% and from the experimental one by 4%. Cohesive energy of graphene256 differs from the calculated one by 1% and from the experimental one by 4%. The minimum volume of graphene64 differ from the calculated one by 20% and graphene256 from the calculated one by 11%. This shows that graphene256 is more stable than graphene64. Although the bulk modulus of graphene64 differs from the calculated one by 4% and graphene256 differ from the calculated one by almost 50%, we can say that the bulk modulus of graphene256 is totally disagreeing with other calculated one and graphene64 agrees with the calculated one, it should also be noted that the model used here is a double layered structure (i.e. graphene64 and graphene256) and the number of atoms are unknown for calculated results. Another thing about the bulk modulus, when the c-axis is increased to 15 Å, the bulk modulus decreases. The derivative of bulk modulus for graphene64 and graphene256 are the same which is equal to 1. Reich *et al*. [133] calculated the derivative of bulk modulus where they got 1, which is the same with graphene64 and graphene256. Girifalco *et al*. [137] calculated the bulk modulus of graphite with different number of atoms and all the values were different. Then it can be said that, the surface area of a material affects the bulk modulus but it does not affect its derivatives. The interplanar spacing of 15 Å could also play a crucial role. But some of the equilibrium properties of graphene64 and graphene256 are similar.

Table 4. 3: Calculated and measured lattice constant (a), bulk modulus (B_0), its derivative (B'), cohesive energy ($CohE_0$), and minimum volume (V_0)

	Graphene64 this work	Graphene256 this work	Calculated [88,125,126,128]	Experimental [7,20]
a(Å)	2.70	2.72	2.47	2.46
$CohE_0$(eV/atom)	-7.28	-7.30	-7.36	-7.60
B_0(GPa)	672	422	700	
B’	1.00	1.00	1.00	
V_0(Å^3/atom)	7.46	5.45	6.08	

4.2.2 Thermodynamics properties of a bilayer graphene (BLG)

Up to this point, ordinary temperature (300 K) properties of double layered models have been considered. The thermodynamics properties of the systems were also considered. Quantum mechanical effects are very important in understanding the thermodynamics properties below the Debye temperature. Since the molecular dynamics method treats the motion of the atoms classically, we only consider the thermodynamics properties above the Debye temperature, where the quantum effect can be neglected [138]. The graphite Debye temperature of 2500 K along the a-axis has been considered [139]. After optimization calculations, the isothermal–isobaric ensemble (NPT) was used to perform the simulation. In order to investigate the thermal expansion coefficient some strain has been exerted along the sheet plane on the models.

4.2.2.1 Specific heat capacity of bilayer graphene64 and graphene256

The specific heat capacity of a material represents the change in energy density E when the temperature changes by 1 K,

$$C_v = \frac{d\,E}{dT}\,. \qquad (4.2).$$

The specific heat and heat capacity are sometimes used interchangeably, with units of joules per kelvin mass, per unit volume, or per mole. The unit, joule per kelvin (J/K) was converted to electron volts per kelvin (eV/K). The specific heat does not determine the thermal energy stored within a body only but also how quickly the body cools off or heats up [133].

Data in figure 4.9 was used to calculate the specific heat capacity of graphene64 and graphene256. The specific heat capacity calculated for both systems is 3.42 k_B. This differs by 12% from the Dulong –Petit's law (3 k_B) of solids at high temperatures, although no experimental data on this has been considered. Zakharchenko et al. [141] found out that the specific heat capacity of a single layer of graphene (SLG) and a bilayer of graphene (BLG) are similar and he also showed that the specific heat capacity at a high and low temperature are not the same. The specific heat of graphene has not been measured directly [140].

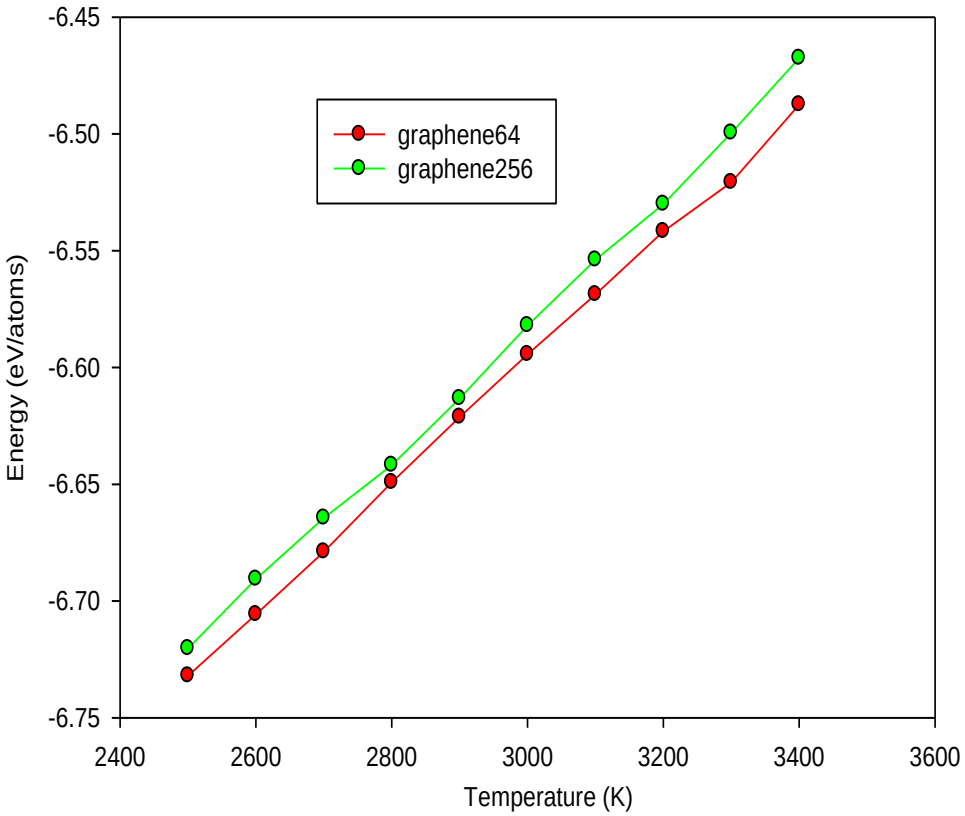

Figure 4. 9: Energy as a function of temperature for graphene64 and graphene256.

4.2.2.2 Coefficient of thermal expansion (CTE) of bilayer graphene64 and graphene256

The coefficients of thermal expansion (CTE) together with the specific heat capacity are both of practical and theoretical importance. They are essential for predicting the thermodynamic equation of state of materials. The coefficient of thermal expansion is one of the most important nonlinear thermal properties. It is obtained from the temperature derivative of lattice constant or temperature derivative of volume,

This is given by:

$$\beta = \frac{1}{V}\left(\frac{\partial V}{\partial T}\right)_P. \qquad (4.3)$$

In the present case the volume was used as function of temperature. The volumetric coefficient of thermal expansion of graphene64 and graphene256 were calculated using figure 4.10. At a low temperature, the coefficient of thermal expansion of graphene is expected to be negative and positive at high temperature [141-142]. Most of the researchers who calculated coefficient of thermal expansion at a low temperature used experimental method and those who calculated thermal expansion coefficient at high temperature used the modelling method. Since our calculation was made at high temperature, we expect our thermal expansion to be positive. The thermal expansion coefficient of graphene64 is 5.02 $x10^{-6}$ K^{-1} and for graphene256 is 9.76 $x10^{-6}$ K^{-1}. Both models have different coefficient of thermal expansion but both of them are positive. Bao et al. [142] calculated the coefficient of thermal expansion of graphene at a low temperature between 0 K and 400 K using experimental method and found -7$x10^{-6}$ K^{-1}. Jiang et al [143] calculated the coefficient of thermal expansion of graphene at a low temperature using nonequilibrium Green's function method; he got -6$x10^{-6}$ K^{-1}. Zakharchenko et al. [141] calculated the negative coefficient of thermal expansion of single layer graphene and found the negative-positive transition to occur at ~900 K. The positive values ranges from 4-20 $x10^{-6}$ K^{-1} at high temperatures. Yoon et al. [144] calculated the coefficient of thermal expansion of single-layer graphene using Raman spectroscopy at a temperature range 200-400 K, it was found to be negative and the value is -8.0$x10^{-6}$ K^{-1}. The results are summarised in table 4.4.

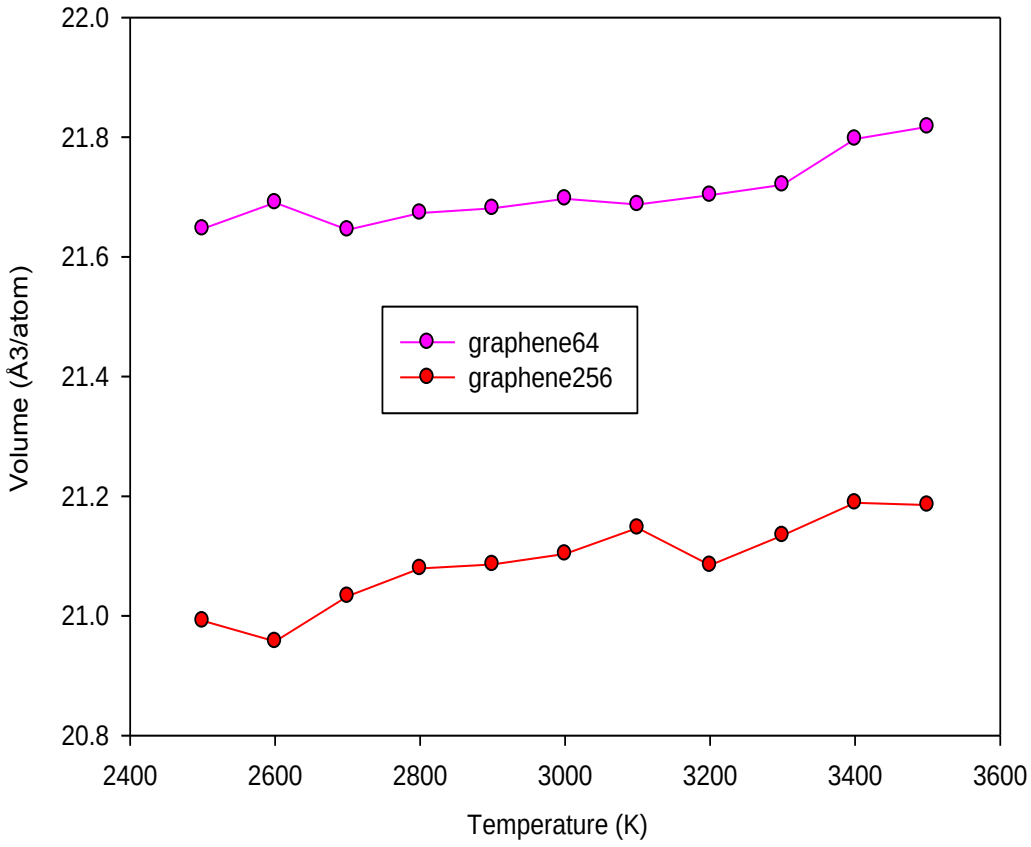

Figure 4. 10 : Volume as a function of temperature for graphene64 and graphene256.

Table 4. 4: The specific heat capacity (C_v) and coefficient of thermal expansion (β) of bilayer graphene

	C_v (K^{-1})		β (k_B)
Graphene64	5.02 $x10^{-6}$		3.42
Graphene256	9.76 $x10^{-6}$ K^{-1}		3.42
Experimental results[142,144]	Low temperature	High temperature	
	-7$x10^{-6}$		
Calculated [141,143]	-6$x10^{-6}$	4-20$x10^{-6}$	3.00

4.3 Conclusion

Some of the results are in agreement with the theoretical calculations and experimental data. This agreement shows the ability of Tersoff potential in combination with the molecular dynamics method, to predict the physical properties of various forms of graphene. The bulk modulus of graphene256 is totally disagreeing with other calculations but graphene64 agrees with the calculated one. When the c-axis increases, the volume of the configuration increases also which triggers a decrease in the bulk modulus. So the size of the surface area affects the bulk modulus. The derivative of bulk modulus for graphene64 and graphene256 are the same with the calculated one. The specific heat capacity of graphene64 and graphene256 is the same. The coefficient of thermal expansion of both models are positive at high temperatures but different. Graphene256 is more stable than graphene64 because the minimum energy and minimum volume of graphene256 is less than the one for graphene64.

Chapter 5

Molecular dynamics simulation of structural and thermodynamic properties of single-walled carbon nanotube

5.1 Introduction

Carbon nanotubes were discovered in 1985 [145]. Fullerenes played an important role in the discovery of carbon nanotubes. C_{60} was the first molecule to be discovered. Its structure was comparable to that of graphite which was already existing, but C_{60} was a new structure because it had excellent properties than graphite. With the help of arc evaporation setups in the laboratory, it was suggested in 1990 that C_{60} can be composed easily. In 1991 [146] well-known Japanese researcher Sumio Iijima identified the fullerene which was associated with carbon nanotubes. Their tubes were double layered with a diameter of about 300 Å and they were closed from both ends. This was a dominant discovery which was well supported in electronics, mechanics and chemistry fields. Recently researchers discovered that carbon nanotubes have thermal conductivity which is better than that of diamond, with a better mechanical strength than that of steel and good electrical conductivity than copper.

Carbon nanotubes (CNTs) have engaged a lot of attention, because of their amazing structural, mechanical and electronic properties, those properties cause carbon nanotube to be attractive for different functions in our daily life [147]. A carbon nanotube is a tube-shaped material, made of carbon, having a diameter measuring in the nanometre scale. The graphite layer appears a little bit like a rolled-up chicken wire with an endless unbroken hexagonal mesh and carbon molecules at the apexes of the hexagons. Carbon nanotubes have different structures, which differ with length, thickness and in the type of helicity and number of layers. Basically, as sheets of graphite layers rolled up to make a tube, carbon nanotube construction is demonstrated using chiral vectors in figure 1.1 of the basic introduction (chapter 1). This two dimensional cylinder of a given radius with different helicities is described by rolling vectors (*n,m*). Therefore (*n,0*), (*n,n*), and (*n,m*) explain the respective zigzag, armchair, and chiral nanotubes. Even though they are produced from actual the same graphite sheet, their electrical properties are different depending on their variations,

acting either as metals or as semiconductors. As a group, carbon nanotubes typically have diameters ranging from 10 Å up to 500 Å [68]. Their lengths are usually several microns, but current improvements have made the nanotubes much longer and they can be measured in centimetres. In this chapter the results of the structural and thermodynamics properties of single-walled carbon nanotubes are presented [148].

5.2 Results and Discussion [148]

Single-walled carbon nanotubes modelled in this work are an armchair (12,12) carbon nanotube, two chiral structures (12,10), and (10,12) nanotubes, which are referred to as cnt(12,12), cnt(12,10), and cnt(10,12) respectively. The structures were chosen such that all have comparable number of carbon atoms; i.e cnt(12,12) has 312 carbon atoms, whilst cnt(12,10) and cnt(10,12) both have 264 and 260 carbon atoms respectively. Furthermore, cnt(12,12) and cnt(12,10) have equal values of *a* and *b*-axis, likewise, cnt(12,12) and cnt(10,12) *c*-axis values are equal. Loosely articulating, cnt(12,10) can be thought of as the projection of cnt(12,12) along the *a* and *b*-axis whereas cnt(10,12) can be thought of as the projection of cnt(12,12) along the c-axis. It needs to be mentioned that all the literature studied works only with chiral structures of the (2*n*,*n*) form [149-151]. The radial distribution functions $(F(r))$ and structure factors ($S(k)$) were calculated at 300, 3000, and 5000 K temperature, to observe the behaviour of atomic configurations and interatomic interactions at elevated temperatures. In order to obtain the equilibrium configurations of these models *a*-axis values were varied with total energy at constant temperature of 300 K until a convincing minimum energy is found. Based on the optimized structures and their energies, various equilibrium properties of these models had been extracted.

5.2.1 Structural properties

The very same procedure for structural optimization under the NVT ensemble from the previous chapter about the bilayer of graphene has been followed. The c-axis for an armchair (12, 12) was found to be 27.105 Å and that of chiral (12, 10) to be 22.935 Å. Figure 5.1 and 5.2 are the structures of single-walled carbon nanotubes for chiral (12,10) at 300 K and 5000 K temperature respectively. At 5000 K, the structure suggests that atom C_{248} is not attached to any atom in the structure. Figure 5.3 and 5.4 are the structural configuration of single-walled carbon nanotubes for armchair

(12,12) at 300 K and 5000 K respectively. For armchair at 5000 K, all atoms are still attached to the structure. To quantify upon this; the armchair configuration appears to be more mechanically stable than the chiral configuration.

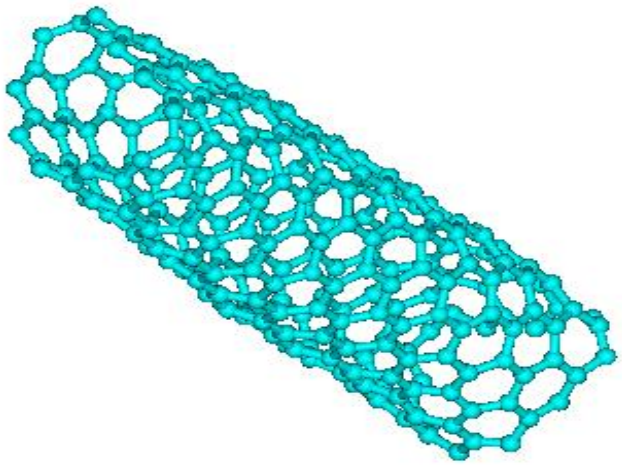

Figure 5. 1: A typical chiral cnt(12,10) carbon nanotube structure at 300 K.

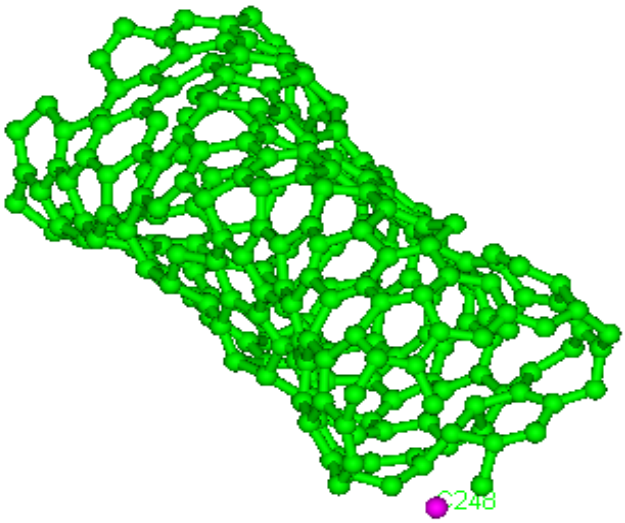

Figure 5. 2: A typical chiral cnt(12,10) carbon nanotube structure at 5000 K.

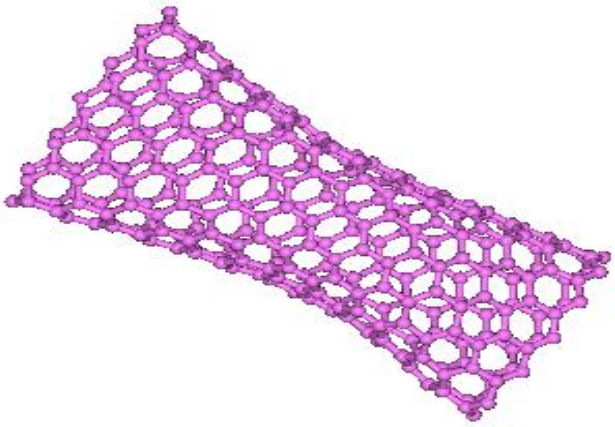

Figure 5. 3 : A typical armchair cnt(12,12) carbon nanotube structure at 300 K.

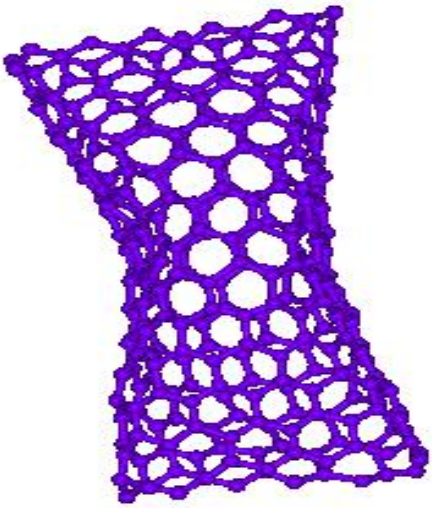

Figure 5. 4: A typical armchair cnt(12,12) carbon nanotube structure at 5000 K.

5.2.1.1The radial distribution function (rdf) of single-walled carbon nanotubes (SWCNT)

In order to draw confidence on the empirical bond order potential, radial distribution functions ($F(r)$) for sinlge-walled carbon nanotubes in two chiral forms have been calculated. When searching for the minimum of the three symmetry configurations; chiral cnt(10,12) configuration produced a maximum instead of a minimum, so it was discontinued in the study. Even though our $F(r)$ gives information only up to the second nearest neighbour, the insight upon the arrangement of carbon atoms in nanotubes can be extracted. This can be quantitatively compared with carbon atoms distribution in graphene and graphite configurations. Using the peak positions of $F(r)$, the nearest neighbour and the second nearest neighbour carbon atoms in single-walled carbon nanotubes can be determined. The peak positions appear at 1.45 and 2.50 Å for both armchair cnt(12,12) and chiral cnt(12,10) at 300 and 3000K, and at 5000 K the peaks appear at 1.47 and 2.54 Å for both models, which are in good agreement with other theoretical calculations and experiments [152-154]. The radial distribution function for cnt(12,10) and cnt(12,12) at 300, 3000, and 5000 K are shown in figures 5.5 and 5.7 respectively. Detailed information from the $F(r)$ can be harvested in table 5.1 and 5.2 respectively. Figures 5.6 and 5.8 display the structure factor functions $S(k)$ for cnt(12,10) and cnt(12,12) respectively at 300, 3000, and 5000 K. The $S(k)$ is the Fourier transform of $F(r)$ from the real space to the reciprocal space. The $S(k)$ plot of 5000 K has least oscillation and $S(k)$ plot at 300 K has more oscillation implying that more information about C-C interaction can be extracted at 300 K.

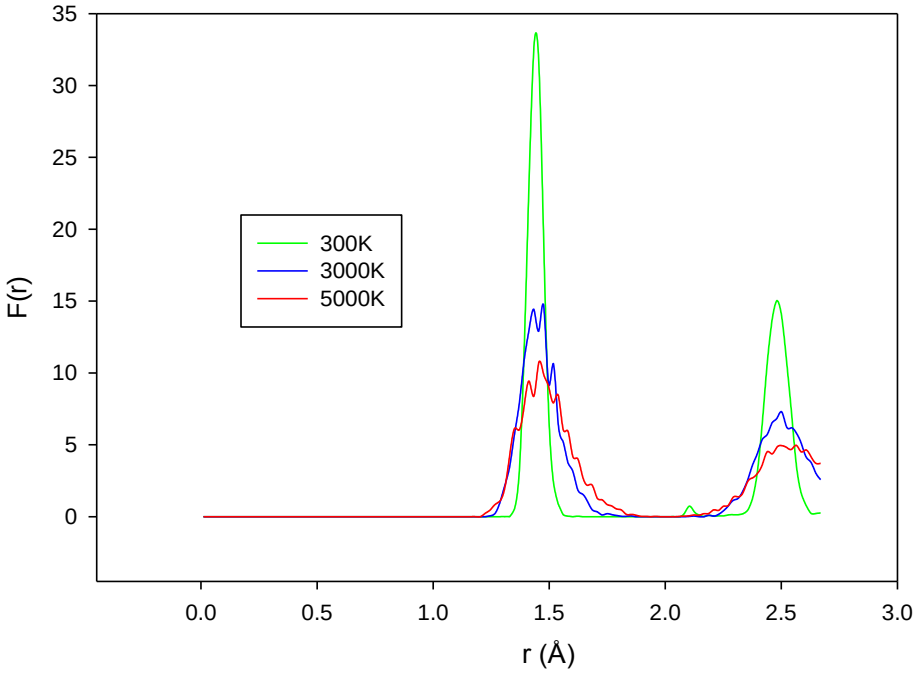

Figure 5. 5: Radial distribution function of chiral cnt(12,10) carbon nanotube bundles.

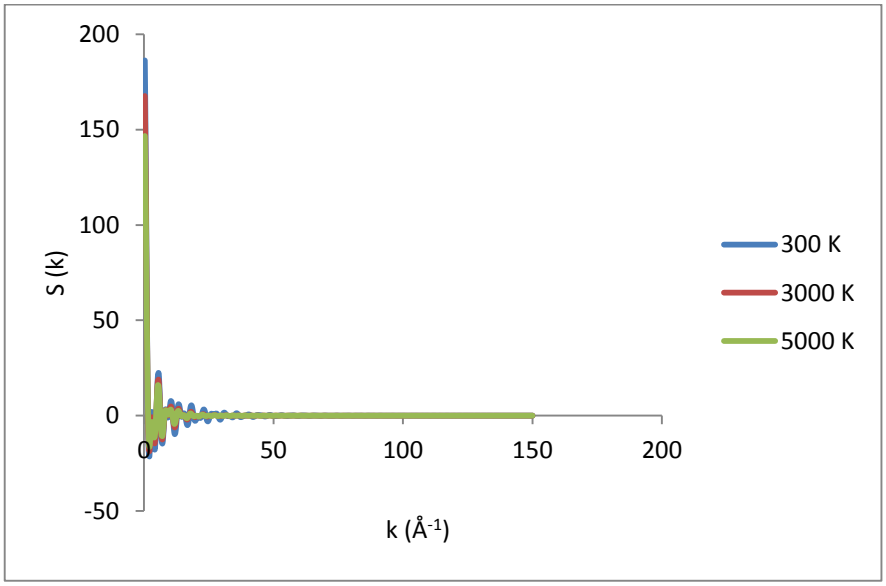

Figure 5. 6: Structure factor for the chiral cnt(12,10) carbon nanotube bundles

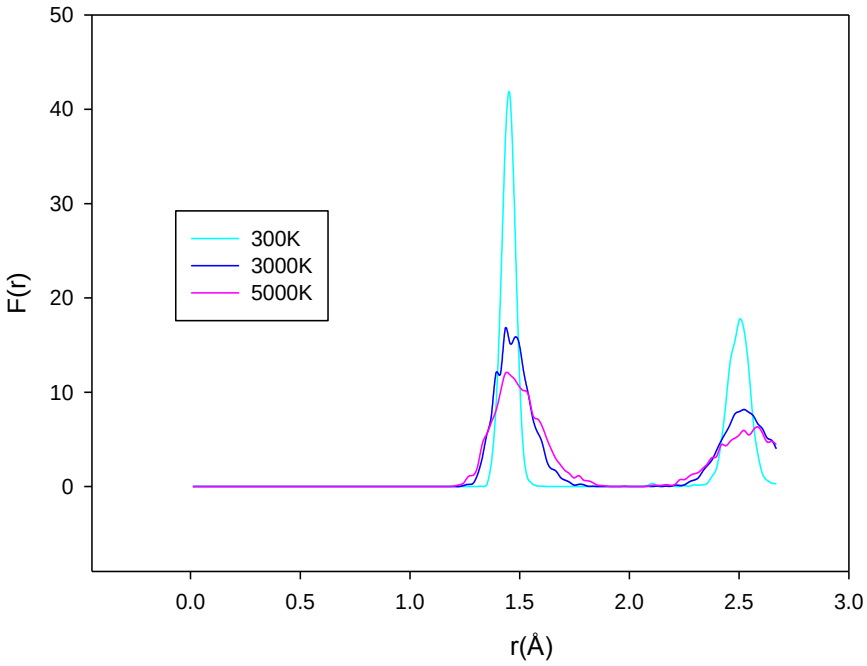

Figure 5. 7: Radial distribution function of armchair cnt(12,12) carbon nanotube bundles.

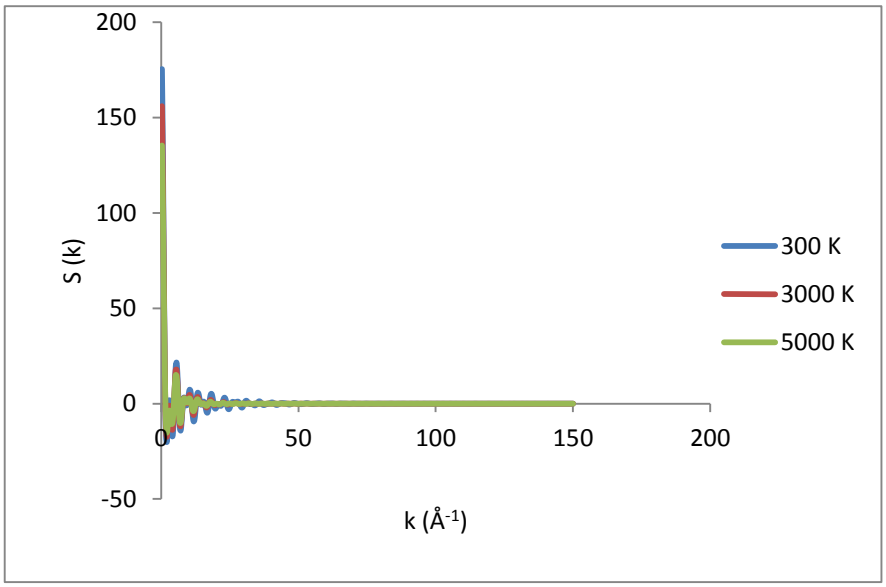

Figure 5. 8: Structure factor for the armchair cnt(12,12) carbon nanotube bundles.

Using a pictorial scrutiny of the $F(r)$ in figures 5.5 and 5.7 and comparison of experimental results in table 5.1, it appears that the carbon nanotubes tubular structure is robust with cylindrically stable structure even at extremes of temperature. This toughness is comparable to that of diamond according to table 5.1 standards. Atomic distribution around the first nearest neighbour is uniform in all temperature ranges and it resembles that of diamond according to Kakinoki *et al*. [154] even though the peak positions are for graphite. At second nearest neighbour distance (2.50 Å) coordination is diamond-like at 300 K but becomes more graphitic at 5000 K. Wiggles observed at 3000 and 5000 K peaks on cnt(12,12) suggest that armchair is not as robust as chiral cnt(12,10). The number of atoms around the first nearest neighbour parameter is represented by n_1 and the number of atoms around the second nearest neighbour parameter is represented by n_2. When the temperature is increased, the height of the peaks decreases. For n_1 and n_2 for both, they decrease with the increasing temperature.

Table 5. 1: Radial distribution function (F(r)) quantities at 300, 3000, and 5000 K in comparison with graphite and diamond data [152-154].

	Temperature (K)	r_1 (Å)	r_2 (Å)	n_1	n_2
cnt(12,12)	300	1.45	2.50	3.63	2.07
	3000	1.45	2.50	3.04	1.55
	5000	1.47	2.54	2.85	1.33
cnt(12,10)	300	1.45	2.50	3.08	1.75
	3000	1.44	2.50	2.61	1.49
	5000	1.47	2.54	2.43	0.77
Graphite [153]	300	1.43	2.53	3.30	-
Diamond [154]	300	1.55	2.53	3.45	-

5.2.1.2 Equilibrium properties of single-walled carbon nanotubes

Various experiments and calculations have shown that the average diameter of single-walled carbon nanotubes (SWCNT) is in the range of 12-14 Å. The distance separating consonant carbon atoms in periodic hexagonal lattice is 2.46 Å, with parallel c-c bonding separation of 2.45 Å. The c-c bond length is 1.42 Å with a tight bonding overlap energy of about ~2.5 eV. According to Thess *et al*. [153] bundles of carbon nanotubes with metallic behaviour have lattice constant in the region of ±17 Å. These laser-ablated bundles occur in two dimensional triangular lattice uniform tubes having C_{5v} symmetry.

The equilibrium properties calculated from figures 5.9 and 5.10 are shown in table 5.2 for cnt(12,12) and cnt(12,10) together with results from other calculations and experiments from the literature [156-165]. Lattice constant of chiral (12,10) SWCNT bundles differs from the calculated one by 0.4% and from the experimental one by 0.7%. These properties were extracted from figure 5.9 and 5.10 for cnt(12,10) and cnt(12,12) respectively. Lattice constant of armchair (12,12) differs from the calculated one by 2% and from the experimental one by 1%. The cohesive energy of chiral (12,10) SWCNT differs from the calculated one by 0.7% and from the experimental one by 3%. Cohesive energy of armchair (12,12) SWCNT differs from the calculated one by 1% and the experimental one by 4%. The diameter of carbon nanotubes depends on whether the carbon nanotube is a zig-zag, armchair or chiral. And the chiral angles again have an effect on the diameter of single-walled carbon nanotubes.

Imtani and Jindal [159] calculated the diameter of a single-walled carbon nanotubes using chiral carbon nanotubes with different values of integers n and m; the value of those diameters ranged from 14.4 – 14.8 Å. In our case for chiral single-walled carbon nanotubes, the diameter was found to be 14.9 Å which agrees with the calculated one [158]. The armchair structure had the diameter of 16.3 Å which agrees with the experimental results of 8.0-16.0 Å [165]. Although the bulk modulus for the single-walled carbon nanotubes bundle, is not the same with the calculated individual single-walled carbon nanotube and the experimental single-walled carbon nanotubes.

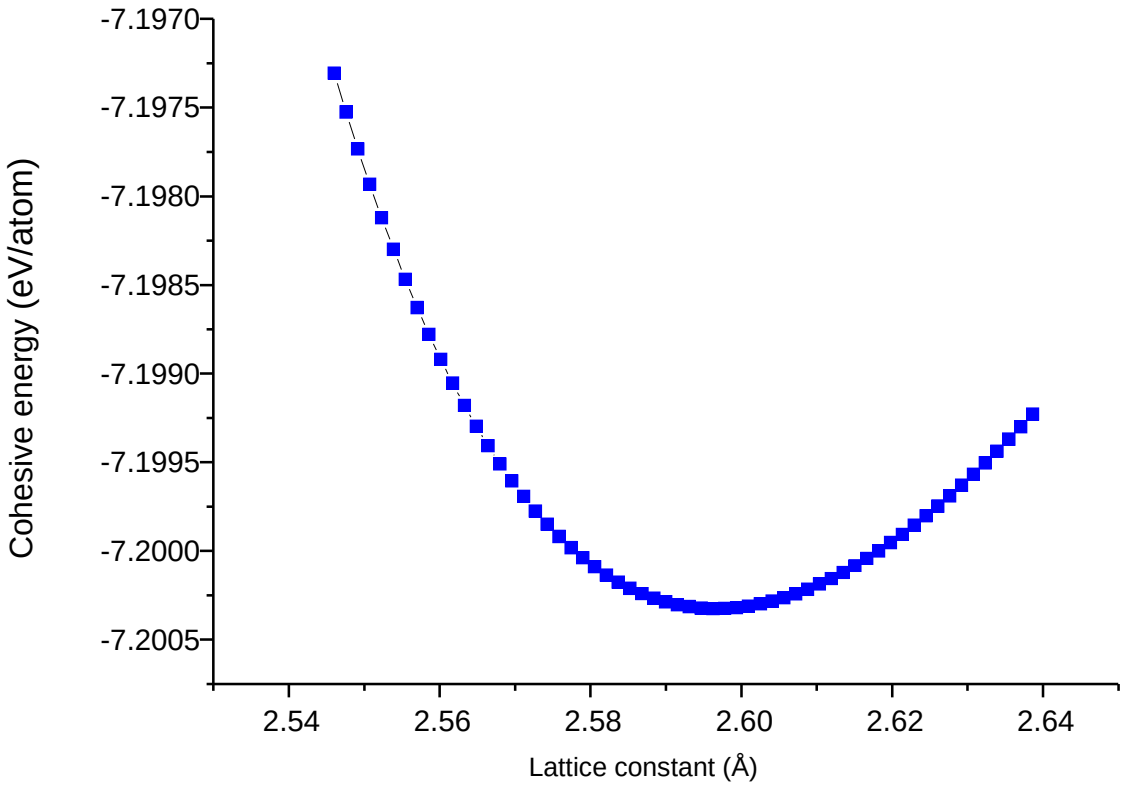

Figure 5. 9: Cohesive energy as a function of lattice constants for chiral cnt(12,10) carbon nanotube bundles.

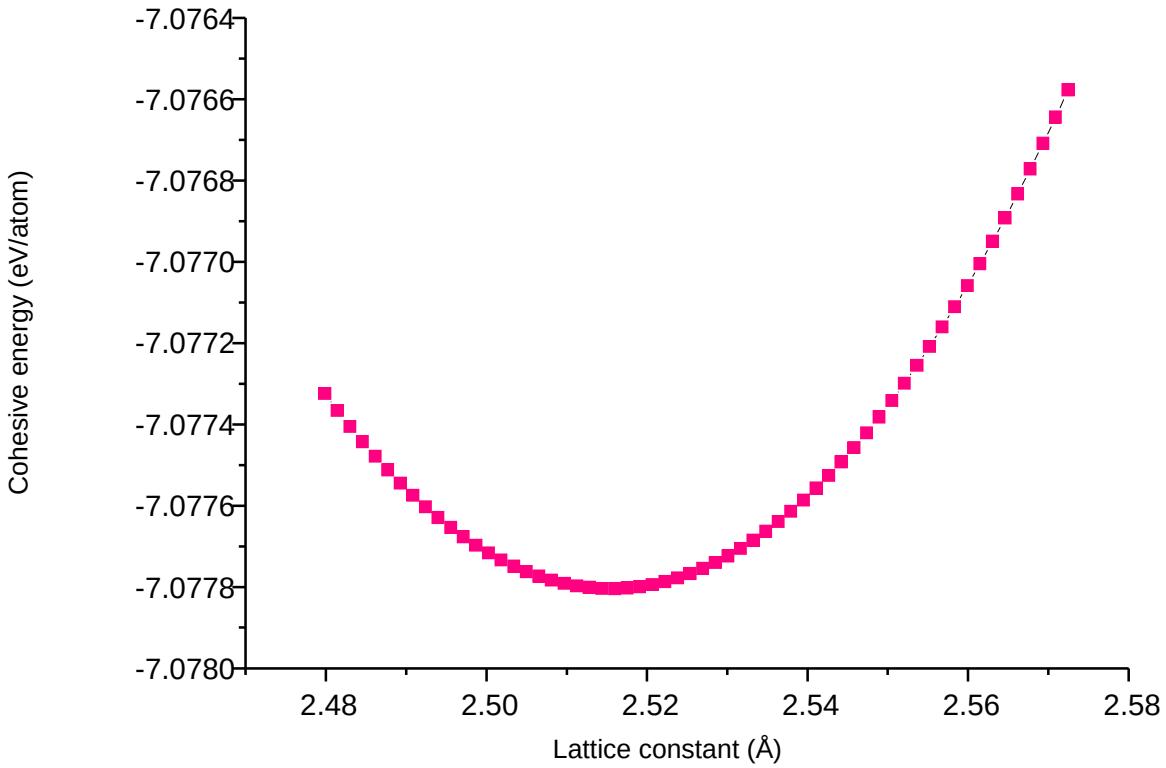

Figure 5. 10: Cohesive energy as a function of lattice constants for armchair cnt(12,12) carbon nanotube bundles.

Table 5. 2: Calculated and measured lattice constant (a), bulk modulus (B_0), its derivative (B'), minimum energy (E_0), diameter (D_{cnt}) and minimum volume (V_0)

	cnt10x12(this work)	cnt12x12(this work)	Other[139,140,141, 143]		Exp[139,143, 123,145, 149]
a_o (Å)	2.60	2.52	2.49		2.46
D_{cnt} (Å)	14.9	16.3	14.4-14.8		8.00-16.0
E_o (eV)	-7.20	-6.30	-6.65		-7.29
B_0 (Gpa)	44.6	21.1	bundle	individual	462-546
			37	230	
B'_o	1.00	1.00	4.50		
Vo (Å^3/atom)	29.4	27.2	34.9		

Unlike in other equilibrium properties, the bulk modulus can be affected by the surface area, whether the model is multi-walled or single-walled, and again if it is an individual or bundle of nanotubes. The derivatives of both single-walled models are the same which is equal to 1, but differ from the calculated one [158]. Povob *et. al.* [160] calculated the bulk modulus of a single-walled carbon nanotubes using Raman calculation and the value was found to be 462 to 546 GPa which shows the disagreement with our results. Reich et al. [133] calculated the bulk modulus of carbon nanotubes for individual and bundle carbon nanotubes; the two values were not similar. Girifalco et al. [137] calculated the bulk modulus of carbon nanotube at a different number of atoms and all the values were different.

5.2.2 Thermodynamic properties of single-walled carbon nanotube

The same optimization procedure and thermodynamic equations that were used in bilayer graphene (section 4.2.2) applies. Experiments by Nan *et. al* [195] show that carbon nanotubes are stable at the temperature range 300 – 875 K. In this temperature range the molar heat capacity of single-walled carbon nanotubes is smaller than that

of multi-walled carbon nanotubes. In addition, the TEM photography shows dispersed tubes of 200 – 400 Å in diameter [195].

5.2.2.1 Specific heat capacity of single-walled carbon nanotubes

The data in figure 5.11 was used to calculate the specific heat capacity of the chiral cnt(12,10) and armchair cnt(12,12) nanotube bundles respectively. The specific heat capacity calculated for both systems is 3.42 k_B. This differs by 12% from the Dulong – Petit's law (3 k_B) of solids at high temperatures, although no experimental data on this has been considered at high temperatures.

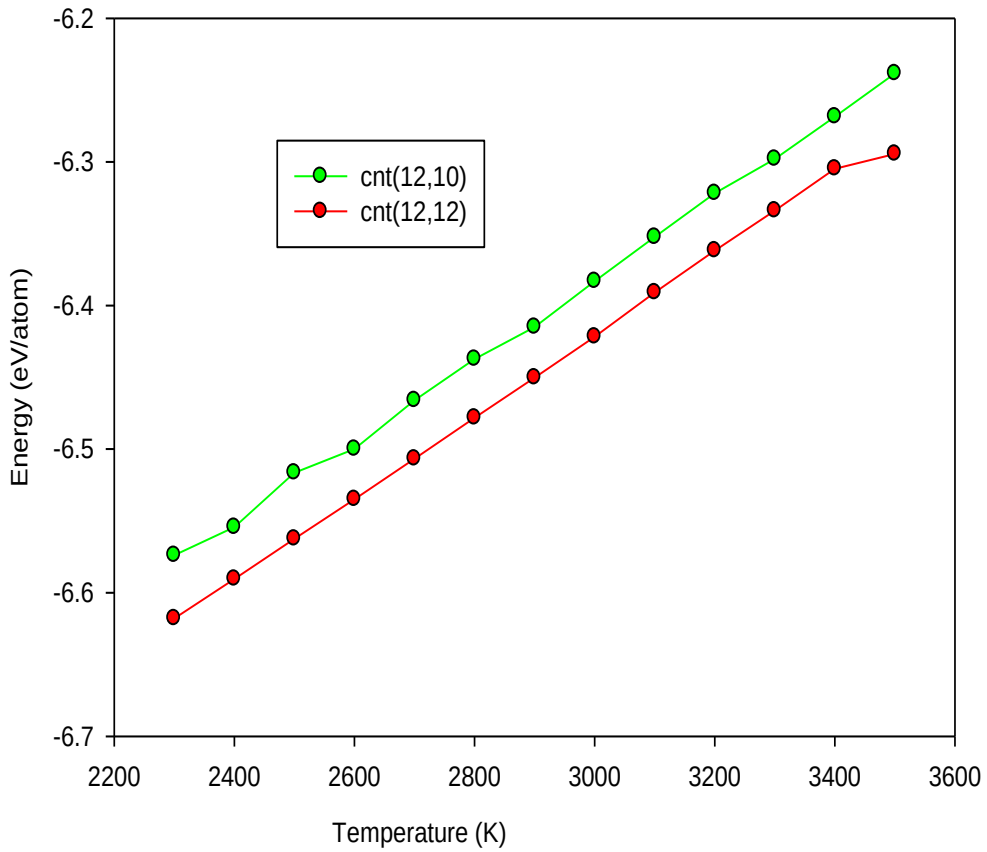

Figure 5. 11: Energy as a function of temperature for chiral cnt(12,10) and armchair cnt(12,12)

5.2.2.2 Coefficient of thermal expansion (CTE) of a single-walled carbon nanotubes

In this case, the volume as a function of temperature relation was used (figure 5.12) to calculate the volumetric thermal expansion of single-walled carbon nanotubes.

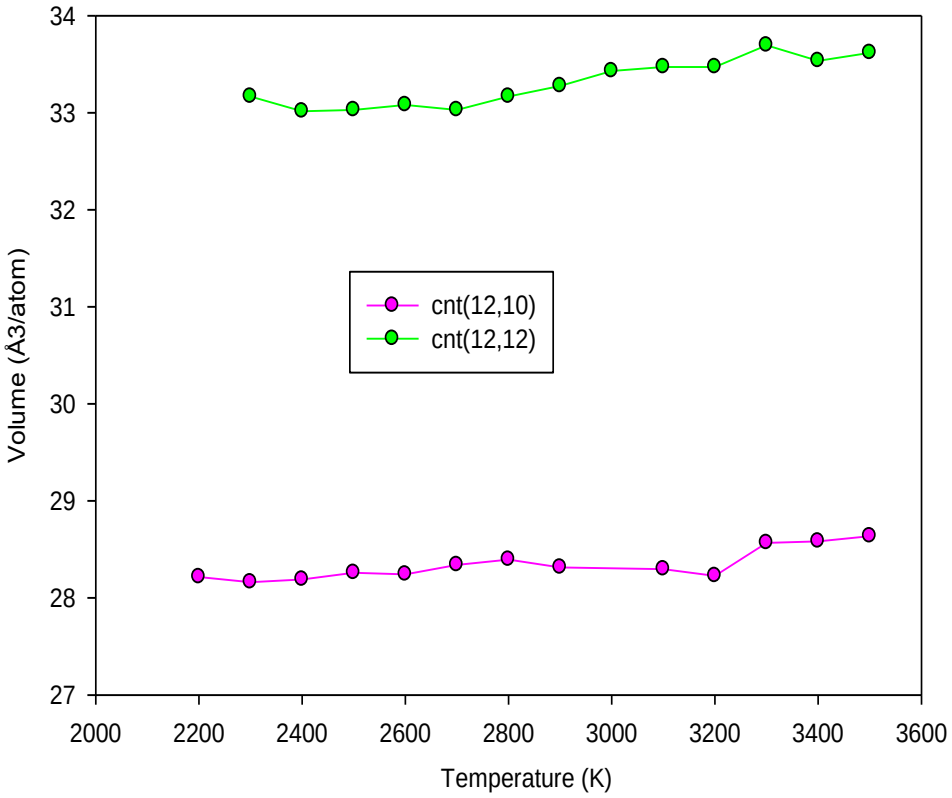

Figure 5. 12: Volume as a function of temperature for chiral cnt(12,10) and armchair cnt(12,12)

The volumetric thermal expansion coefficients of the armchair cnt(12,12) and chiral cnt(12,10) symmetries were then calculated and are shown in table 5.3. The thermal expansion coefficient of armchair cnt(12,12) is 18.9 $x10^{-6}$ K^{-1} and that of chiral cnt(12,10) is 10.9 x 10^{-6} K^{-1}. Both models have different thermal expansion coefficient but both of them are positive, the model with high number of atoms has the high value of thermal expansion coefficient and the one with less number of atoms has the smallest value. Jiang *et al*. [163] calculated the coefficient of thermal expansion of carbon nanotube at a low temperature using non-equilibrium Green's function method; he got -9.6$x10^{-6}$ K^{-1}. Naveen [167] calculated the thermal coefficient of expansion of carbon nanotubes using molecular dynamics at a low temperature and got -8.88 $x10^{-6}$ K^{-1} and at a high temperature got 16.16 $x10^{-6}$ K^{-1}.

Table 5.3: The specific heat capacity (C_v) and coefficient of thermal expansion (β) of single-walled carbon nanotube for cnt(12,10) and cnt(12,12)

	C_v (K^{-1})		β (k_B)
cnt(12,10)	10.9 $x10^{-6}$		3.42
cnt(12,12)	18.9 $x10^{-6}$		3.42
	Low temperature	High temperature	
Experimental results [147]	-1.50x 10^{-6}	-	
Calculated results [163,167]	-8.88 $x10^{-6}$ -9.60$x10^{-6}$	16.2 $x10^{-6}$	3.00

5.3 Conclusion

The armchair configuration appears to be more mechanically stable than the chiral configuration. The results are in agreement with the theoretical calculations and experimental data. This agreement shows the ability of Tersoff potential in combination with the molecular dynamics method, to predict the physical properties of various forms of carbon nanotubes. The bulk modulus of both models can be related to the one for the single-walled carbon nanotube bundles but differs with the calculated individual single-walled carbon nanotubes and the experimental one. The derivatives of both models are the same but differ with the calculated one. The specific heat capacity of single-walled armchair cnt(12,12) and chiral cnt(12,10) is the same. The coefficient of thermal expansion of both model are positive at a high temperature. The surface area does not affect the specific heat. The value of temperature and the surface area affect the coefficient of thermal expansion.

Chapter 6

XRD and AFM studies of graphene and single-walled carbon nanotube

6.1 Introduction

Single walled carbon nanotubes are of good interest from the aspect of their exclusive electronic properties, chemical stability and important application in molecular electronic device as well as for probe tip in scanning probe microscopy (SPM) [186]. Carbon nanotubes (CNTs) based devices have been manufactured by selecting single tubes from any deposited CNTs consisting of many bundles [196]. On the other hand graphene appears to be an interesting material with promising functions. It has extraordinary characteristics because it is a Dirac solid, with the electron energy being linearly reliant on the wave vector close to the crossing points in the Brillouin zone [197]. In this chapter, the experimental results of graphene and single walled carbon nanotubes will be presented using the atomic force microscopy (AFM) and X-ray powder diffraction (XRD) techniques.

6.2 Characterisation Techniques

6.2.1 Atomic force microscopy (AFM)

AFM is usually used to characterise inorganic, organic, and biological nanostructures. The factor resolution achieved by AFM is determined in large part by the size and shape of the imaging probe tip [168]. This technique is mostly used for assessing the dispersion and separation methods of nanotubes and it is also used to assess the condition of the samples [169]. Besides that it can determine the diameter of the tube and is actually useful in determining if the nanotubes are in the form of bundles or individuals, as well as if they are multi-walled or single-walled [170]. Atomic force microscopy (AFM) has become a great technique in the field of nanotechnology due to its exclusive strength to characterise structures in liquid, ambient, and vacuum environments [171].

The probe tip is a critical and probably limiting component of the global technology in AFM and other scanning probe microscopies. Ordinary micro-fabricated pyramidal silicon tips and oxide-sharpened silicon nitride tips usually have radii of curvature that

range from 50 to 150 Å, with a half cone angles of 10-35° [171]. It does not only give different aspects in nanoscale structures, but it can again be used as a manipulator of those structures. AFM is a great microscopy apparatus because it is very cheap and supply a high resolution (at the atomic scale in some cases) and it is very flexible [173]. After all, a dominant disadvantage to AFM is the length of time it takes to achieve a high quality image. A scan of a sample that is 0.8 millimetres ($8x10^6$ Å) wide can take as long as 10 minutes, but a scan from an electron microscope takes just few seconds. Speedy scanning techniques have been recently in the market, so that they can be used to solve this disadvantage [174].

Three AFM modes which are available are contact (static) mode, intermittent contact (semi contact or tapping) mode and non-contact mode. The latter two modes are also called dynamic or oscillatory [175]. In contact mode, the tip apex is exactly in contact with the surface and the force acting between the atoms of tip. Besides that the sample is counteracted by the elastic force formed by the deflected cantilever according to Hooke's law:

$$F = -kz. \quad (6.1)$$

Where F is the elastic force, k is the proportionality constant and z is size of displacement.

The contact mode may be performed either at consistent force or consistent height. A new cycle in imaging was presented when microscopists introduced a system for carrying out the non-contact mode which is used in situations where tip contact might change the sample in exquisite actions [176]. In this mode the tip drift around 50-150 Å above the sample surface. Interesting van der Waals forces acting between the tip and the sample are discovered and topographic images are created by scanning the tip above the surface [177].

Tapping mode is a key advance in AFM. This important technique allows high resolution topographic imaging of sample surfaces that are quickly damaged, generally hold to their substrate or crucial to depict by other AFM techniques [178]. This mode overcomes issues related with friction, adhesion, electrostatic forces and other complications that affect ordinary AFM scanning methods by alternately putting the tip in contact with the surface to supply high resolution and again to lift the tip off the surface to dodge dragging the tip across the surface [179]. Tapping mode imaging

is carried out in the atmosphere by oscillating the cantilever assembly at or near the cantilever's resonant frequency using a piezoelectric crystal [178].

Different types of solvents that can be used when characterising carbon nanotubes using AFM are chloroform, toluene, tetrahydrofuram, dimethylfermamide (DMF), ethanol and more. SiO_2 substrate is mostly used when doing the measurement. In this chapter single-walled carbon nanotubes were characterised using Easy Scan 2Flex AFM. Figure 6.1 shows one example of an atomic force microscope.

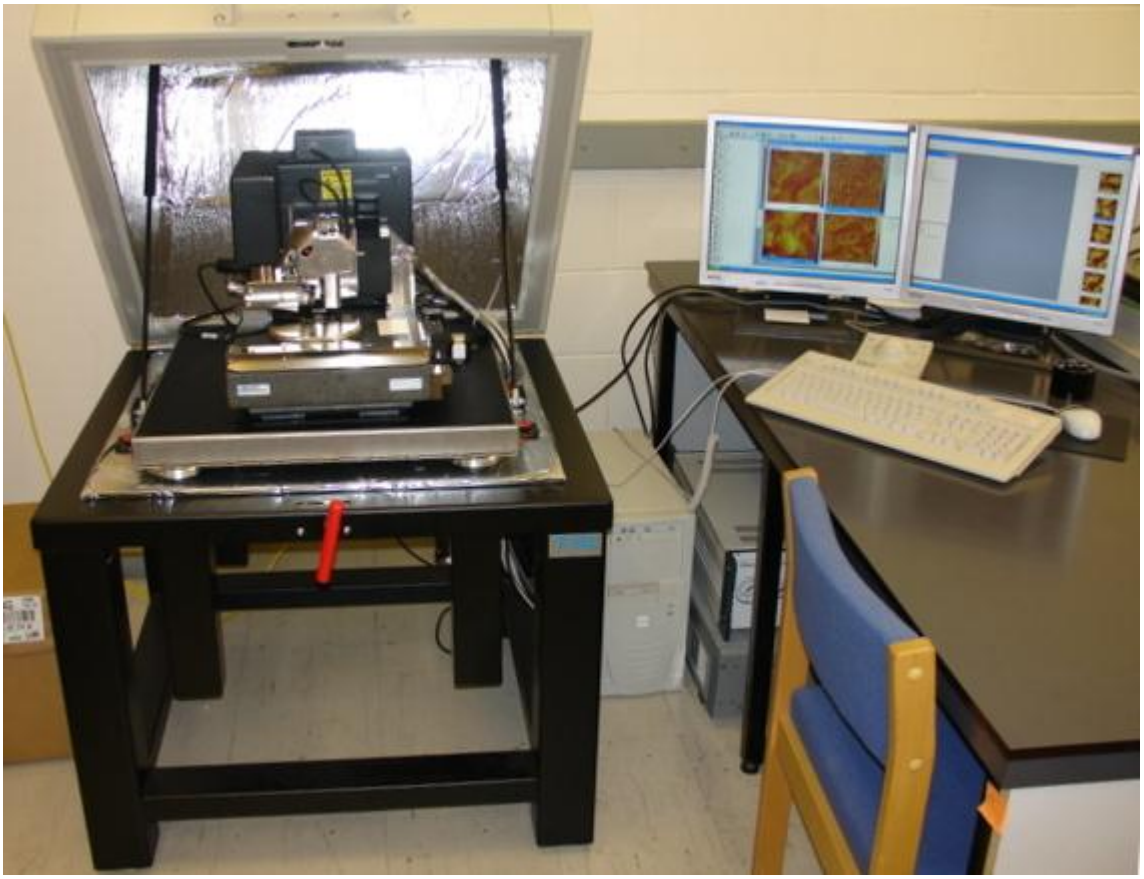

Figure 6. 1: Atomic force microscopy (http://en.wikipedia.org/wiki/Atomic_force_microscopy)

6.2.2 AFM Preparation

The single-walled carbon nanotubes that were used in this work were bought from Sigma Aldrich. When preparing SWCNT for characterization, 3 mg of SWCNT was added in 10 ml of chloroform. On washing Si substrate, acetone was put in beaker with Si substrate and then ultra-sonicated for 10-15 minutes, followed by washing with distilled water. Isopropanol was added in the beaker together with Si substrate and ultra-sonicate it for 10-15 minutes. Si substrate was then dried using nitrogen gas. The sample of SWCNT was ultra-sonicated for 30 minutes. Then one drop of the solution was added on the Si substrate and left to dry. The same method was followed using ethanol solvent.

6.2.3 X-Ray Powder Diffraction (XRPD)

X-ray powder diffraction is one of the potential techniques used by mineralogists to investigate the mineralogy of finer grained sediments, particularly clays [180]. It is also used by solid state chemists and physicists to investigate the physical and chemical make-up of unknown solids [181]. As a method, X-ray diffraction is interesting because of its fast and satisfaction performance and again because it need only a small portion of sample. This technique is non-destructive and can be used to carry out semi-quantitative analyses of poly-mineralic mixtures [182]. The elemental geometry of an X-ray diffractometer includes a source of monochromatic radiation and an X-ray detector placed on the circumference of an accredited circle centred on the powder specimen. Divergent slits which are placed between the X-ray source and the specimen, and divergent slits which are placed between the specimen and the detector, restrict scattered (non-diffracted) radiation, lower background noise and compile the radiation [183]. The detector and specimen holder are mechanically connected with a goniometer so that a rotation of the detector through 2ɵ degrees develop in conjunction with the rotation of the specimen through ɵ degrees, a constant 2:1 ratio [182]. The data is expressed in a collection of single-phase X-ray powder diffraction (XRPD) patterns for the three great acute D values in the form of tables of inter-planar spacing(D), relative intensities(I/Io), and materials name [184]. XRPD can be used to investigate crystal structures using Rietveld refinement, determine modal amounts of minerals (quantitative analysis), lattice parameters, calculate stress

and strain, determining disorder density and quality of the film by convulsing curve analysis [183]. Figure 6.2 shows an example of X-ray powder diffractiometer.

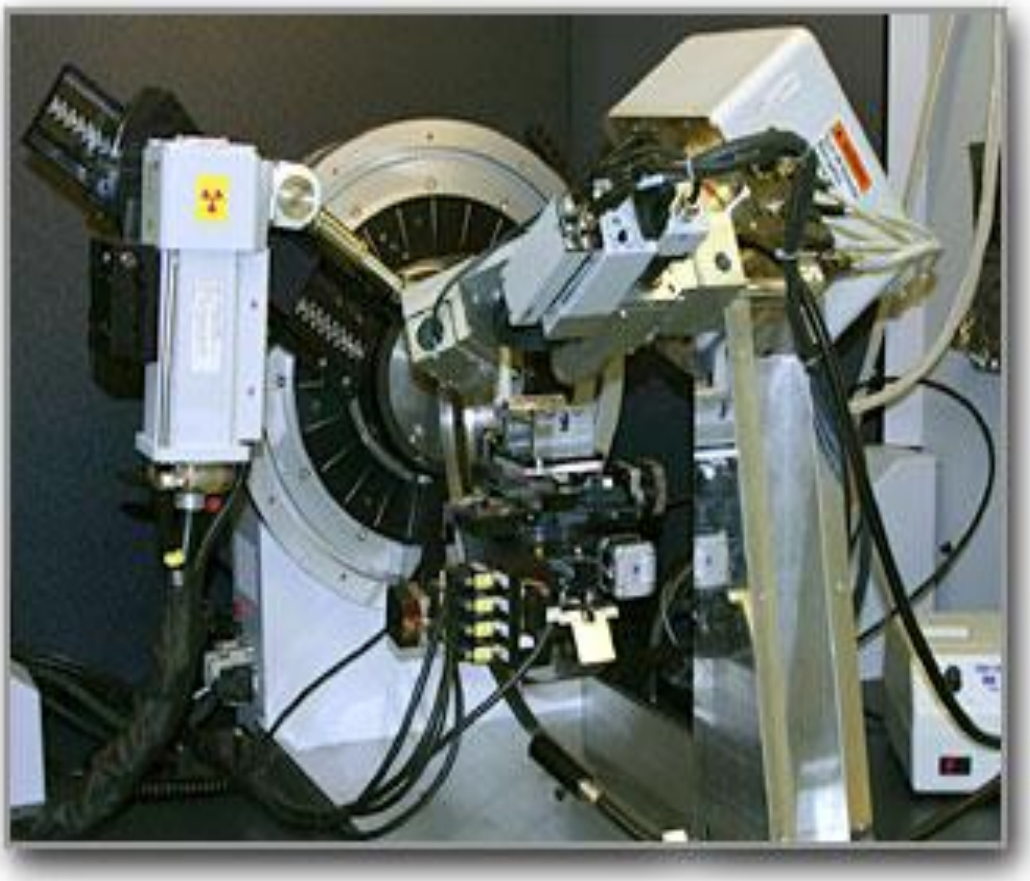

Figure 6. 2: x-ray powder diffraction equipment
http://www.grc.nasa.gov/WWW/StructuresMaterials/ASG/XRay/index.html

6.2.4 X-ray powder diffraction (XRPD) preparation

Both samples of graphene and carbon nanotube were bought from a chemical company called Sigma-Aldrich. The samples were heated at a temperature of 300 ^{0}C and 600 ^{0}C for one hour each. The samples were then characterised using X-ray powder diffraction (XRPD) (Siemens D500).

6.3 Results and Discussion

In this section, the AFM and XRD characterisation results of a single-walled carbon nanotubes and graphene are presented and discussed.

6.3.1 Atomic force microscope results of single-walled carbon nanotubes

The AFM images show the bundles and individual carbon nanotubes in different solvents. This method of characterising carbon nanotubes gives us information about the width of nanotubes and approximate valuation of the bundles diameter. In the present work the diameter of the SWCNT was estimated from the height of SWCNT in AFM images because the lateral dimensions of the tubes are enhanced by the tip radius [186]. The diameter of single-walled carbon nanotubes (SWCNTs) represents a critical structural aspect as it determines many electronic and chemical properties. For instance, diameter determines the metallicity due to the inverse proportionality with the band gap [186]. Similarly, thermal properties are also dictated by the diameter as curvature is related with Umklapp scattering [189]. Finally, diameter determines the radius of curvature of the tube which affects surface functionalization [190]. Therefore, diameter can represent an important structural parameter of SWCNTs; however, precise control of the SWCNT diameter over a wide range is yet to be demonstrated. The diameter and the helicity of carbon atoms in the nanotube shell are believed to determine whether the nanotube is metallic or a semiconductor [194]. In this case the diameter of a SWCNT was estimated from the height of SWCNTs in AFM images.
One drop of prepared solution was spin coated on a Si substrate. The sample was investigated using the AFM in a taping mode. About ten areas of 1x1 μm were scanned until nanotubes were found indicating a very low convergence of tubes. It was noticed that some tubes are buckled and bent; this might be because of ultrasonic treatment.

6.3.1.1 AFM images of SWCNT using ethanol solvent

On AFM images the width and the height of a single-walled carbon nanotubes can be determined by drawing a small line on the image where a smooth curved graph will be plotted like in figure 6.3 [186]. The graph in figure 6.3 shows the diameter of 8.5 Å which is represented by the height on the y axis and x-axis represents the width. Figure 6.4 shows some nanotubes prepared using ethanol solvent. Because of the shape of the nanotubes that appears on our AFM images, we can assume that the nanotubes are perfectly cylindrical [186].

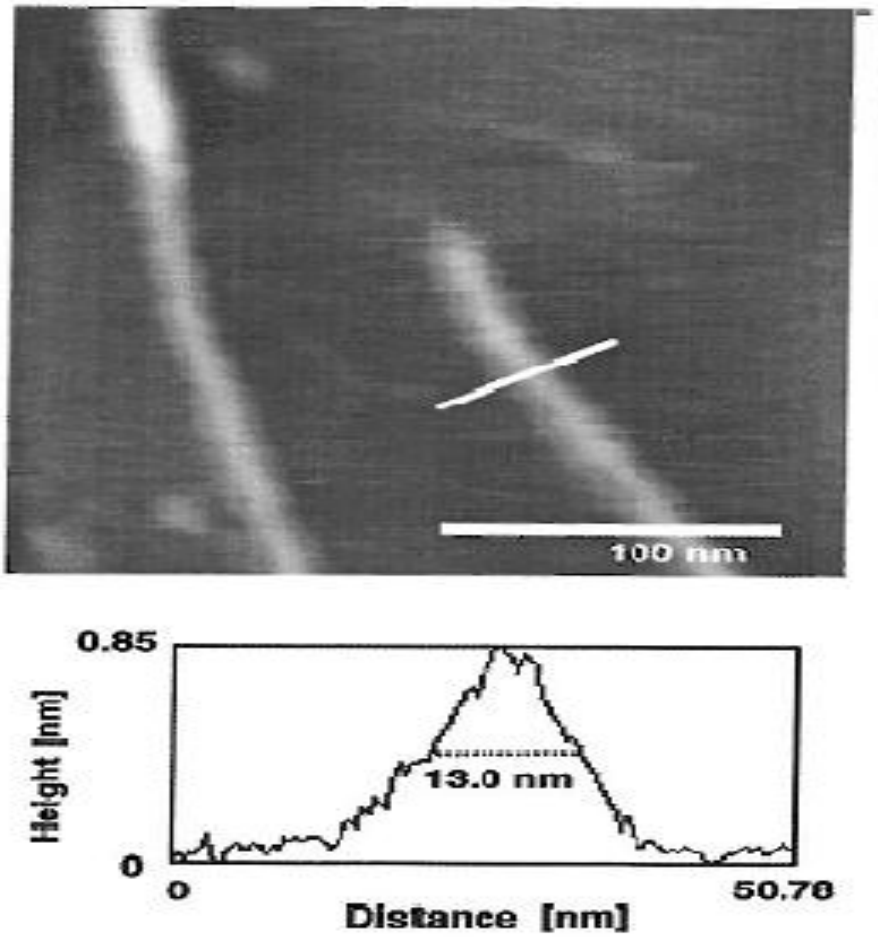

Figure 6. 3: AFM image of SWCNT using conventional Si tip. [186]

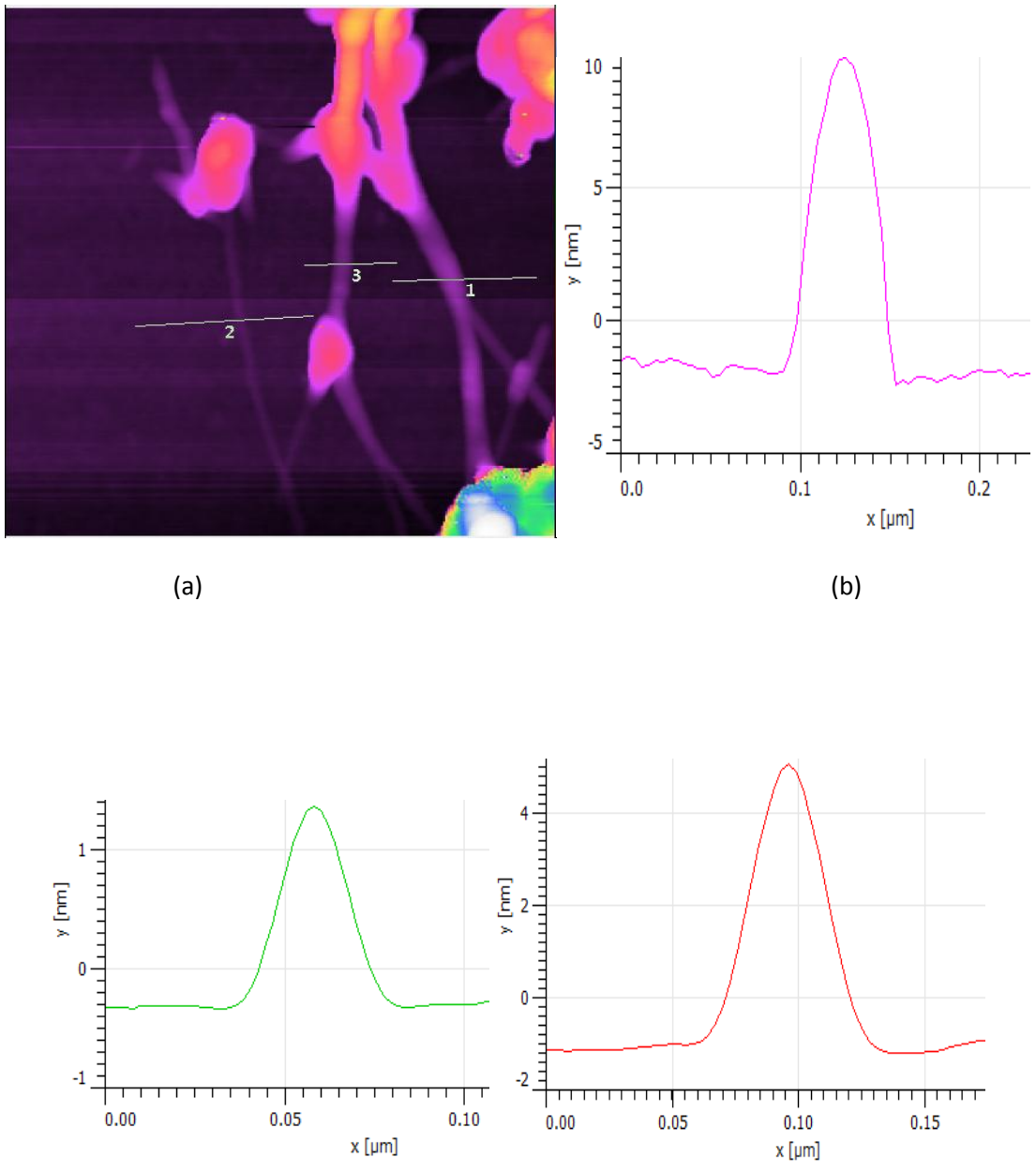

Figure 6. 4: AFM images of SWCNT and corresponding wall diameter plots. Scan 1 corresponds to plot (b), 2 corresponds to plot (c), and 3 corresponds to plot (d).

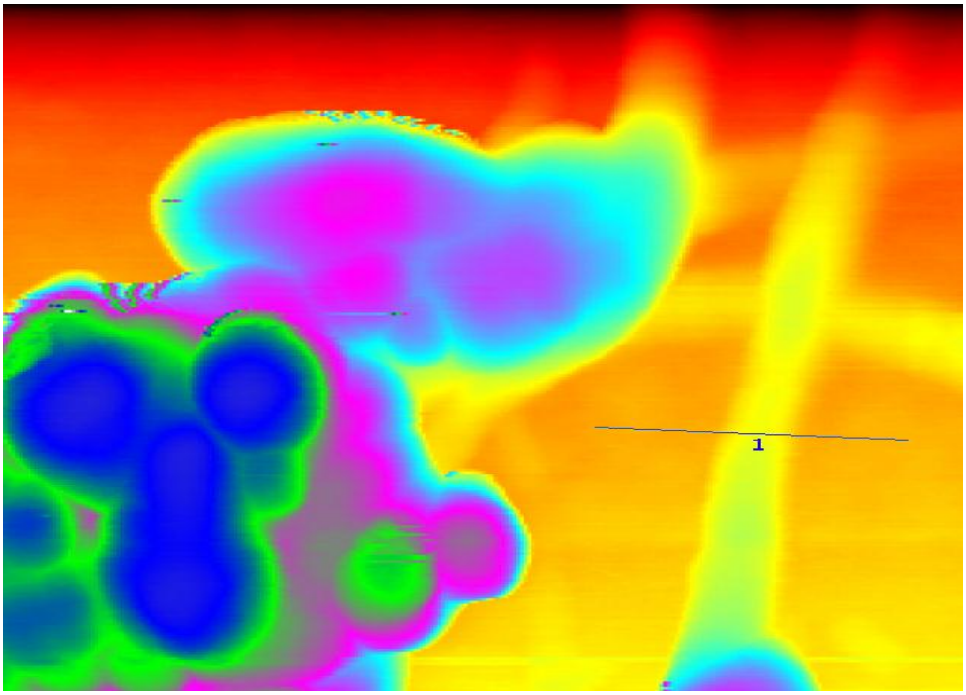

(a)

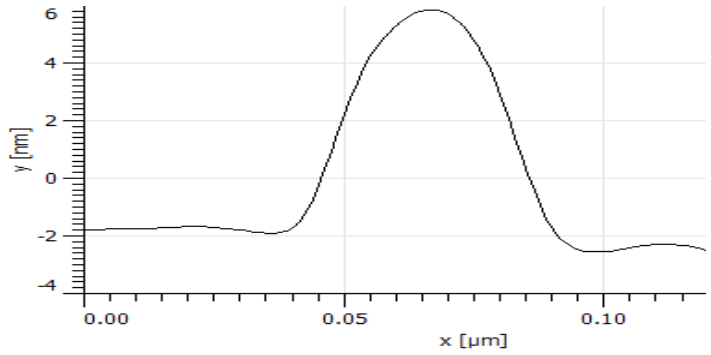

(b)

Figure 6. 5: AFM image of SWCNT and the corresponding wall diameter plot

On these graphs, the width of 600 Å, 390 Å and 550 Å are determined for figure 6.4 b, c and d respectively with the diameters of 119 Å, 15.3 Å and 57.7 Å for figure 6.4 b, c and d respectively. Figure 6.5 shows another nanotube in our sample. It has a diameter of 75.4 Å with a width of 512 Å. An individual carbon nanotube has a diameter of 6.0-20.0 Å [188]. In this case one carbon nanotube has the diameter of 15.3 Å which falls under the range of diameter of single-walled carbon nanotubes. Some of the images might be the bundles of single-walled carbon nanotubes because of their diameter. The bundles of single-walled carbon nanotubes can have the diameter of up to 70.0 Å [156,168]. Wade at al. [187] managed to get the diameter of single-walled

carbon nanotubes that range from 42 to 65 Å, which shows that some of our diameters agree with his results. The bundles might be caused by sonication time.

6.3.1.2 AFM images using chloroform as a solvent

Figures 6.6 and 6.7 show AFM images of SWCNT prepared using chloroform as a solvent. In the first image figure 6.6, one can only see the bundles of carbon nanotubes. And in figure 6.7, the graph shows that a single tube was not found but only the bundles that might have many tubes. Chloroform solvent did not give us good results. It was not easy to determine the length and the diameter in these two images.

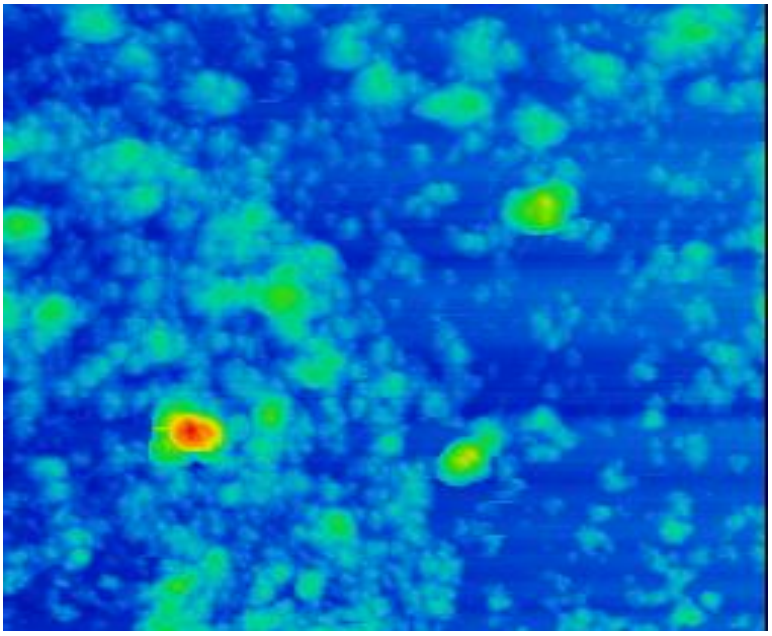

Figure 6. 6: AFM image of SWCNT

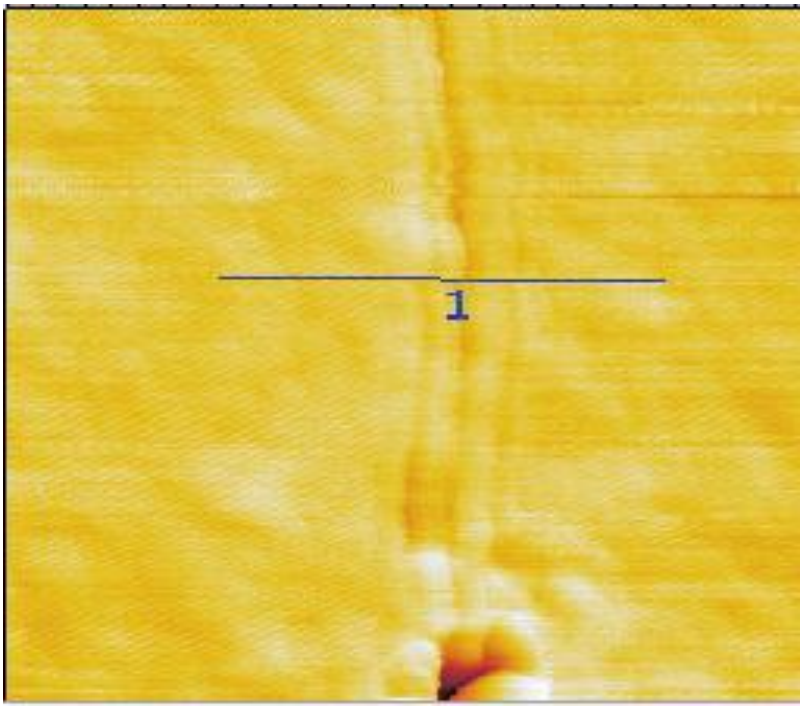

(a)

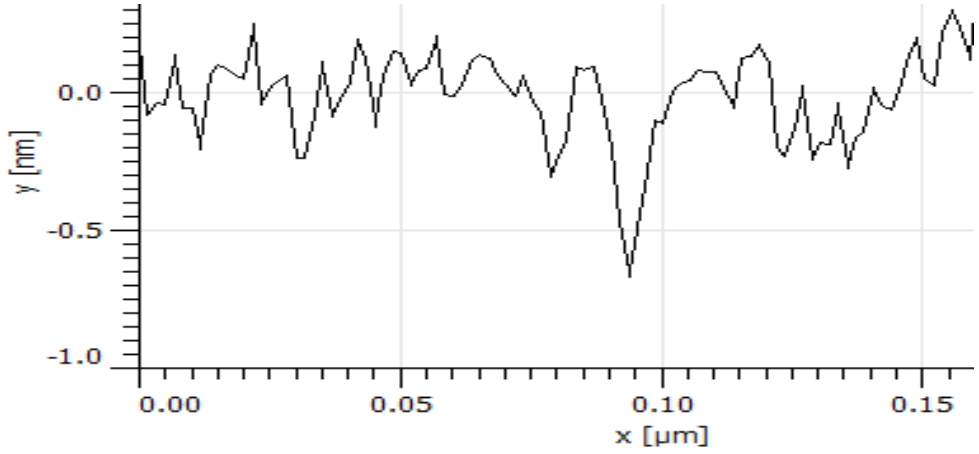

(b)

Figure 6. 7: AFM image of SWCNT and the corresponding wall diameter plot

6.3.2 XRD results of graphene

Figures 6.8 - 6.10 were used as references to find the planes of the peaks that appear in figure 6.11. Peaks around 26.4^0 and 43.1^0, correspond to the {002} and {100} diffractions of graphite, respectively [191].

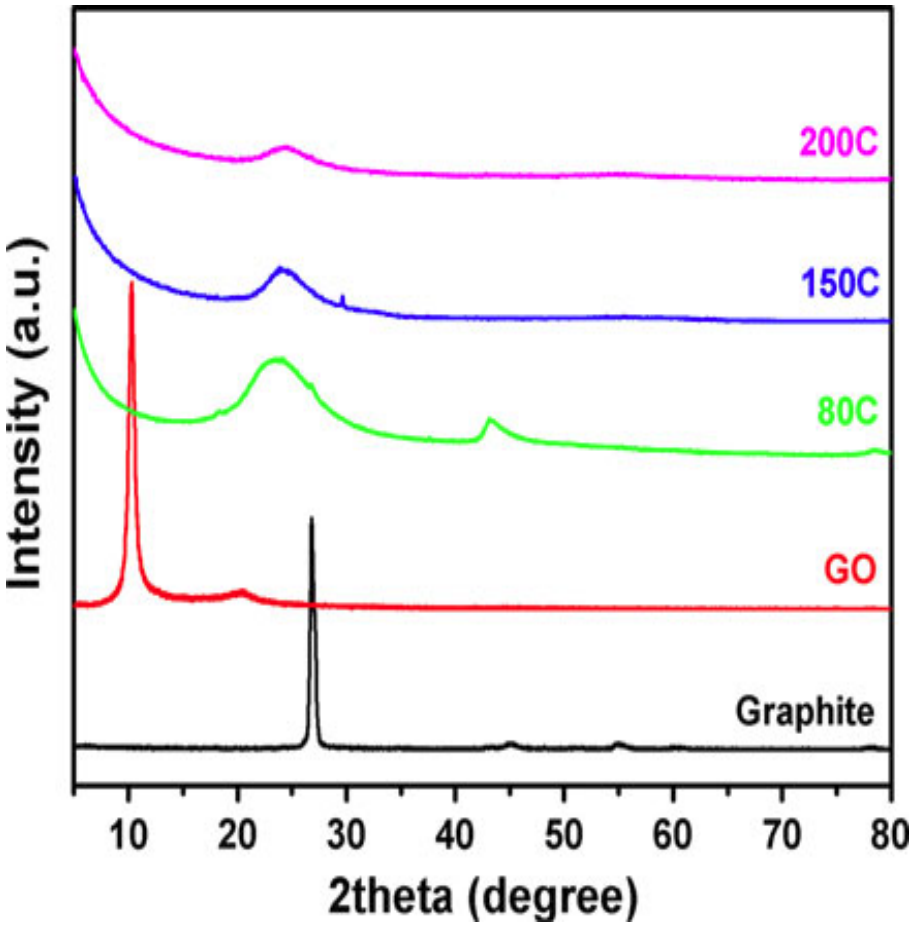

Figure 6. 8: XRD patterns of graphite, GO, HRGN-80, HRGN-150and HRGN-200 [191]

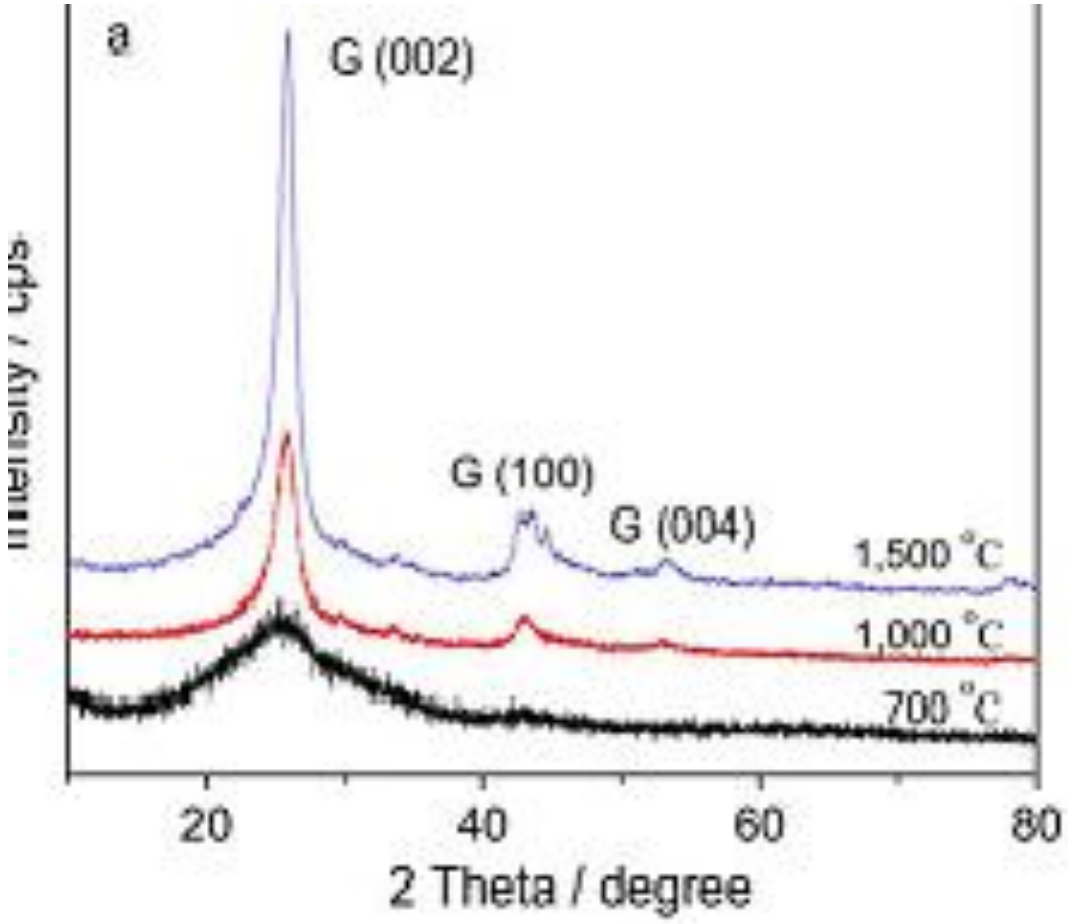

Figure 6. 9: XRD patterns of graphite at different temperatures [193]

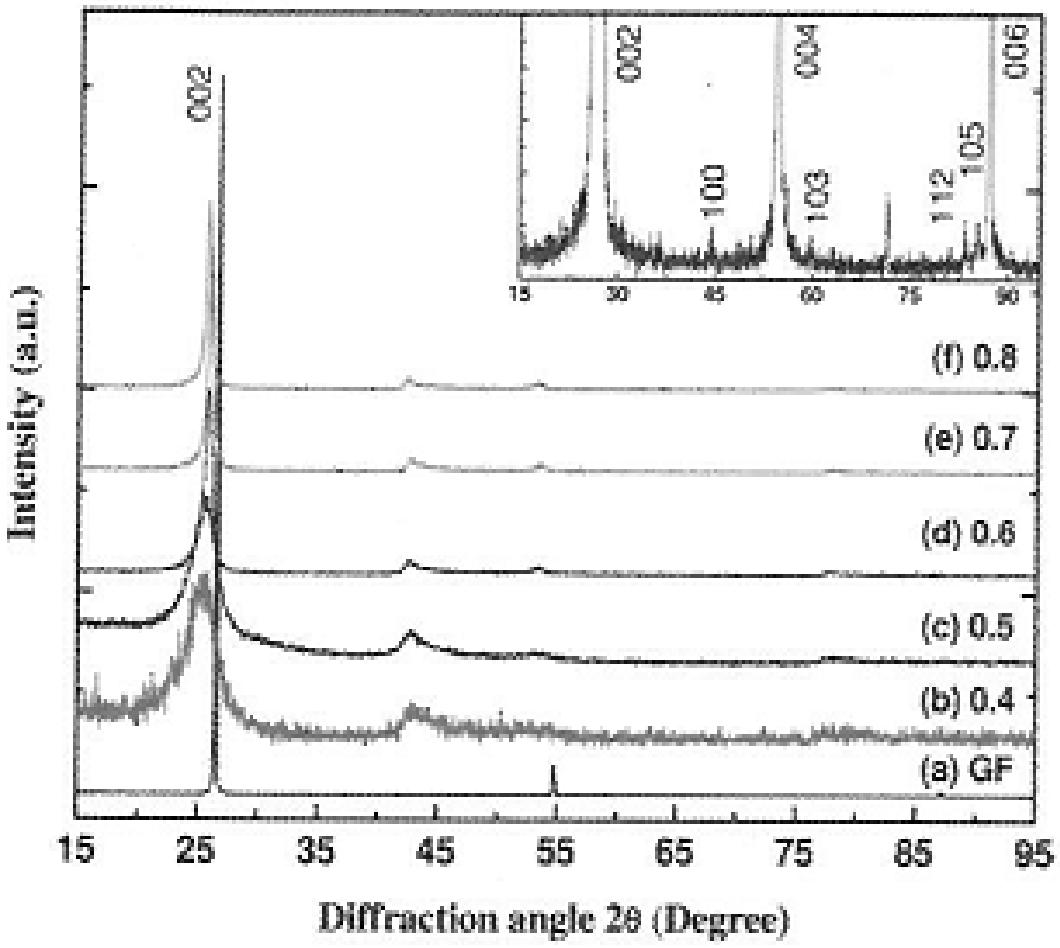

Figure 6. 10: XRD patterns of (a) graphite flakes (GF), and ((b)–(f)) the detonation carbon graphene nanosheets (GNs) [191]

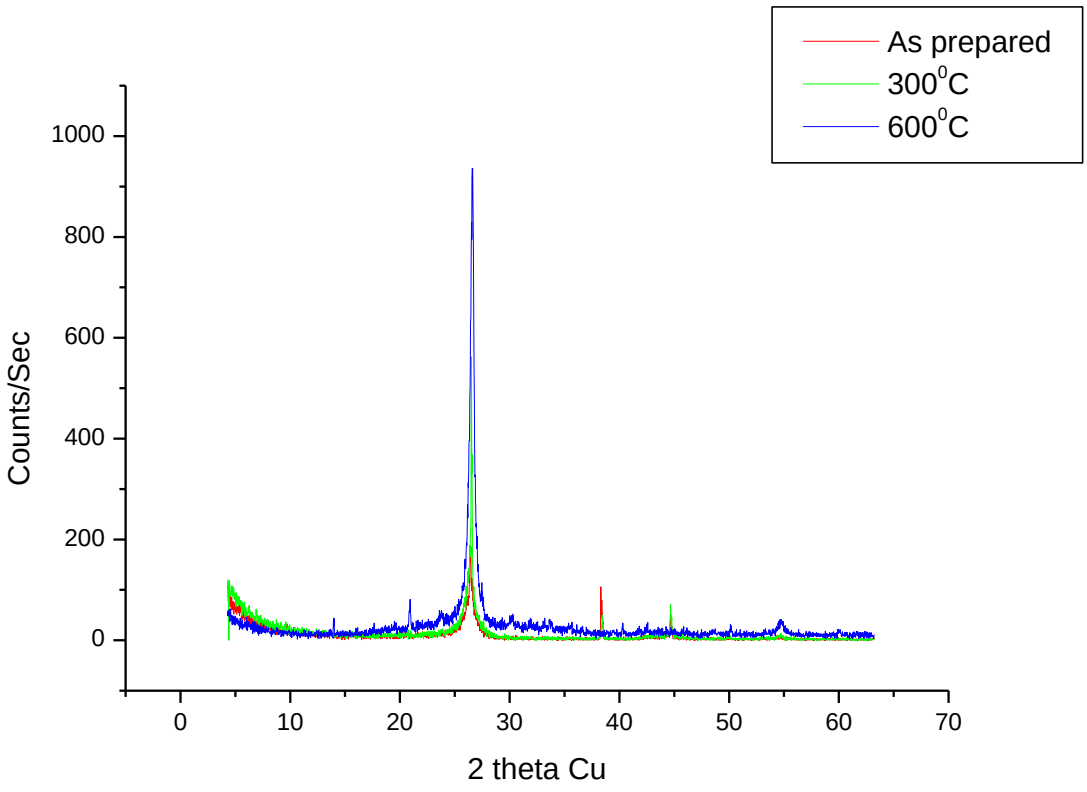

Figure 6. 11: XRDs of graphene Cu Kα

For as prepared sample, three peaks appearing at 26.4^0, 38.4^0 and 44.7° are observed. For 300 ^{0}C, the peaks are observed at 26.5^0, 38.4^0 and 44.7^0 and for 600 ^{0}C at 26.6^0, 42.3^0 and 55.2^0. As the temperature increases, the height of the peak of 002 increases and becomes sharp whereas the width decreases. For simplicity and clarity, the first peak is (002) because is similar with the one from graphite. In all the three samples, two peaks were used to calculate the lattice constants. For as prepared sample, 002 at 26.4^0 (d=3.370 Å) and 100 at 44.7^0 (d=2.026 Å), 300 ^{0}C 002 at 26.5^0 (d=3.359 Å) and 100 at 44.7^0 (d=2.026 Å) and 600 ^{0}C 002 at 26.6^0 (d=3.351 Å) and 100 at 42.3^0 (d=2.135 Å) were used to calculate the lattice constants and d spacing. The lattice constant (a) of as-prepared and 300^0C are the same with the value of 2.339 Å, which differs with the one from the literature by 9.0 %. For 600 ^{0}C, the lattice constant (a) is equal to 2.452 Å which differs with the one from the literature by 0.3%. The lattice constant (c) for as-prepared sample differs with the one from the literature by 1.0 %, 300 ^{0}C differs by 1.0 % and 600 ^{0}C differs by 1.5%. The percentage difference shows that the results of the lattice constants are in agreement with the one from the literature [13,180-182]. Table 6.1 shows the results of lattice constants for graphene.

Table 6.1: XRD results of graphene

Temperature	Lattice constants (Å)			Literature (Å) [13]	
	a	b	c	a	c
As prepared	2.34	2.34	6.74	2.46	6.80
300^0C	2.34	2.34	6.72		
600^0C	2.45	2.45	6.70		

6.3.3 XRD results of single-walled carbon nanotubes

Because of the first peak that appears at 002, the structure of these single-walled carbon nanotubes is perfectly hexagonal. The same equation that was used to calculate the lattice constants of graphene is used to calculate the lattice constants of

single-walled carbon nanotubes. Figure 6.12 was used to calculate the results that are tabulated in table 6.2. The d spacing for the peaks in this study ranges from 3.35 to 3.36 Å, which agrees well with the theoretical value of 3.42 Å in a carbon nanotube crystal predicted by Tersoff et al [194] based on van de Waals interaction. It is close to the experimental average value of 3.44 Å in the C_{60} crystal [194]. The lattice constants and d-spacing were calculated using the same equations that were used in graphene's calculation, because the structure of single-walled carbon nanotubes that was used here is hexagonal like graphene. For as prepared sample, the peaks are at 26.4º, 38.5º and 44.5º whereas for 300 ºC, peaks are at 26.5^0, 38.4^0 and 44.5^0 and for 600 ^{0}C, peaks are at 26.6º, 42.4º and 54.7º. To calculate the lattice constants, two peaks were used in each sample. For as prepared sample the peaks that were used are 26.4^0 (d=3.37 Å) and 44.5º (d=2.03 Å), for 300 ^{0}C are 26.5º (d=3.36 Å) and 44.5^0 (2.03 Å) and for 600 ºC are 26.6º (d=3.35 Å) and 42.4º (d=2.24 Å). The lattice constants (a) for as-prepared and 300 ºC sample are the same which differs with the one from the literature by 4.62%. The lattice constant (a) for 600 ^{0}C differs with the one from the literature by 0.2%. As prepared sample's lattice constant (c) differs with the one from the literature by 0.9%, for 300 ^{0}C differs by 1.2% and 600 ºC differs by 1.3%. The percentage difference shows that the lattice constants are in agreement with the one from the literature [191].

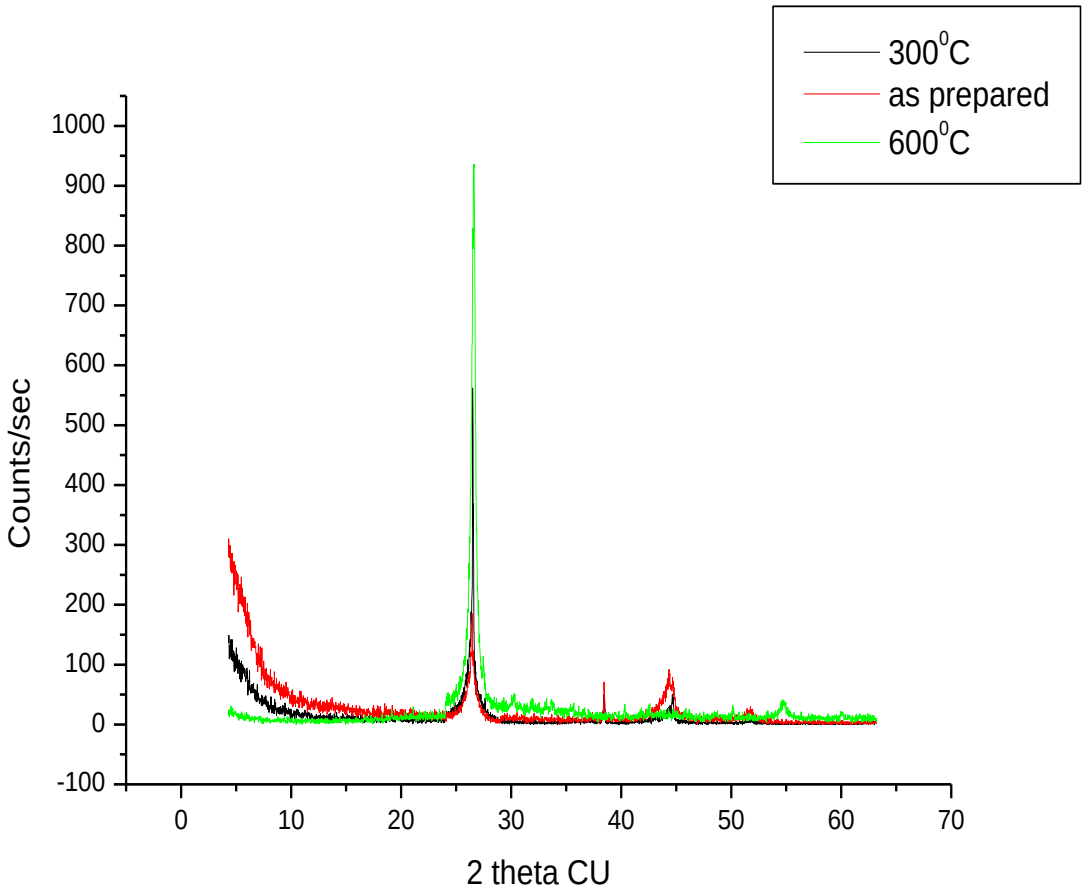

Figure 6. 12: XRDs of single-walled carbon nanotubes Cu Kα

Table 6. 2: XRD results of single-walled carbon nanotubes

Temperature	Lattice constants (Å)			Literature (Å) [13]	
	a	*b*	*c*	*a*	*c*
As prepared	2.35	2.35	6.74	2.46	6.80
300^{0}C	2.35	2.35	6.72		
600^{0}C	2.47	2.47	6.71		

6.3 Conclusion

The AFM result for ethanol solvent appears to show some convincing carbon nanotubes images. Those carbon nanotubes have different diameters and lengths. But the one for chloroform solvent, no visible carbon nanotubes imaging was observed. In the present work it shows that ethanol is the best solvent than chloroform. The diameter of SWNCT as calculated in chapter 5 ranges from 14.93 -16.27 Å. The experimental value of the diameter of SWCNT as presented in this chapter is 15.3 Å. This shows the agreement between the computational and experimental method. The XRD results of graphene and single-walled carbon nanotubes are similar. The lattice constants of both samples increase slightly when increasing the temperature. The lattice constants of graphene and SWCNT obtained experimentally in this chapter agree with the calculated one in chapter 4 and 5 which are for graphene and SWCNT respectively. This shows that both the computational and experimental approaches can be used to calculate the lattice constants of nano materials.

References

[1] http://www.nyu.edu/pages/mathmol/modules/carbon/carbon1.html (1999)

[2] N.D. Mermin, Crystalline Order in two dimensions, *Physics Review letter 176,* 250-256 (1968)

[3] P.J.F. Harris Structure of non-graphitising carbons International Materials Reviews 42,206-207(1997)

[4] U. Boser, "Diamonds on Demand". *Smithsonian 39,* 52–59 (2008)

[5] A. Fasolino, J.H. Los and M.I. Katsnelson, Intrinsic ripples in graphene, *Nature Materials 6*, 858-861 (2007)

[6] X. Wang, Q. Li, and J, Xie, Z. Jin, J. Wang, Y. Li, K. Jiang and S. Fan, Fabrication of ultralong and electrically uniform single-walled carbon nanotubes on clean substrates "*Nanotechnology Letters 9,* 3137–3141 (2009)

[7] J.C. Meyer, A.K. Geim, M.I. Katsnelson, K.S. Novoselov, T.J. Booth, S. Roth, The structure of suspended graphene sheets, *Nature Material 446*, 60-63 (2007)

[8] S.D. Sarma, Electronic transport in two-dimensional graphene, *Reviews of modern physics 83*(2), 407-470 (2011)

[9] A.K. Geim and K.S. Novoselov, The rise of graphene, *Nature Materials 6,* 183-191 (2007)

[10] D. Bolmatov, Thermodynamic properties of tunneling quasiparticles in graphene-based structures, *Physica C 471,* 1651–1654 (2011)

[11] I.W. Frank, D.M. Tanenbaum, A.M. Vander Zande and P.L. McEuen, Mechanical Properties of Suspended Graphene Sheets, *Journal of Vacuum Science and Technology B* 25 2558-2561 (2007)

[12] X. Wang, L.X. Zhi and K. Mullen, Transparent conductive graphene electrodes for dye-sensitized solar cells, *Nanotechnology Letter* 8 323-327 (2008)

[13] X.R. Wang, Y.J. Ouyang, X.L. Li, H.L. Wang, J. Guo and H.J. Dai, Room temperature all-semiconducting sub-10-nm graphene nanoribbon field-effect transistors, *Physics Review Letter 100*, 206803(1-7) (2008)

[14] D.S.L. Abergel, V. Apalkov, J. Berashevich, K. Zieglerc and T. Chakraborty, Properties of graphene: a theoretical perspective, *Advance in Physics 59*, 261–482 (2010)

[15] J.J. Zhao, A. Buldum, J. Han and J.P. Lu Gas molecule adsorption in carbon nanotubes and nanotube bundles, *Nanotechnology 13*, 195-200 (2002)

[16] A.M. Fischer, A.R. Romer and A.B. Dzyubenko, Magnetoplasmons and SU (4) symmetry in graphene, *Journal of Physics Condense Matter, 286* 012054 (2011)
[17] Y. Noel, P.D. Arco, R. Demicheslis, C.M. Zicovich-Wilson and D. Roberto, On the use of symmetry in the ab initio quantum mechanical simulation of nanotubes and related materials, *Journal of Chemistry 3*,1 855–862 (2010)
[18] F. Schedin, A.K. Geim, S.V. Morozov, E.W. Hill, P. Blake, M.I. Katsnelson and K.S. Novoselov, Detection of individual gas molecules adsorbed on graphene, *Nature Material 6* 652-655 (2007)
[19] L. Liao and X. Duan, Graphene-dielectric integration for graphene transistors *Materials Science and Engineering 70* 354-370 (2010)
[20] P.L. Neumann, Large scale nanopatterning of graphene, *Physics Research B 282*, 130-133 (2012)
[21] C. Dekker, Carbon nanotubes as molecular quantum wires, *Physics Today 52* 22–28 (1999)
[22] Y.K. Kwon, Y.K and D. Tomanek, Electronic and structural properties of multiwall carbon nanotubes *Physics Review B 58* 48824-1116 (1998)
[23] D.L. Majure, R.W. Haskins, N J. Lee, C R. Welch and C F. Cornwell, Tight-binding molecular dynamics study of the role of defects on carbon nanotube moduli and failure, *Journal of Chemical Physics 127*, 074708 (1-10) (2007)
[24] M. Damnjanović, B. Nikolić, and I. Milošević, Symmetry of nanotubes rolled up from arbitrary two-dimensional lattices along an arbitrary chiral vector, *Physics Review B 75*, 0334031-0334034 (2007)
[25] M. Damnjanović, I. Milosevic, T. Vuković, and R. Sredanović, Full symmetry, optical activity and potentials of single-wall and multiwall nanotubes, *Physics Review B 60*, 2728-2739 (1999)
[26] I. Milošević and M. Damnjanović, Symmetry of rolled-up rectangular lattice nanotubes*, Journal Physics: Condense Matter 18*, 8139-8147 (2006)
[27] I. Milošević and M. Damnjanović, Normal vibrations and Jahn-Teller effect for polymers and quasi-one-dimensional systems, *Physics Review B 47*, 7805-7818 (1993)
[28] R.H. Baughman, A.A. Zakhidov and W.A. Zakhidov: Carbon nanotubes – the route toward applications, *Science 297*, 787–792 (2002)
[29] K. Nomura and A.H. MacDonald, Quantum Hall ferromagnetism in graphene, *Physical Review Letters 96*, 256602(1-4) (2006)

[30] Y.K. Bahk, J. Buha and J. Wang, Determination of geometrical length of airborne carbon nanotubes by electron microscopy, model calculation and Filtration Method, *Aerosol Science and Technology* 47, 776-784 (2013)

[31] M. Li, G.W. Mulholland and M.R. Zachariah, The effect of orientation on the mobility and dynamic shape factor of charged axially, symmetric particles in an electric field, *Aerosol Science and Technology* 46, 1035–1044 (2012)

[32] A. Nicholas, G. Parra-Vasquez, I. Stepanek, V.A. Davis, V.C. Moore, E.H. Haroz, J. Shaver, R.H. Hauge, R.E. Smalley and M. Pasquali, Simple length determination of single-walled carbon nanotubes by viscosity measurements in dilute suspensions, *Macromolecules* 40, 4043-4047 (2007)

[33] K.S. Novoselov, V.I. Fal'ko, L. Colombo, P.R. Gellert, M.G. Schwab and K. Kim, A roadmap for graphene, *Nature Material 49*0 (2012)

[34] M. Andersson, L. Hultman, S.A. Lloyd, R. Pearce and R. Yakimova, Field effect transistor for chemical sensing using graphene, chemical sensor using the transistor and method for producing the transistor, *WO2012150884 A1*, (2011)

[35] W. Yuan and G. Shi, Graphene-based gas sensors, *Journal of material chemistry 35*, 10078-10091 (2013)

[36] J. Kong, N.R. Franklin, C. Zhou, M.G. Chapline, S. Peng, K. Cho and H. Dhai, Nanotube Molecular Wires as Chemical Sensors, *Science 287*, 622-625 (2000)

[37] Y. Wang and J.T.W. Yeow, A Review of Carbon Nanotubes-Based Gas Sensors, *Journal of Sensors 45*, 493904 (1-24) (2009)

[38] M.L. Sin, G.C.T. Chow, G.M.K. Wong, W.J. Li, P.H.W. Leong and K.W. Wong, Ultralow-power alcohol vapour sensors using chemically functionalized multi-walled carbon nanotubes, *Transactions on Nanotechnology 6*, 571-577 (2007)

[39] Y.P. Dan, Y. Lu, N.J. Kybert, Z.T. Luo, and A.T.C. Johnson, Intrinsic response of graphene vapour sensors, *Nanotechnology Letter 9*, 1472-1475 (2009

[40] J.L. Johnson, A. Behnam, Y. An, S.J. Pearton and A. Ural, Experimental study of graphitic nano-ribbon films for ammonia sensing, *Journal of Applied Physics 109*, 124301-7 (2011)

[41] B.H. Chu, J. Nicolosi, C.F. Lo, W. Strupinski, S.J. Pearton and F. Ren, Effect of coated platinum thickness on hydrogen detection sensitivity of graphene-based sensors. *Electrochemical Solid-State Letter 14*, 1099-1102 (2011)

[42] H.T. Wang, B.S. Kang, F. Ren, R.C. Fitch, J.K. Gillespie and N. Moser, Comparison of gate and drain current detection of hydrogen at room temperature with

AlGaN/GaN high electron mobility transistors, *Applied Physics Letter 87,* 172105(1-5) (2005)

[43] H.T. Wang, B.S. Kang, F. Ren, L.C. Tien, P.W. Sadik and D.P. Norton, Hydrogen selective sensing at room temperature with ZnO nanorods, Applied *Physics Letter 86,* 243503(1-6) (2005)

[44] H.T. Wang, T.J. Anderson, B.S. Kang, F. Ren, C. Li and Z.N. Low, Stable hydrogen sensors from AlGaN/GaN heterostructure diodes with TiB[sub 2]-based Ohmic contacts, *Applied Physics Letter 90*, 252109(1-8) (2007)

[45] L.K. Randeniya, P.J. cMartin, A. Bendavid and J. McDonnell, Ammonia sensing characteristics of carbon-nanotube yarns decorated with nano-crystalline gold. *Carbon 49*, 5265–5270 (2011)

[46] J.T. Robinson, F.K. Perkins, E.S. Snow, Z. Wei and P.E. Sheehan, "Reduced Graphene Oxide Molecular Sensors," *Nanotechnology Letters 10*, 3137-3140 (2008)

[47] A. Varezhnikov, A. Sinitskii, M. Augustin, M. Bruns, M. Sommer, V. Sysoev and A. Kolmakov, Simple graphene based multi-sensor array for gas analysis, IMCS, *the 14th International Meeting on Chemical Sensors* 1771-1772 (2012)

[48] D.F. Jesse, J.A. Matthew, C.T. Vincent, Y. Yang, B.K. Richard and H.W. Bruce, Practical Chemical Sensors from Chemically Derived Graphene, ACS *Nanotechnology letter 3*, 301-306 (2009)

[49] M. Quazi, G. Koley, NO2 detection using micro-cantilever based potentiometric, *Sensors 8*, 7144-7156 (2008)

[50] G. Koley, H.Y. Kim, Y.M. Park, K.Y. Lee and J. Kim, Graphene-based nitrogen dioxide gas sensors, *Applied Physics 10*, 1002-1004 (2010)

[51] J. Li, Y. Lu and Q. Yet, "Carbon nanotubes sensors for gas and organic vapour detection," *Nanotechnology Letters 3*, 929–933 (2003)

[52] Y.D. Lee, W.S. Cho and S.I. Moon, "Gas sensing properties of printed multi-walled carbon nanotubes using the field emission effect," *Chemical Physics Letters 433*, 105–109, (2006)

[53] K. Yamamoto, S. Akita, and Y. Nakayama, "Orientation and purification of carbon nanotubes using ac electrophoresis," *Journal of Physics D 31*, 34–36, 1998

[54] K. Bubke, H. Gnewuch, M. Hempstead, J. Hammer, and M.L.H. Green, "Optical anisotropy of dispersed carbon nanotubes induced by an electric field," *Applied Physics Letters 71*, 1906–1908 (1997)

[55] T. Prasse, J.Y. Cavaille, and W. Bauhofer, “Electric anisotropy of carbon nanofibre/epoxy resin composites due to electric field induced alignment,” *Composites Science and Technology 63,* 1835–1841 (2003)
[56] X.Q. Chen, T. Saito, H. Yamada, and K. Matsushige, “Aligning single-wall carbon nanotubes with an alternating-current electric field,” *Applied Physics Letters 78*, 3714–3716 (2001)
[57] X. Liu, J.L. Spencer, A.B. Kaiser, and W.M. Arnold, “Electric field oriented carbon nanotubes in different dielectric solvents,” *Current Applied Physics 4*, 125–128 (2004)
[58] F. Wakaya, T. Nagai, and K. Gamo, “Position control of carbon nanotube using patterned electrode and electric field,” *Microelectronic Engineering 63(1–3),* 27–31, (2002)
[59] R. Krupke, F. Hennrich, H.B. Weber, et al., “Contacting single bundles of carbon nanotubes with alternating electric fields,” *Applied Physics A 76(3),* 397–400, (2003)
[60] J. Suehiro, G. Zhou, H. Imakiire, W. Ding and M. Hara, Controlled fabrication of carbon nanotube NO2 gas sensor using di-electrophoretic impedance measurement, *Sensors and Actuators B 108*, 398–403 (200)
[61] Y.T. Jang, S.I. Moon, J.H. Ahn, Y.H. Lee and B.K. Ju, “A simple approach in fabricating chemical sensor using laterally grown multi-walled carbon nanotubes,” *Sensors and Actuators B 99*, 118–122 (2004)
[62] Y. Obeng and P. Srinivasan, Graphene: An overview of the material, devices, and applications, the electrochemical society interface, spring (2011)
[63] S. Peng and K. Cho, “Chemical control of nanotube electronics, *Nanotechnology 11*, 57–60, (2000)
[64] S. Maeng, Single-walled carbon nanotube network gas sensor, carbon nanotubes growth and applications, first edition, ISBN 978-953-307-566-2, 437-456, (2011)
[65] Q.P. Vermesh, O. Grecu, M. Javey, A. Wang, Q. Dai, H. Peng and S. Cho, Toward large array of multiplex functionalized carbon nanotube sensors for highly sensitive and selective molecular detection, *Nanotechnology Letters 3(3),* 347-351, 2003
[66] X.H. Zheng, X.L. Wang, T.A. Abtew and Z. Zeng, Building half-metalicity in graphene nanoribbons by direct control over edge states occupation, *Journal of Physical Chemistry C 114*, 4190-4193 (2010)

[67] S. Tongay, M. Lemaitre, X. Miao, B. Gila, B.R. Appleton and A.F. Hebard, Rectification at Graphene-Semiconductor Interfaces: Zero-gap semiconductor Based diodes, *Physical Review X 2,* 011002(1-10) (2012)

[68] Y. Lin, X. Li, D. Xie, T. Feng, Y. Chen, R. Song, H. Tian, T. Ren, M. Zhong, K. Wang and H. Zhu, Graphene semiconductor hetero-junction solar cells with modulated antireflection and graphene work function, *Energy and Environmental Science 6*, 108–115 (2013)

[69] E.V. Castro, K.S. Novoselov, S.V. Morozov, N.M.R. Peres, J.M.B. Lopes dos Santos, J. Nilsson, F. Guinea, A.K. Geim and A.H. Castro Neto, Biased bilayer graphene: Semiconductor with a gap tuneable by the electric field effect, *Physical Review Letter 99*, 216802(1-4) (2007)

[70] S.J. Tans, R.M. Verschueren, and C. Dekker, "Room temperature transistor based on a single carbon nanotube," *Nature Material 393*, 49-52 (1998)

[71] P.L. McEuen, M. F.uhrer and H. Park, Single-walled carbon nanotube electronics, *Nanotechnology 2*, 78-85 (2002)

[72] J. Park and P.L. McEuen, "Formation of a p type quantum dot at the end of an n-type carbon nanotube," *Applied Physics Letters 79*, 1363-1365, 2001

[73] A. Javey, M. Shim, and H. Dai, "Electrical properties and devices of large-diameter single-walled carbon nanotubes," *Applied Physics Letters 80*, 1064-1066 (2002)

[74] M.S. Fuhrer, B.M. Kim, T. Durkop and T. Brintlinger, High-mobility nanotube transistor memory, *Nanotechnology Letter 2*, 755-759 (2002)

[75] M. Radosavljevic, M. Freitag, K.V. Thadani and A.T. Johnson, Non-volatile molecular memory elements based on am-bipolar nanotube field effect transistors, *Nanotechnology Letter 2(7)* 761-764 (2002)

[76] A. Star, J.C.P. Gabriel, K. Bradley and G. Gruner, Electronic detection of specific protein binding using nanotube FET Devices, *Nanotechnology Letter 3(4),* 459-463 (2003)

[77] K. Besteman, J.O. Lee, F.G.M. Wiertz, H.A. Heering and C. Dekker, Enzyme-coated carbon nanotubes as single-molecule biosensors, *Nanotechnology Letter 3*, 727-730 (2003)

[78] R.J. Chen, S. Bangsaruntip, K.A. Drouvalakis, N.W.S. Kam, M. Shim, Y. Li, W. Kim, P.J. Utz and H. Dai, Non-covalent functionalization of carbon nanotubes for highly specific electronic biosensors, *Proceedings of the National Academy of Sciences of the united states of America 100*, 4984-4989 (2003)

[79] T. Durkop, S.A. Getty, E. Cobas, and M.S. Fuhrer, Extraordinary mobility in semiconducting carbon nanotubes, *Nanotechnology Letter 4(1),* 35-36 2004

[80] C.H. Chen and C.C. Huang, Hydrogen storage by KOH-modified multi-walled carbon nanotubes, *International Journal of Hydrogen Energy 32,* 237 – 246 (2007)

[81] Y.L. Chen, B. Liu, J. Wu, Y. Huang, H. Jiang and K.C. Hwang, Mechanics of hydrogen storage in carbon nanotubes, *Journal of the Mechanics and Physics of Solids 56,* 3224–3241(2008)

[82] A.C. Dillon, T. Gennett, J.L. Alleman, K.M. Jones, P.A. Parilla and M.J. Heben, Carbon nanotube materials for hydrogen storage, *Proceedings of the U.S DOE Hydrogen Program Review NREL/CP*-570, 26938(1-18) (1999)

[83] F.L. Darkrim, P. Malbrunot and G.P. Tartaglia, Review of hydrogen storage by adsorption in carbon nanotubes. *International Journal of Hydrogen Energy 27 (2)*, 193–202, (2002)

[84] A.C. Dillon, K.M. Jones, T.A. Bekkedahl, C.H. Kiang, D.S. Bethune, M.J. Heben, Storage of hydrogen in single-walled carbon nanotubes, *Nature 386*, 377–379 (1997)

[85] C. Liu, Y.Y. Fan, M. Liu, H.T. Cong, H.M. Cheng and M.S. Dresselhaus, Hydrogen storage in single-walled carbon nanotubes at room temperature, *Science 286 (5442),* 1127–1129 (1999)

[86] F.L. Darkrim and D. Levesque, High adsorptive property of opened carbon nanotubes at 77 K, *Journal of Physical Chemistry 104*, 6773–6776, (2000)

[87] Y. Jiang, A. Kozinda, T. Chang, L. Lin, Flexible energy storage devices based on carbon nanotube forests with built-in metal electrodes, *Sensors and Actuators A 195*, 224–230 (2013)

[88] G. Pistoia, Batteries for Portable Devices, Elsevier Science B.V, Amsterdam, The *Netherlands, ISBN: 978-0-444-51672-5* (2005)

[89] A.G. Pandolfo, A.F. Hollenkamp, Carbon properties and their role in super capacitors, *Journal of Power Sources 157*, 11–27 (2006)

[90] S.L. Candelaria, Y. Shao, W. Zhou, X. Li, Jie Xiao, J.G. Zhang, Y. Wan, J. Liu, J. Li, G. Cao, Nanostructured carbon for energy storage and conversion, Nano Energy 1, 195–220 (2012)

[91] C. Du and N. Pan, Carbon nanotube-based super capacitors, *Nanotechnology law and business 4*, 569-576, (2007)

[92] Z.G. Fthenakis, Z. Zhu, D. Teich, G. Seifert and D. Tomanek, Limits of mechanical energy storage and structural changes in twisted carbon nanotube ropes, Physical review B 88, 245402(1-11), (2013)

[93] P.A. Michael, Introduction to Molecular Dynamics Simulation, NIC Series 23, 1-28 (2004)

[94] X. Huang, Z. Yin, S. Wu, X. Qi, Q. He, Q. Zhang, Q. Yan, F. Boey and H. Zhang, Graphene-based materials: synthesis, characterization, properties and applications, *Small volume 7 issue 14*, 1876-1902 (2011)

[95] K.S. Novoselov, A.K. Geim, S.V. Morozov, D. Jiang, Y. Zhang, S.V. Dubonos, I.V. Grigoreiva and A.A. Firsov, Electric field effect in atomically thin carbon films, *Science 306*, 666-669 (2004)

[96] S.L. Altmann, A. Lapiccirella, K.W. Lodget and N.Tomassini, A valence force field for the silicon crystal, *Journal of Physics 15*, 5581-5591 (1982)

[97] P.A. Michael and J.D. Tildesley, Hard convex body fluids, *Computer simulation in chemical physics volume 397*, 211-259 (1993).

[98] M. Fritsche, R.B. Pandey, B.L. Farmer and D.W. Heermann, Conformational temperature-dependent behaviour of a histone H2AX: A coarse-grained Monte Carlo approach via knowledge-based interaction potentials, *Plos One V 7*, 32075(1-8) (2011)

[99] F. Hedman and A. Laaksonen A. Ewald summation based on non-uniform fast Fourier transform, *Journal of Chemical Physics 425,* 142-147 (2006)

[100] F. Ercolessi, A Molecular Dynamics Primer, (http://www. sica.uniud.it/ ercolessi/md/md) (1997)

[101] L. Verlet, Computer “Experiments” on Classical Fluids, Thermodynamical Properties of Lennard-Jones Molecules, *Physical Review Letter 159*, 98-103 (1967)

[102] W. Huang and B. Leimkuhler, The adaptive Verlet method, *Journal of Scientific Computing 18*, 239-256 (1997)

[103] V. Antohe and I. Gladwell, Performance of variable step size methods for solving model separable Hamiltonian systems, *Computers and Mathematics with Applications 40*, 1245-1262 (2004)

[104] L.F. Shampine, Mathematics Department Southern Methodist University Dallas, TX 75275 shampine@smu.edu

[105] P.A. Michael and D.J. Tildesley,"Computer Simulation of Liquids", Oxford University Press (1989)

[106] W.C. Swope, H.C. Andersen, P.H. Berens and K.R. Wilson, A Computer simulation method for the calculation of equilibrium constants for the formation of physical clusters of molecules: application to small water clusters, *Journal of Chemical Physics 76*, 637 649 (1982)

[107] R.W. Hockney, The Potential Calculation and Some Applications, *Methods in Computational Physics 9*, 135-211 (1970)

[108] T. Hammerschmidt and R. Drautz, Bond-order potentials for bridging the electronic to atomistic modelling hierarchies, *NIC Series Volume 42,* 229-246 (2009)

[109] J. Tersoff, New empirical model for the structural properties of silicon, *Physical Review Letter 56*, 632-635 (1986)

[110] J. Tersoff, New empirical approach for the structure and energy of covalent systems", *Physical Review B 37*, 6991-7000 (1988)

[111] J. Tersoff, "Empirical interatomic potential for silicon with improved elastic properties", *Physical Review B 38*, 9902-9905 (1988)

[112] J. Tersoff, Empirical interatomic potential for carbons, with applications to amorphous carbon, *Physical Review Letter 61*, 2879-2882 (1988)

[113] D.W. Brenner, Empirical potential for hydrocarbons for use in simulating chemical vapour decompositions of diamond films, *Physical Review B 42*, 9458-9471 (1990)

[114] K. Matsubara, K. Sugihara, and T. Tsuzuku, Electrical resistance in the c direction of graphite, *Physical Review B 46*, 1948-1948 (1992)

[115] D.W. Brenner, O.A. Shenderova, J.A. Harrison, S.J. Stuart, B. Ni, and S.B. Sinnott, A second-generation reactive empirical bond order (REBO) potential energy expression for hydrocarbons, *Journal of Physics: Condense Matter 14*, 783-802 (2002)

[116] J.H. Los and A. Fasolino, Intrinsic long-range bond-order potential for carbon: Performance in Monte Carlo simulations of graphitization, *Physical Review B 68*, 024107 1-024107 14 (2003)

[117] W. Zou, H.N.G. Wadley, X.W. Zhou, R.A. Johnson and D. Brownell, Surfactant-mediated growth of giant magneto-resistance multilayers, *Physical review B 64*, 174418(1-10) (2001)

[118] M.W. Finnis and J.E. Sinclair, “A simple empirical N-body potential for transition metals”, *Philosophical Magazine A 50*, 45-55 (1984)

[119] F. Stillinger and T.A. Weber, Computer simulation of local order in condensed phases of silicon, *Physics Review B 31*, 5262-5271 (1985)

[120] K. Charles and H. Kroemer, Thermal Physics, Second Edition, San Francisco: W.H. Freeman and Company 31 ff. ISBN 0-7167-1088-9 (1980)

[121] M.H. Lee, Ergo metric theory of the ergodic hypothesis, *Acta Physica Polonica B 5*, 1009-1024 (2010)

[122] A. Abragam and B. Bleaney, Electron Paramagnetic Resonance of Transition Ions, Clarendon Press, Oxford, 1970

[123] R. Balescu, Equilibrium and Nonequilibrium Statistical Mechanics, A Wiley-Interscience Publication, New York, 1975

[124] W. Smith, T.R. Forester and I.T. Todorov STFC Daresbury Laboratory Daresbury, Warrington WA4 4AD Cheshire, UK Version 2.18, August (2007)

[125] W. Smith and T.R. Forester, DL_POLY_2.0: a general-purpose parallel molecular dynamics simulation package, *Journal of Molecular Graphics and Modelling 14*, 136-141 (1996)

[126] K.S. Novoselov, D. Jiang, T. Booth, V.V. Khotkevich, S.M. Morozov, A.K. Geim, Two dimensional atomic crystals, *Proceeding of the National Academy of Sciences of USA 104*, 10451-10453 (2005)

[127] M.S. Dresselhaus, fifty years in studying carbon-based materials, *Physica Scripta T146*, 014002(1-10) (2012)

[128] J. Kunstmann, Z.C. Ouml, A. Quandt, H. Fehske, Stability of edge states and edge magnetism in graphene nanoribbons, *Physical Review B 83,* 045414(1-6) (2011)

[129] X. Zhong, R. Pander, S.P. Karna, Stacking dependent electronic structure and transport in bilayer graphene nanoribbons, *Carbon 50*, 784-790 (2012).

[130] J.M.B. Lopes dos Santos, N.M.R. Peres, and A. H. Castro Neto, Graphene Bilayer with a Twist: Electronic Structure, *Physical Review Letter 99*, 256802(1-4) (2007)

[131] M. Shai, T.E. Mosuang and K.E. Rammutla, Molecular dynamics simulations of bilayer graphene structures, *Proceedings of the 57th South African Institute of Physics Annual Conference,* ISBN: 978-1-77592-070-0, 602-607, (2014)

[132] Y. Pathania and P.K. Ahluwalia, Molecular dynamics study of two- and three-dimensional classical fluids using double Yukawa potential, *Journal of Physics 65*, 457-468 (2005)

[133] S. Reich, C. Thomsen and P. Ordejón, Elastic properties of carbon nanotubes under hydrostatic pressure, *Physical Review B 65*, 153407(1-4) (2002)
[134] S. Reich, J. Maultzsch and C. Thomsen, Tight-binding description of graphene, *Physical Review B 66*, 035412(1-5) (2002)
[135] D. Gray, A. McCaughan and B. Mooke, Crystal structure of graphite, graphene and silicon, *Physics for Solid State application 730*, 1-20 (2009)
[136] F.D. Murnaghan, The compressibility of media under extreme pressures, *Proceedings of the National Academy of Sciences, USA 30*, 244-247 (1944)
[137] L.A. Girifalco, M. Hodak, and R.S. Lee, Carbon nanotubes, buckyballs, ropes, and a universal graphitic potential, *Physical Review Letter 62*, 13104-13110 (2000)
[138] W.H. Moon, M.S. Son and H.J. Hwang, Molecular dynamics simulation of structural properties of cubic boron nitride, *Physica B 336*, 329-334 (2003)
[139] J. Krumhansl and H. Brooks, the lattice vibration specific heat of graphite, *Journal of Chemical Physics 21*, 1663-1669 (1953)
[140] E. Pop, V. Varshney and A.K. Roy, Thermal properties of graphene: Fundamentals and applications, *Material Research Science Bulletin Volume 37*, 1273-1282 (2012)
[141] K.V. Zakharchenko, J.H. Los, M.I. Katsnelson, and A. Fasolino, Atomistic simulations of structural and thermodynamic properties of bilayer graphene, *Physical Review B 81*, 235439(1-4) (2010)
[142] W. Bao, F. Miao, Z. Chen, H. Zhang, W. Jang, C. Dames, and C.N. Lau, Controlled ripple texturing of suspended graphene and ultrathin graphite membranes *Natter Material 4*, 562-566 (2009)
[143] J.W. Jiang, J.S. Wang, and B. Li, Thermal expansion in single-walled carbon nanotubes and graphene: Nonequilibrium Green's function approach, *Physical Review B 80*, 205429(1-7) (2009)
[144] D. Yoon, Y.W Son, and H. Cheong, Negative Thermal Expansion Coefficient of Graphene Measured by Raman Spectroscopy, *Nanotechnology Letter 11*, 3227–3231 (2011)
[145] H.W. Kroto, J.R. Heath, S.C. O'Brien, R.F. Curl and R.E. Smalley, C_{60} Buckminsterfullerene, *Nature Material 318*, 162−163 (1985)
[146] S. Iijima, Helical microtubules of graphitic carbon, *Nature Material 354*, 56 (1991)

[147] E. Abou-Hamad, M.R. Babaa, M. Bouhrara, Y. Kim, Y. Saih, S. Dennler, F. Mauri, J.M. Basset, C. Goze-Bac and T. Wagberg, Structural properties of carbon nanotubes derived from ^{13}C NMR, *Physical Review B 84*, 165417(1-6) (2011)

[148] M. Shai, T.E. Mosuang and K.E. Rammutla, Molecular dynamics studies of some carbon nanotubes chiral structures *Proceedings of the 59th South African Institute of Physics Annual Conference,* ISBN: 978-0-620-65391-6, 620- 625, (2014)

[149] D.H. Robertson, D.W. Brenner, J.W. Mintmire, Energetics of nanoscale graphitic tubules, *Physical Review B 45*, 12592(1-5) (1992)

[150] A. Pullen, G.L. Zhao, D. Bagayoko and L. Yang, Structural, elastic, and electronic properties of deformed carbon nanotubes under uniaxial strain, *Physical Review B 71*, 205410(1-5) (2005)

[151] G. Gao, T. Çağin and W.A. Goddard, Energetics, structure, mechanical and vibrational properties of single-walled carbon nanotubes, *Nanotechnology 9*, 184-198 (1998)

[152] D. Beeman, R. Silverman, R. Lynds and M.R. Anderso, Modelling studies of amorphous carbon, *Physical Review B 30*, 870-875, (1984)

[153] B.T. Bioko, L.S. Palatnik and A.S. Derevyanchenko, Structure of amorphous carbon films, *Doklady Akademii Nauk SSSR 179*, 316-320 (1968)

[154] J. Kakinoki, K. Katada, T. Hanawa and T. Ino, Electron diffraction study of evaporated carbon films, *Acta Crystallographica 13*, 171-179 (1960)

[155] A. Thess, R. Lee, P. Nikolaev, H. Dai, P. Petit, J. Robert, C. Xu, Y.H. Lee, S.G. Kim, A.G. Rinzler, D.T. Colbert, G.E. Scuseria, D. Tomanek, J.E. Fischer, R.E. smalley, Crystelline ropes of metallic carbon nanotubes, *Science 273*, 483-487 (1996)

[156] O. Bill, J. Liu and J.T. Yates, Characterization of single wall carbon nanotubes by nonane preadsorption, *Carbon 44*, 2039–2044 (2006)

[157] H. Robertson, D.W. Brenner and J.W. Mintmire, 'Energetics of nanoscale graphitic tubules' *Physical Review B 45*, 12592(1-11) (1992)

[158] H. Mori, S. Ogata, J. Li, S. Akita and Y. Nakayama, Energetics of plastic bending of carbon nanotubes, *Physical Review B 74*, 165418 (2000)

[159] A.N. Imtani and V.K. Jindal, Structure of chiral single-walled carbon nanotubes under hydrostatic pressure, Department of Physics, Panjab University, Chandigarh-160014, India,(2009)

[160] M. Pobov, M. Kvotani and Y. Koga, high pressure polymerization of single wall carbon nanotube, *Nasa-Cp 210948,* 681-686 (2001)

[161] A. Zett and J. Cumings, elastic properties of fullerenes, department of physics, university of California Berkeley USA, ISBN D-12-4457622/535-D0 (2001)

[162] K. Xue and Z. Xu, Hydrogenation of Carbon Nanotubes, *Journal of Applied Physics 96*, 780-783 (2001)

[163] H. Jiang, B. Liu, Y. Huang and K.C. Hwang, Thermal Expansion of Single Wall Carbon Nanotubes, *Journal of Engineering Material and Technology 126*, 265-270 (2004)

[164] Y. Maniwa, R. Fujiwara, H. Kira, H. Tou, H. Kataura, S. Suzuki, Y. Achiba, E. Nishibori, M. Takata, M. Sakata, A. Fujiwara, and H. Suematsu and Thermal expansion of single-walled carbon nanotube „SWNT… bundles: X-ray diffraction studies, *Physical Review B 64*, 241402 (1-3) (2001)

[165] W. Gomulya, G.D. Costanzo, E.J. de Carvalho, S.Z. Bisri, V. Derenskyi, M. Fritsch, N. Fröhlich, S. Allard, P. Gordiichuk, A. Herrmann, S.J. Marrink, M.C. Dos Santos, U. Scherf, M.A. Loi, Semiconducting single-walled carbon nanotubes on demand by Polymer Wrapping, *Advanced Materials 25*, 2948–2956, (2013)

[166] J.W. Jiang, J.S. Wang and B. Li, Thermal expansion in single-walled carbon nanotubes and graphene: Non-equilibrium Green's function approach, *Physical Review B 80*, 205429(1-7) (2009)

[167] P.M. Naveen, determination of coefficient of thermal expansion of single walled carbon nanotube, Florida state university college of engineering, (2005)

[168] S.S. Wong, A.T. Woolley, T.W. Odom, J. Huang, P. Kim, Dimitri V. Vezenov, and C.M. Lieber, Single-walled carbon nanotube probes for high-resolution Nanostructure imaging, *Applied Physics Letter 73*, 3465-3567 (1998)

[169] M. Zheng and E.D. Semke, Enrichment of single chirality carbon nanotubes, *Journal of American Chemical Society 129*, 6084 (2007)

[170] S.J. Tans, M.H. Devoret, H.J. Dai, A. Thess, R.E. Smalley, L.J. Geerligs and C. Dekker, Individual single-wall carbon nanotubes as quantum wires. *Nature 386*, 474 (1997)

[171] C.L. Cheung, J.H. Hafner, and C.M. Lieber, Carbon nanotube atomic force microscopy tips: Direct growth by chemical vapour deposition and application to high-resolution imaging, *Proceedings of the National Academy of Sciences 97*, 3809-3813 (2000)

[172] L. Chen, C.L. Cheung, P.D. Ashby, and C.M. Lieber, Single walled carbon nanotube AFM probes: Optimal imaging resolution of nanoclusters and biomolecules in ambient and fluid environments, *Nanotechnology Letter 4*, 1725-1731 (2004)
[173] G. Binnig, C.F. Quate, Ch. Geber, Atomic Force Microscope, *Physics Review Letters 56*, 930-934 (1986)
[174] G. Binnig, H. Rohrer, C.H. Gerber, E. Weibel, Surface Studies by Scanning Tunnelling Microscopy, *Physics review letter 49*, 57-61 (1982)
[175] R. Garcı´a, Amplitude modulation atomic force microscopy, WILEY-VCH Verlag and Co. KGaA, Boschstr.12, 69469 Weinheim, Germany ISBN: 978-3-527-40834-4 (2010)
[176] R.N. Parmar and D.G. Kuberkar, Studies on Structural, Transport and magnetic properties of mixed oxide perovskites, Saurashtra University Theses Service (2006)
[177] J. Su, Fabrication and characterization of mercurocuprate superconductors on silver substrates, Electronic Theses, Treatises and Dissertations Paper 1525 (2004)
[178] D.J. Muller, C. Schoenenberger, A. Engel and F. Schabert, Structural Changes in Native Membrane Proteins Monitored at Sub-nanometre resolution with the Atomic force microscope, *Journal of structural biology 119*, 149-157 (1997)
[179] P.K. Hansma, Tapping mode atomic force microscopy in liquids, Applied *Physics Letters 64*, 1738-174040 (1994)
[180] M.J. Pearson, Quantitative clay mineralogical analyses from the bulk chemistry of sedimentary rocks, *Clays and Clay Minerals 26*, 423--433 (1978)
[181] B.D. Hall, D. Zanchet and D. Ugarte; Estimating nanoparticle size from diffraction measurements, *Journal of Applied Crystallography 33*, 1335-1341 (2000)
[182] L.J. Poppe, V.F. Paskevich, J.C. Hathaway, and D.S. Blackwood, A laboratory manual for X-ray powder diffraction, U. S. Geological Survey Open-File Report 01-041 (2002)
[183] R. Barua, Pathways for tailoring the magneto structural response of FeRh-based systems, Chemical Engineering Dissertations Northeastern University Paper 21, http://hdl.handle.net/2047/d2000496, (2004)
[184] D.L. Bish and J.E. Post, Modern Powder Diffraction, *Mineralogical Society of America Volume 20*, ISBN 0-939950-24-3, 1-369 (1998)
[185] H.P. Klug and L.E. Alexander, X-ray diffraction procedures for polycrystalline and amorphous materials 2nd edition Wiley, New York (1974)

[186]. N. Choi, T. Uchihashi, H. Nishijima, T. Ishida, W. Mizutani, S. Akita, Y. Nakayama, M. Ishikawa and H. Tokumoto, Atomic force microscopy of single walled carbon nanotubes using carbon nanotube tip, *Jounal of Applied Physics* 39, 3707-3710 (2000)

[187] L.A. Wade, I.R. Shapiro, Z. Ma, S.R. Quake and C. Patrick, Collier Correlating AFM Probe Morphology to Image Resolution for Single-Wall Carbon Nanotube Tips, *Nanotechnology Letter* 4, 735-731 (2004)

[188] J.W.G. Wildöer, L.C. Venema, A.G. Rinzler, R.E. Smalley and C. Dekker, Electronic structure of atomically resolved carbon nanotubes, *Nature Material* 391, 59–62 (1998)

[189] C.H. Yu, L. Shi, Z. Yao, D.Y. Li and A. Majumdar, Thermal conductance and thermo power of an individual single-wall carbon nanotube. *Nanotechnology Letter* 5, 1842–1846 (2005)

[190] M.S. Strano, C.A. Dyke, M.L. Usrey, P.W. Barone, M.J. Allen, H. Shan, C. Kittrell, R.H. Hauge, J.M. Tour and R.E. Smalley. Electronic structure control of single-walled carbon nanotube functionalization, *Science* 301, 1519–1522 (2003)

[191] C. Ma, Z. Chen, M. Fang and H. Lu, Controlled synthesis of graphene sheets with tuneable sizes by hydrothermal cutting, *Journal of Nanoparticle Research* 14, 996 (1-9) (2012)

[192] X.X. Wang, Z.H. Tan, M. Zeng and J.N. Wang, Carbon nanocages: A new support material for Pt catalyst with remarkably high durability, *Scientific report* 4, 4437(1-11) (2014)

[193] A. Nepal, G.P. Singh, B.N. Flanders and C.M. Sorensen, One-step synthesis of graphene via catalyst-free gas-phase hydrocarbon detonation, *Nanotechnology* 24 245602 (1-7) (2013)

[194] J. Tersoff and R.S. Ruoff , Structural Properties of a Carbon-Nanotube Crystal, *Physics review Letter* 73, 676-67

[195] Z. Nan, C. Wei, Q. Yang, and Z. Tan, Thermodynamic Properties of Carbon Nanotubes, *Journal of Chemical Engineering* 54, 1367-1370 (2009)

[196] T.W. Ebbesen, H.J. Lezec, H. Hiure, J.W. Bennett, H.F. Ghaemi and T. Thio, *Nature 382*, 54-, (1996)

[197] K.S. Subrahmanyam, S.R.C. Vivekchand, A. Govindaraj and C.N.R. Rao, A study of graphenes prepared by different methods: characterization, properties and solubilisation, *Journal of Materials Chemistry 18*, 1517–1523, (2007)